Investigating the Cyclic Performance of Laser Sintered Nylon 12

The University Of Sheffield.

Thesis submitted to The University of Sheffield in partial fulfilment of the requirements for the degree of Doctor of Philosophy

Hoda Amel

Department of Mechanical Engineering

University of Sheffield

December 2015

Abstract

The growing demand from industries for light-weight structures calls for manufacturing techniques capable of producing complex optimised designs. Laser Sintering is one of these manufacturing techniques that allow the production of end-use parts directly from computer files with no tooling required. For these parts to be used in industrial applications, their mechanical properties throughout in-service applications must be examined. The focus of the present work is to provide an understanding of the dynamic performance of Laser Sintered Nylon 12 parts. In order to investigate the viscoelastic properties of the material, Dynamic Thermal Mechanical Analysis was performed at different frequencies and temperatures. Samples with three different section thicknesses were produced and the effect of section thickness on their tensile properties was examined. Tension-tension cyclic behaviour of samples was studied and cyclic creep was shown to have a great impact in such behaviour in addition to fatigue. Pure tensile cyclic loading could not be achieved hence fully reversed cyclic loading was chosen as an alternative approach. Samples with different section thicknesses were subjected to fully reversed force-controlled cyclic loading and the effect of section thickness on their fatigue life was studied. The percentage of porosity within the samples was measured and its influence on fatigue life of samples was investigated. Thermal history of the samples was recorded during cyclic testing, to inspect the influence of temperature on their fatigue life. Forced convection was applied to the samples to investigate its possible effect on increasing the fatigue life of samples.

Acknowledgements

I would like to express my sincere gratitude to my supervisor, Professor Neil Hopkinson, for his guidance, encouragement and unconditional support from the very first day for which I am deeply grateful, and my co-supervisor, Dr Jem Rongong, for his invaluable advice and assistance on the dynamic aspects of this research.

This research would not have been possible without the help of many people. My warmest gratitude go to all my colleagues and friends in the Advance Manufacturing Centre who gave an opinion on my work and for all the stimulating discussions that inspired me during my research. I would also like to thank the technical staff who provided the necessary help that ensured the successful completion of this work. Special thanks to Farhana for proof reading this thesis.

My warmest thanks to every member of my family for their encouragement and support throughout these years. My most sincere thanks to my parents for believing in me and always being there for me, and to my little sister for all the joyful moments we shared.

My heartfelt appreciations to my most loving and caring husband, Hadi, who made the world a better place for me from the moment he stepped into my life. Thanks for all the technical and emotional support, for always believing in me and encouraging me every single day. I could not have done this without you.

Contents

List of Figures

List of Tables

Nomenclature

T_g	Glass transition temperature, °C
T_m	Melting temperature, °C
T_b	Part bed temperature, °C
LP	Fill laser power, W
SS	Scan spacing, mm
BS	Scan Speed, mm s^{-1}
h	Slice thickness, mm
ED	Energy density, J mm^{-1}
C	Specific heat, J kg^{-1} K^{-1}
k	Thermal conductivity, W m^{-1} K^{-1}
T_R	Recrystallization temperature, °C
E_c	Compressive modulus, Pa
S_c	Compressive strength, Pa
t	Present time, s
τ	Previous time, s
G	Relaxation modulus, Pa
ε	Strain, %
$\dot{\varepsilon}$	Strain rate, s^{-1}
ω	Angular frequency, rad s^{-1}
G^*	Complex relaxation modulus, MPa
η	Loss factor
E	Young's modulus, MPa
T_0	Reference temperature, °C
C_1 and C_2	William-Landel-Ferry constants
α_T	Shift factor
J	Creep compliance, Pa^{-1}
FCP	Fatigue Crack Propagation
E^*	Complex Young's modulus, Pa
E'	Storage (elastic) modulus, Pa
E''	Loss (viscous) modulus, Pa

$\boldsymbol{Tan\ \delta}$	Damping coefficient
$\boldsymbol{K}$	Stiffness, N m^{-1}
EaB	Elongation at Break, %
UTS	Ultimate Tensile Strength, MPa
$\boldsymbol{D}$	Displacement, mm
$\boldsymbol{R^2}$	Coefficient of determination
$\boldsymbol{p}$	Level of significance
$\boldsymbol{\dot{E}}$	Energy generated per second, J s^{-1}
$\boldsymbol{f}$	Frequency, Hz
$\boldsymbol{\sigma}$	Peak stress, MPa
$\boldsymbol{J''}$	Loss compliance, Pa^{-1}
$\boldsymbol{T}$	Temperature, °C

1. Introduction

1-1- Context

Automotive and aerospace industries have been dealing with the challenge of producing lightweight structures to reduce fuel consumption and increase energy efficiency, while maintaining safety and comfort standards for a long time. Different approaches such as using materials of less weight but similar performance -polymers and composites- or altering the current parts by high stiffness, reduced weight designs have been attempted by industries. The challenge for utilizing alternative designs is a manufacturing process with the capability of fabricating complex structures with reduced need for post-processing to get the end products [1].

Additive Manufacturing (AM) has attracted the interest of researchers over the past decade, as a layer-wise technique enabling manufacturers to produce parts with high geometric complexity in a reduced time and with no tooling required. Some of the materials and processes employed are mature enough that AM techniques have been transformed from producing prototypes with poor and unrepeatable properties to producing end-use parts with properties comparable with the ones from conventional techniques.

Laser Sintering (LS) is an AM process where a laser scans the surface of a layer of powder to sinter the particles to fuse and form a new part. Unlike other AM processes, LS allows building of parts from a wide range of materials including; polymers, metals and various

types of composites, while possessing the advantages of AM. However, to use this process in automotive and aerospace applications the mechanical properties of the parts must be satisfactory and must meet the standard requirements.

In the context of automotive and aerospace industries, many of the internal parts are naturally under dynamic loading of which the bearings and engine caps are good examples [2]. Furthermore many polymeric biomaterials such as biomedical implants and devices, which are considered as a growing market for AM processes due to their complex shapes, experience a combination of static and dynamic loading in their service conditions [3]. In spite of its importance for in service applications, cyclic behaviour of polymer LS parts has been scarcely studied previously.

The focus of the research presented in this thesis is to investigate the influence of parts' section thickness on their performance under cyclic loading. To study this effect, parts of different section thicknesses were produced and subjected to various cyclic loading conditions. Influence of different aspects such as morphology and thermal behaviour of the parts, in addition to section thickness, on their fatigue life was studied. Additional experiments were performed to understand viscoelastic behaviour of the material and its effect on parts' cyclic performance.

1-2- Thesis Structure

This thesis is presented in three distinct stages; literature review consisting of chapters 2-5, a preliminary investigation based on a preliminary hypothesis, and a principal investigation leading to key findings of this work. An outline of the thesis chapters are given below.

Chapter 1. This chapter provides an introduction to the present study and an overview of the thesis chapters.

Chapter 2. An introduction to Additive Manufacturing is provided in this chapter. Advantages of Additive Manufacturing and some example applications are presented. Polymer additive manufacturing processes are classified and briefly described emphasizing their advantages and disadvantages. Laser sintering is introduced as the most suitable process for long term industrial applications.

Chapter 3. This chapter provides a detailed description of polymer laser sintering process. Build process and parameters are introduced and the key parameters influencing properties of final parts are presented. Findings on mechanical properties of laser sintered parts are reviewed, and gaps in the field are identified.

Chapter 4. As the material of interest in this research is a polymer, this chapter provides an introduction to polymer materials and their properties. Effect of different structural aspects of materials such as crystallinity and viscoelasticity as well as external parameters such as temperature and frequency on performance of polymers are reviewed and reported.

Chapter 5. In this chapter fatigue and failure mechanisms of polymers are reviewed. Cyclic testing variables and influence of testing conditions on material's behaviour are presented. It is shown that fatigue behaviour of polymers is significantly dependent on test conditions.

Chapter 6. Hypothesis and research objectives of this research are presented in this Chapter

Chapter 7. In this chapter samples design and manufacturing process are explained in details. This chapter consists of two main experimental sections. The first section explains the methodology and experimental approach to assess viscoelastic properties of the material. Experiments to investigate initial physical and mechanical properties of the samples are described in second section

Chapter 8. The second objective of the research is examined in this chapter. Samples of different section thicknesses are subjected to tension-compression cyclic loading and their fatigue lives are compared. Relationship between fatigue life of samples and their physical properties is also examined and reported in this Chapter

Chapter 9. Samples behaviour subject to load-controlled tension-compression cyclic loading and influence of their section thickness on this behaviour is reported in this chapter.

Chapter 10. Morphology of the samples is obtained by micro-CT scanning and effect of porosity on their cyclic performance is studied.

Chapter 11. In this chapter maximum surface temperature of the samples is recorded and is employed to create the thermal history and study the thermal behaviour of the samples under tension-compression loading. Effect of cooling on fatigue life of samples is also studied in this chapter by applying forced convection on the samples while they are tested.

Chapter 12. Main conclusions of this work and some possible ideas for future research work are included in this chapter.

2. Additive Manufacturing

2-1- Introduction to Additive Manufacturing

The basic principle of Additive Manufacturing (AM) is that a physical part which is initially generated using 3D Computer Aided Design (CAD) or reverse engineering can be fabricated directly by adding material in layers, each layer representing a thin cross-section of the part. The technology was first commercialized as Rapid Prototyping (RP) and was employed for rapidly creating a part representing the final product; whilst nowadays the machines have the ability to make parts which can directly be used as end-use products, therefore the term AM is increasingly used to describe these technologies.

While other manufacturing processes need to determine various details such as; the order different features can be fabricated in, tools and processes to be used and additional fixtures required to complete the part, the only details required by AM are some basic dimensions of the part and a small amount of understanding of how the AM machine works and the materials being used [4, 5].

2-2- Additive Manufacturing Steps

A large number of different Additive Manufacturing processes with different build procedures and different build materials are available, however most Additive Manufacturing processes, at some degree, consist of the 8 following steps [6], as illustrated in Figure 2-1.

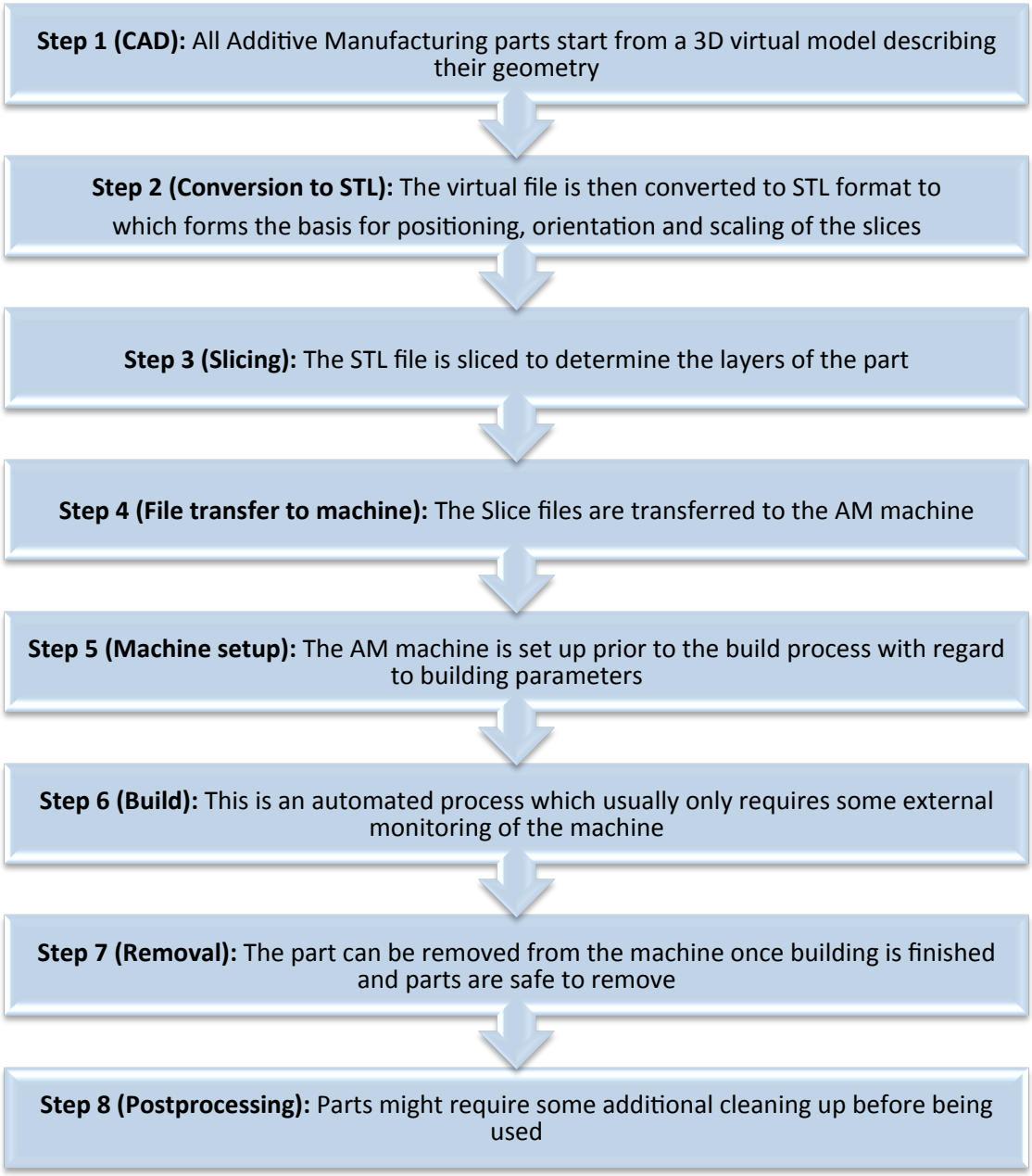

Figure 2-1- standard process steps for AM

2-3- Advantages

AM has the potential to reduce or eliminate many stages of traditional manufacturing chains, reducing the time required for processes such as tooling and assembling of parts. Due to the fact that no tooling is required in these processes, AM enables the manufacture of high geometric complexity and provides new design freedom for creating new types of products.

Parts can be designed and optimised for their specific function with reduced need to consider how they will be manufactured, which is paramount when parts are to be machined or moulded. Figure 2-2 shows some examples of complex geometries which are impossible to make with other automated manufacturing techniques.

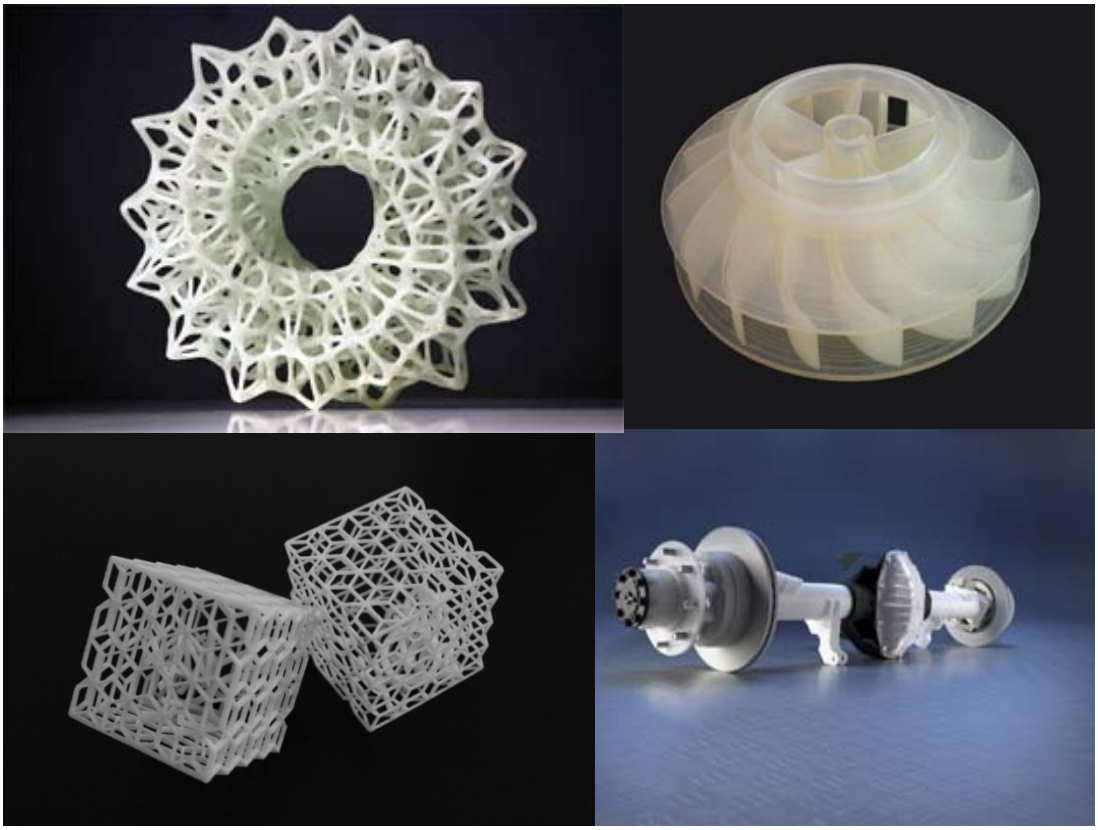

Figure 2-2- Examples of Additive Manufactured parts [7, 8]

With no tooling or moulds required, AM is often a perfect choice for producing one-off or limited edition products, with lower cost and in less time. AM also allows distributed manufacturing, which means parts do not have to be made at one production location and shipped to the place required [9]. Finally, AM, has the potential to produce less waste than traditional mass manufacturing processes, leading to much cleaner, more streamlined, more versatile manufacturing facilities [4, 10].

AM processes are capable of producing parts in a wide range of materials including polymers, metal, ceramics and composites. However this research will only consider processes that produce parts in polymeric materials.

2-4- Polymer Additive Manufacturing Processes

There are several ways to classify polymer AM technologies, one of which is to classify processes according to the type of raw material input. Figure 2-3 illustrates some of the key processes and the techniques employing them.

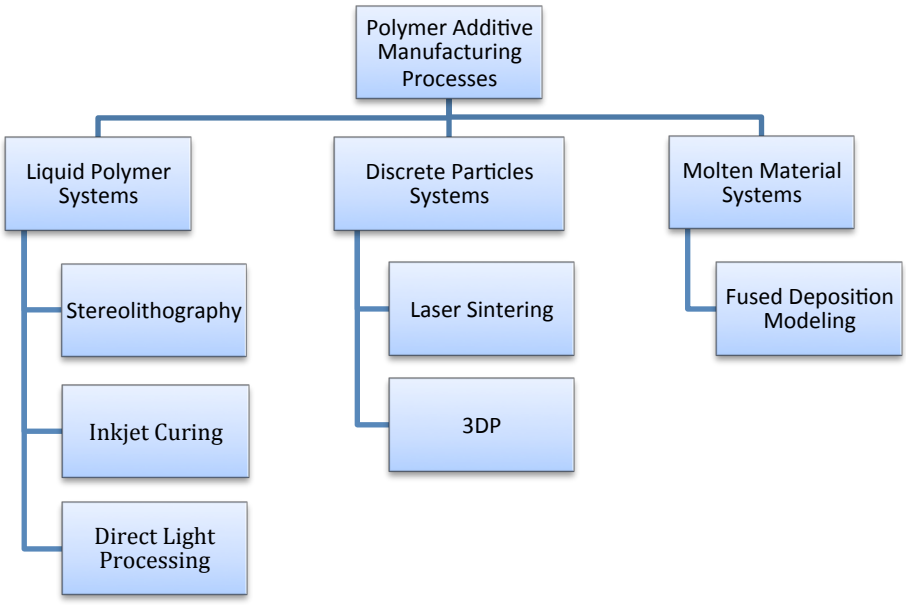

Figure 2-3- Classification of Polymer Additive Manufacturing processes

2-4-1- Liquid Polymer Systems

These systems, including Stereolithography, Digital Light Processing (DLP) and Inkjet Curing, work on the basis of curing a photopolymer liquid via UV electromagnetic radiation. Some of these techniques cure the layer point to point using point sources of UV e.g. the use of a scanning laser in Stereolithography, while others solidify the entire layer at once e.g. DLP [4–6].

Stereolithography

Known as the founding process within the field of Rapid Prototyping, this technology involves curing and solidification of a liquid photosensitive polymer through the use of a UV laser beam, which supplies the energy required to initiate curing in the resin.

The stereolithography machine consists of a computer, a vat containing a photosensitive polymer, a moveable platform and a laser system. The manufacturing process starts by lowering the build platform in the vat of resin, leveling it to the very top of the vat; so that a thin film of polymer, typically of 100µm thickness, covers it. The laser then selectively cures the polymer to form the first layer. The platform then dips further into the vat allowing another film of polymer cover it to form the next layer.

Stereolithographic parts are chemically unstable due to continued curing. These parts become stiffer over time which makes them unsuitable for long term applications requiring consistent mechanical properties [6, 11].

Inkjet Curing

An Inkjet printer uses an array of printing heads to deposit small droplets of photopolymer selectively to form a layer, as thin as 16 microns, of the desired part. A UV lamp then passes over the deposited layer causing it to cure. A second series of jets can also deposit the supporting material [6, 12].

Due to its ability to precisely deposit very small volumes of material, this technology has become an important approach for many applications such as flexible electronics, nanotechnology and tissue engineering [13]. However, as with streolithography, chemical instability of the parts and their continued curing can lead to brittle parts, which can be an issue for long term applications.

Direct Light Processing

A system currently employing this technology is the Perfactory process by Envisiontec. As in other Liquid Polymer systems, the main process is curing resins by photo-polymerisation. However, Perfactory uses a different approach in curing the resins. The photo-polymerisation process is created by a technology called Digital Mirror Devices developed by Texas Instruments, where a 2D matrix of mirrors are selectively switched on and off to reflect UV light onto the build area, in order to cure the resin in the selected areas.

The process is rather quick compared to other AM processes, with a build speed of 10-15 seconds per layer, and the resolution is fairly fine, between 50-150µm. However, it is mostly suitable for producing small parts such as hearing aid devices. Furthermore, as in other liquid

polymer technologies, chemical instability due to continued curing is an issue for long term use of parts [6, 14].

2-4-2- Discrete Particle Systems

Two different technologies use thermoplastic polymer particles as their base material. In one approach a laser beam is employed to elevate the temperature to melt the polymer powder (Laser Sintering), allowing the particles to bond. There are a variety of such systems, with the main commercial suppliers being EOS and 3D Systems.

Another approach is to apply printer technology into the powder bed (3D printing). In this approach, a binder or solvent is printed onto the powder bed, causing the powder particles to stick together to form a 3D structure. The system employing this approach is known as Three Dimensional Printing [5].

Laser Sintering

The Laser Sintering (LS) process is in some ways similar to Stereolithography but with the raw material in the form of powder rather than liquid. The build process starts by spreading a layer of powder, of typically 100μm thickness, over the build area. A computer controlled laser selectively scans over this area to heat up the powder particles to melt and consolidate by liquid phase sintering. A fresh layer of powder is then spread over the previous layer, so that another layer of the part can be made and bonded to the layer below by the laser. The process continues until the 3D part is made without the need for additional supports as the un-fused powder acts as a supporting material [15, 16]. A schematic of the process is illustrated in Figure 2-4.

When sintering highly crystalline polymers, especially nylon, the powder bed is held just below the powder's melting temperature (T_m) and the laser elevates the powder temperature above T_m causing partial or full melting. This leads to good binding of particles and as a result good mechanical properties, making semi-crystalline polymers a good choice in AM applications. Use of amorphous polymers, such as polycarbonate, on the other hand, is usually restricted in AM applications. When manufacturing these polymers, the powder bed temperature is elevated to just below the powder's glass transition temperature (T_g), because they do not have a sharp melting point, and the laser elevates the powder temperature above T_g leading to weaker parts than the ones sintered at melt temperature [6].

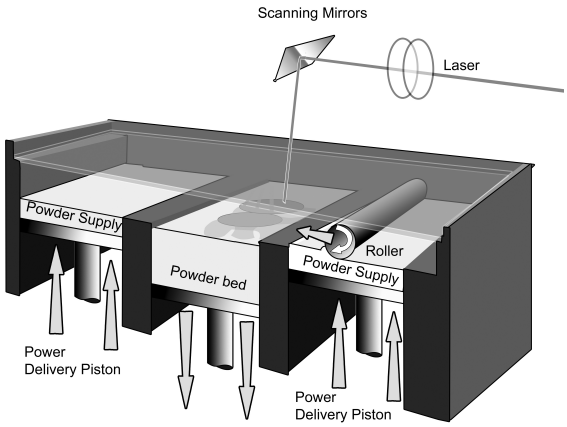

Figure 2-4- Schematic of LS Process[6]

Three Dimensional Printing

In Three Dimensional Printing (3DP) process, like other discrete particle processes a layer of powder is laid on the building area. A binder material is then selectively printed on the powder layer. This layer is then lowered down and covered by another layer of powder on which the same process is repeated. The binder material can be a solvent as practiced by VoxelJet.

This process is relatively fast and inexpensive, however due to the mechanical properties and brittleness of the manufactured part, 3DP is not recommended for load bearing applications [17, 18].

2-4-3- Molten Material Systems

A pre-heating chamber is used in these systems to heat the material to its melting temperature. The molten material can then flow through a nozzle in a controlled manner. The most well-known of these techniques is Fused Deposition Modeling.

Fused Deposition Modeling

In the Fused Deposition Modeling (FDM) process, a thermoplastic polymer such as polycarbonate, polyphenylsulphone or ABS, in the form of a filament is fed into an extrusion head. The filament is then heated to a semi-liquid state and extruded on the platform through

a nozzle that traverses in X and Y direction to form the layers of the part. A separate nozzle is also used to extrude the support material.

This simple process makes FDM an easy approach; however several drawbacks exist; part resolution is limited by filament diameter, build speed is quite low as the nozzle should move in X and Y direction to form each layer and mechanical properties of the part are orthotropic as bonding of the layers in Z direction is not very good. These limitations often render FDM unsuitable for end use parts [14, 19].

2-5- Example Applications

Although AM processes are still developing, they are already being used in numerous applications in various industries including aerospace, medical and automotive.

The aerospace industry is a key growth market for Additive Manufacturing. Environmental control system ducts are typical applications for polymer AM. Examples are air ducts manufactured by LS for the F-18 Military jet and the Boeing 787.

Offering of a direct CAD-to-part process allows production of patient-specific parts such as hearing aid bodies using data derived from 3D scanning of an individual's ear. The data is then used in streolithography or SLS to create a custom fitting hearing aid body (see Figure 2-5a).

AM techniques enable design and fabrication of anatomically shaped scaffolds with varying internal architectures which allows precise control over pore size, porosity, permeability, and stiffness. This has made AM a desirable technique for bioengineering applications with the aim to enhance cell infiltration and mass transport of nutrients and metabolic waste throughout the scaffold [20, 21].

AM is commonplace within Formula 1 motor racing. The Renault Formula 1 team use LS to manufacture a number of parts for their race cars, such as cooling ducts (see Figure 2-5b) and aerodynamic fins. In this way, modifications can be implemented quickly and at significantly reduced cost.

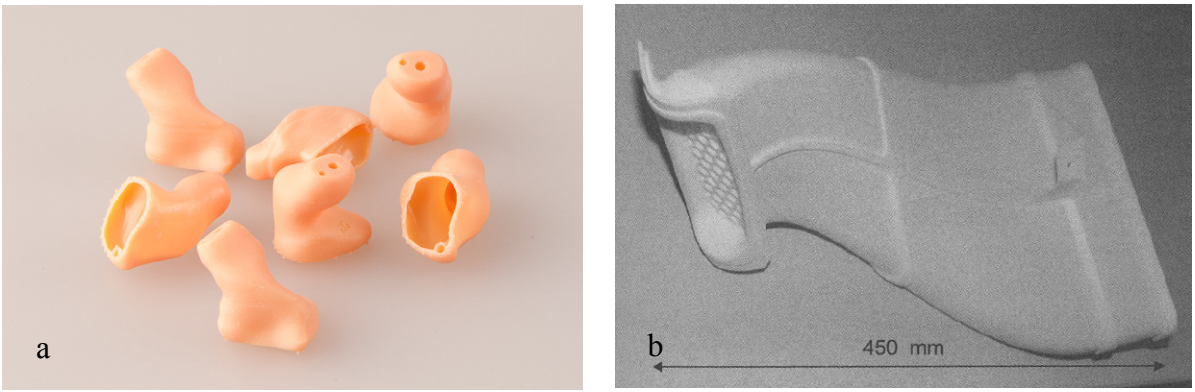

Figure 2-5- a) Custom made hearing aid bodies [19], b) LS cooling duct for Renault F1 race car [6]

2-6- Summary

This chapter has provided an introduction to AM, the generic process for AM techniques and its advantages and capabilities, AM process classification and a brief description of some of the most widely employed polymer based processes. AM techniques are often a satisfactory choice for complex and unique geometries. LS as one of the AM processes is more widely employed in industries than other AM approaches due to its geometric freedom, acceptable material properties, and chemical and mechanical stability. The following chapter examines LS in detail as the technology employed within this research.

3. Laser Sintering

3-1- Introduction to Laser Sintering

As described in the previous chapter laser sintering (LS) is an AM process which generates complex 3D parts by sintering powder particles in a layer by layer basis using a CO_2 laser.

Unlike other AM processes, LS allows building of parts in a wide range of materials, including polymers, metals and various types of composites (e.g. metal-metal, metal polymer, polymer-ceramic, metal-ceramic composites). Furthermore, parts produced by LS demonstrate material properties that are very close to the material properties obtained by conventional manufacturing processes, like injection moulded plastic components [23].

This chapter outlines the parameters influencing the properties of the final part and to follow rules in designing and building of a part.

3-2- Basic Principles of Laser Sintering

As described in the previous section the base line of the LS process is selective sintering of powder particles. Sintering is described as a powder processing technique where adjacent powder particles bond to one another, via formation of sintering necks, upon heating and sometimes in the presence of pressure to form a solid object [24].

Two primary classifications of sintering are solid state sintering and liquid phase sintering. Solid state sintering occurs below the materials melting temperature through atomic diffusion in solid state and is rarely applied in AM techniques due to its slow process. Liquid phase sintering can occur at either partial or full melting of the powder particles. In this case, the molten polymer flows between the powder particles and forms sintering necks [24, 25]. The LS process of polymers produces solid parts from powder particles using liquid phase sintering.

During laser sintering of polymers, the energy supplied by the laser raises the powders' temperature beyond its glass transition or melting point based on the polymer type. This results in partial or full melting of the powder particles and turns them into a viscous flow. Necks are formed between adjacent molten particles or their molten outer layer and the liquid phases begin to coalesce around the particle cores that have remained solid as shown in Figure 3-1. As the molten regions cool down upon removing the energy source, polymer crystals nucleate and grow, recreating crystalline mixed up with amorphous regions [23].

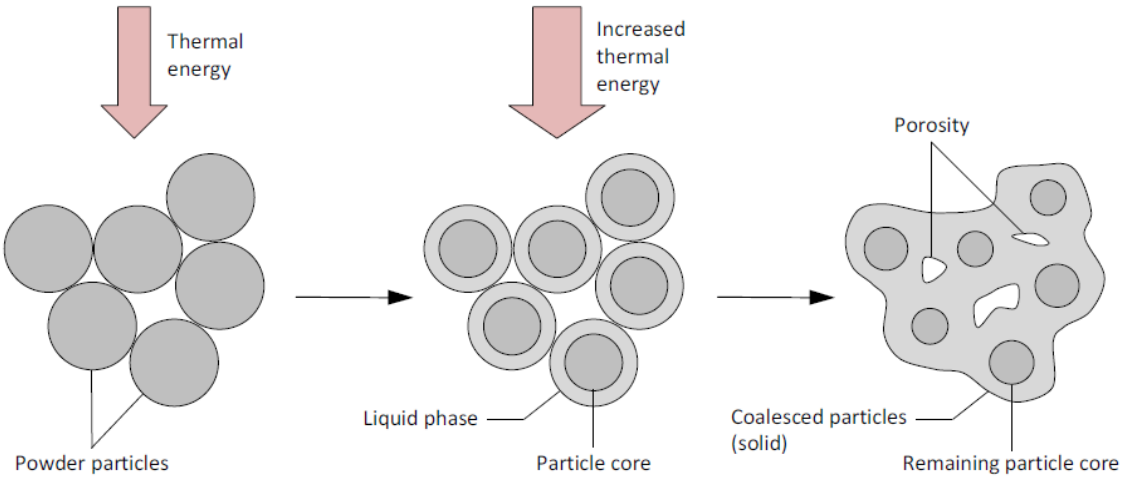

Figure 3-1- Schematic of liquid phase sintering in LS [26]

3-3- Build Process and Key Parameters

The two manufacturers currently commercialising LS systems are 3D Systems of the United States (previously DTM) and EOS of Germany [27]. As previously described, like other AM processes, the LS process starts by making of a 3D virtual model which is later used to define the geometry of the image scanned by the laser on each layer of powder, consolidating the powder particles and gradually generating the 3D part.

From theories and experiments, it is known that powder properties influence fabrication parameters in the sintering process. It is also known that both powder properties and fabrication parameters have a great influence on the mechanical properties and surface qualities for LS parts [28]. Therefore, it is important to obtain a deep understanding of the relationship between powder properties and fabrication parameters in the LS process, and the parts produced using this process.

3-3-1- Build Parameters

To achieve optimum quality for the final part, different fabrication parameters are set in the machine in accordance with powder properties and application requirements. Some of these parameters are described in the following:

***Part bed temperature* (T_b):** The temperature at which the powder in the part bed is maintained. Powder in the bed cylinder is heated to part bed temperature before the laser starts scanning. T_b is used for reducing laser power and distortion in the sintering process [28].

For amorphous polymers, part bed temperature should be set close to glass transition temperature (T_g). For a crystalline polymer part bed temperature should be set 3-4°C below its melting temperature (T_m) [29].
Results by Tontowi and Childs concluded that powder bed temperature affects the density of sintered parts. Lower powder bed temperatures resulted in lower sintered part densities [24].

***Fill laser power* (*LP*):** With laser power, powder will be heated rapidly to a higher temperature above part bed temperature. If this higher temperature reaches T_m, the polymer will behave as a highly viscous liquid. Above T_m, the polymer is in a liquid state and can

flow. Due to this liquid flow, the porosity can be reduced and some mechanical properties of the parts can be increased.

***Scan spacing* (*SS*):** The distance between two neighbouring parallel scan vectors. If scan spacing is too great, the cross-section may not be completely sintered. It is related to the laser beam size and energy density.

Scan Speed or Beam Speed (BS): The distance the laser spot moves across the bed in a time step. Higher or lower scan speeds can affect the sintering quality of parts.

***Slice thickness* (*h*):** The depth that the part piston lowers for each layer, which determines powder thickness of each layer in the part cylinder. A stair-step effect is caused by slice thickness. Slice thickness is an important factor that influences building time, surface roughness and mechanical properties especially in z direction. Small slice thickness can decrease surface roughness but it takes more time to build a part than large slice thickness does [27].

Energy Density (ED): For each material there is an optimum energy density that is generally determined on an empirical basis, although some general rules apply. The energy density is a function of the beam speed (BS), the fill laser power (LP) and the scan spacing (SS) and can be determined using the following equation [27, 30]:

$$ED = \frac{LP}{SS \times BS} \ J/mm^2 \qquad (3\text{-}1)$$

Vandenbroucke et al [31] have identified volumetric energy density as the laser power divided by the product of laser speed, scan spacing and layer thickness, which therefore includes the effect of varying layer thickness and can be related directly to the melting characteristics of the polymer material.

$$Volumetric\ ED = \frac{LP}{SS \times BS \times h} \ J/mm^3 \qquad (3\text{-}2)$$

Starr et al [32] have obtained energy-melt ratio by dividing the energy required to fully melt the powder by the energy density. In their study, they introduce energy-melt ratio as a useful

parameter for relating process conditions to the physics of powder melting which can be used to predict the effect of a change in bed temperature or a change in material. Typical calculated energy-melt ratio for LS process is around 2, which means the actual energy required for melting the powder during the LS process is twice the theoretical amount.

3-3-2- Powder (Material) Parameters

Several powder parameters have been shown to influence the final properties of LS parts. Some of these parameters are shown to affect the sintering process of the powder while others influence the pre/post sintering behaviour of the material.

Powder flowability has been considered as a key parameter in the LS process that influences the parts' density, surface finish and mechanical properties [33, 34]. Powder flow can be affected by different parameters such as particle size, particle size distribution, particle shape and temperature.

Physical properties of the powder including particle size and density are considered as important factors in the LS process. Particle size is important since larger particles are less likely to melt completely due to the low thermal diffusivity of polymer powders, which may result in higher porosity, lower mechanical properties and rougher surfaces on sintered parts [35].

Powder particle morphology also influences consolidation. For a powder with near spherical shape particles, when no pressure is applied during consolidation, the voids and air trapped between the particles remain in the solid part. This reduces the effective cross section and the tensile strength [20].

LS is a heat transfer process in which the polymer powder is heated rapidly by laser and cooled down naturally causing solidification to form the part. Thermal properties such as specific heat (C) and thermal conductivity (K) are therefore of particular importance [22].

Thermal transitions of the powder particles is another important aspect in the LS process. Differential Scanning Calorimetry (DSC) curves are employed to study thermal behaviour of the material including its melting and recrystallization temperatures. Powder particles with a narrow melting range and a wide super-cooling range (difference between melting and

recrystallization temperatures) produce parts with less shrinkage and as a result more precise dimensions [23].

Viscosity of the melted powder has a significant influence on properties of the final part. To obtain parts with densities close to injection moulded parts, the melt viscosity should be low enough to allow complete consolidation within the time of the process, however low viscosity also results in high shrinkage and as a result poor part accuracy. The melt viscosity is linearly related to the Molecular Weight (MW) of the powder, hence an optimum MW range is desirable for the LS process [23].

3-4- Materials

It is often perceived that any material that can be provided in powder form and that melts as the temperature rises can be processed by LS, however practice is still far from this ideal situation [27].

As in any manufacturing process, the choice of material in AM processes is partly dependent on the specifics of the process, imposing constraints on the range of available materials. Coupled with these constraints are the desired final product properties required by the user.

Both 3D Systems and EOS supply a small number of polymer materials for their machines; most of these are based on Polyamides (PA12 and PA11), although Polypropylene and PEEK materials have recently been released by EOS. Powdered materials specifically designed for laser sintering are also produced by Advanced Laser Materials (ALM); again these are predominantly polyamide-based thermoplastics, with a more recently released thermoplastic elastomer. Despite some advances in material choice over the past couple of years, this has been very limited and Polyamide 12 remains by far the most widely used laser sintering polymer making up more than 95% of the current market [23].

Generally, polymers can be classified into two main types: amorphous and crystalline. Amorphous materials, e.g. PC, have chain molecules arranged in a random manner. Semi-crystalline materials e.g. nylon, on the other hand, have some chain molecules arranged in an orderly structure. Crystalline and amorphous polymers have different thermal properties which determine fabrication parameters in LS [22].

3-4-1- Consolidation Mechanisms

Semi-Crystalline polymer

The laser consolidation of semi-crystalline polymer powders occurs by increasing the powder temperature above their T_m. Semi-cystalline polymers have a highly ordered molecular structure with sharp melt points. They do not gradually soften with rising temperature but rather remain hard until a given quantity of heat is absorbed and then rapidly change into a viscous liquid. The molten polymer flows in between the powder particles, forming sintering necks. With enough heat, the complete layer is fully molten. As the molten polymer cools down below the recrystallization temperature (T_R), polymer crystals nucleate and grow, recreating regions of ordered molecular chains (crystallites) mixed up with disordered amorphous regions as shown in Figure 3-2 [36].

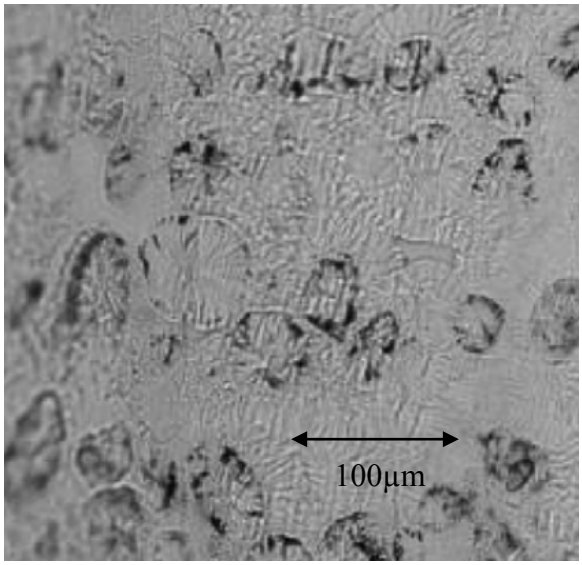

Figure 3-2- Optical microscope images of microtomed specimens [37]

The densities obtained are close to full density and most of the mechanical properties are close to those of moulded polymers. However, the freezing of the polymer at T_R may lead to shrinkage (a phenomenon that occurs at a lesser extent with amorphous polymers), that may induce geometrical inaccuracies and distortion of the part. A good way to prevent this is to preheat the polymer powder to a temperature slightly below its melting temperature and keep it there for a certain amount of time after consolidation. In such a way, no major shrinkage

will occur during laser melting, and localized shrinkage (and hence part distortion) can be reduced [15, 29].

Amorphous Polymers

The consolidation of amorphous polymer powder occurs by laser heating the powder to just above T_g, at which the polymer is in a more viscous state than semi-crystalline polymers at similar temperature. Amorphous polymers have a randomly ordered molecular structure. They do not have a sharp melt point but instead soften gradually as the temperature rises.

The viscosity of these materials changes when heated, but they seldom are as easy flowing as crystalline materials. The flow and sintering rate will be less than semi-crystalline polymers, resulting in a lower degree of consolidation, higher porosity, lower strength, but also a lower shrinkage that is favourable when creating patterns for casting [23, 25].

3-5- Feature Resolution and Design Freedom

The LS process like other AM processes can produce parts of high shape complexity without the need for any tooling. This ability enables designers to be free from many of the constraints of design for manufacturing [29].

Commercial LS machines, however, are not designed to fabricate geometries with micron-scale features. The smallest attainable feature size is limited by the diameter of the laser (around 0.4 to 0.5 mm) and the powder layer thickness (most commonly set at 0.1 mm) [30].

3-6- Mechanical Properties

AM technologies have long been renowned for producing parts with poor and/or unrepeatable mechanical properties. As AM of end-use components becomes increasingly viable, the ability to produce parts with repeatable and predictable mechanical properties has become progressively more important.

Nylon 12 with the trademarks of DuraForm PA (3D Systems) and PA 2200 (EOS) is known as the most commonly used material in Laser Sintering of polymers. Some key mechanical properties, published by the machine manufacturers supplying LS Nylon 12 powder are

summarised in Table 3-1. It should be noted that the build parameters have not been provided by the manufacturers and therefore this data can only be used as a rough gauge for the properties of Nylon 12.

Table 3-1- Manufacturers published materials properties for LS Nylon 12 [40, 41]

	3D Systems	EOS
Tensile Strength (MPa)	44	45
Tensile Modulus (MPa)	1600	1700
Strain at Break (%)	9	20

In LS, mechanical properties of the part are influenced by many factors such as powder history, fabrication parameters, fabrication position and orientation, and post-processing, and a fair amount of research has been performed in this area [42].

3-6-1- Tensile Properties

Tensile properties are the most commonly provided properties of LS Nylon 12 by the manufacturers. There is also a noticeable amount of research dedicated to the behaviour of polymer LS parts in tension and the effect of build parameters on them [27, 28, 32, 38, 43, 44, 42]. Caulfield et al [42] investigated the effect of energy density and part orientation on mechanical properties of DuraForm polyamide parts reporting Young's modulus, yield strength and fracture strength increasing due to an increase in energy density as shown in Figure 3-3.

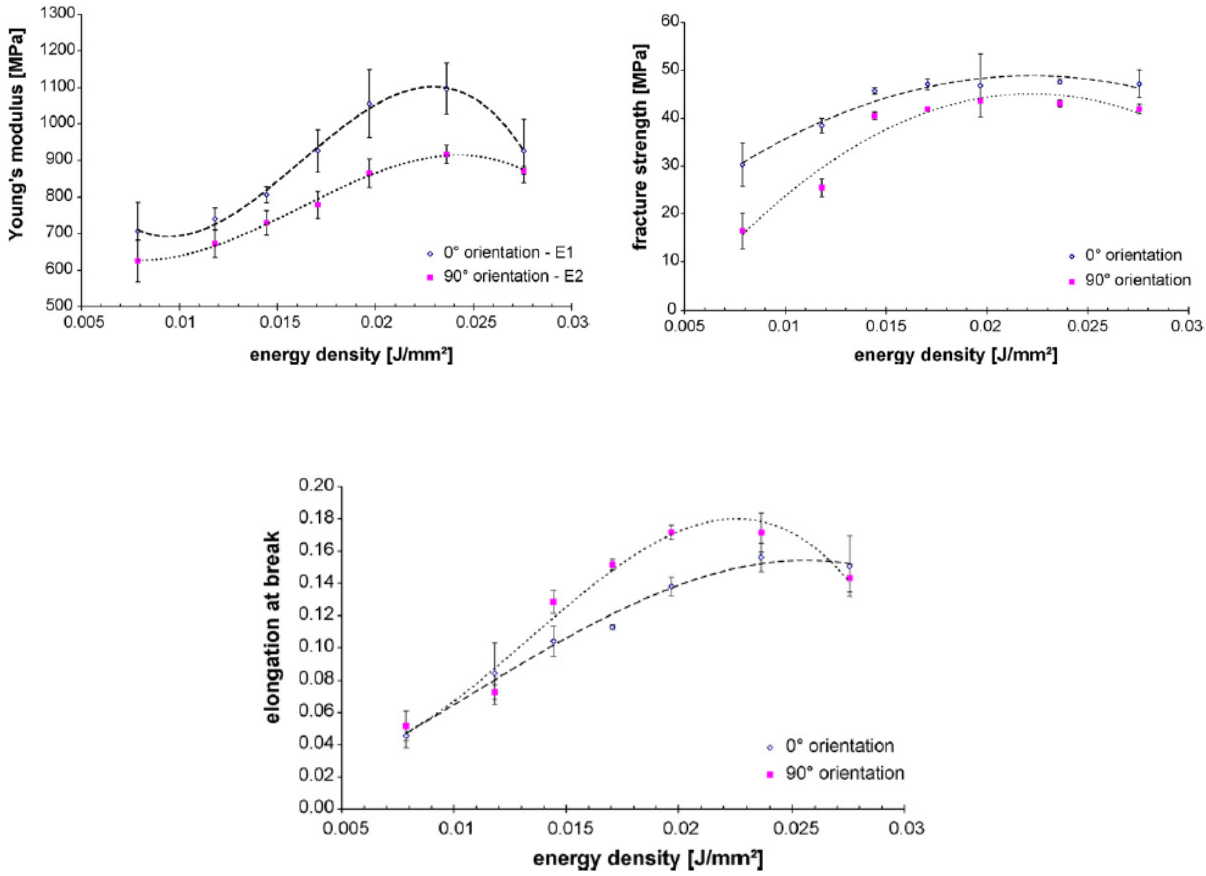

Figure 3-3- Young's modulus, fracture strength and elongation at break for samples made with different energy densities [42]

The relationship between tensile properties of DTM Laserite Polycarbonate Compound LPC-3000 sintered specimens and the energy density has been studied by Ho et al [45] showing that the perpendicular tensile strength significantly depends on the scan spacing. Also their results suggest that the strength of the sintered component is closely related to the density, which is directly proportional to energy density.

Comparing the tensile test results of Nylon 12 parts built with different process parameters and their Differential Scanning Calorimetry (DSC) graphs, employed for quantifying the Degree of Particle Melt (DPM), have illustrated a close correlation between mechanical properties and the derived DPM [37, 44]. Ultimate Tensile Strength and Elongation at Break of the parts increase when using higher process parameters, although they do not achieve injection moulding values [28].

The effect of build orientation on mechanical properties of the parts made by LS is also well documented [38, 42, 46, 47], identifying significant differences based upon build orientation. Research shows that pre-processing parameters can influence the tensile properties of LS parts.

Zarringhalam et al [37] showed that parts made of used powder have improved mechanical properties in comparison with parts made of virgin powder due to their increased molecular weight. Majewski et al [46] studied the influence of section thickness and build orientation on Young's modulus, tensile strength and elongation at break of samples under tensile loading and found that section thickness had no significant effect on tensile properties in any build orientation. Major findings of this study are shown in Figure 3-4.

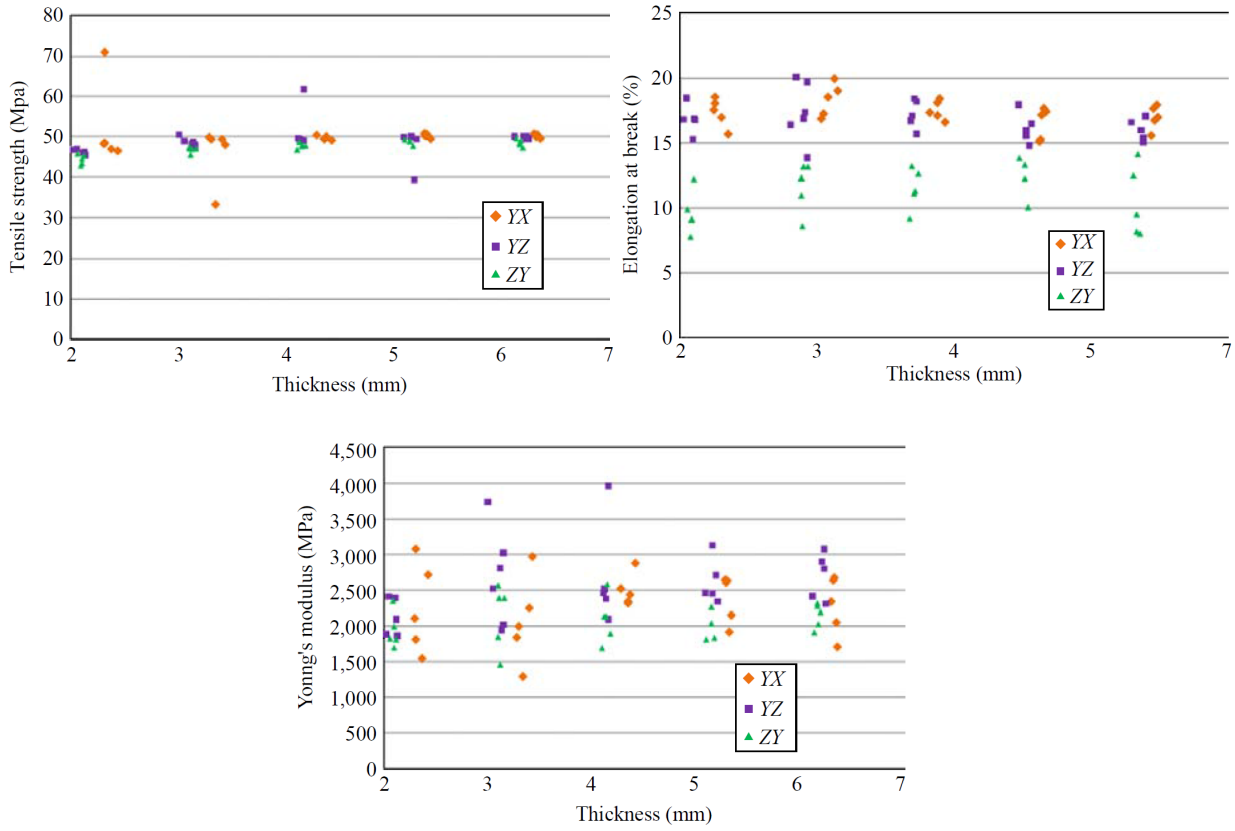

Figure 3-4- Tensile Strength, Elongation at Break and Young's modulus of LS samples with different build orientation and section thicknesses [46]

3-6-2- Compressive Properties

In terms of mechanical properties of polymer LS materials in compression, no information is provided by the manufacturers and a limited number of studies have been performed on compressive properties of parts manufactured from these materials. Compressive modulus (E_c) and compressive strength (S_c) of laser sintered Nylon 12 parts with different build orientations have been obtained and compared in a study by Ajoku et al [47]. The compression test parts built in the x-axis orientation show the highest S_c and E_c values, while the test parts built in the z axis orientation show the lowest S_c and E_c values, although the S_c values had less influence from build orientation than E_c values.

In another study, Ajoku et al [48] compared the compression test results of Nylon 12 compression test parts produced using injection moulding and laser sintering. They reported that the modulus for laser sintered Nylon 12 parts was 10% below the injection moulded Nylon 12. However, their strength values were larger, due to poor toughness of the injection moulded parts. They also produced 2D and 3D finite element models for both samples, applying the same conditions on them, which indicate a reasonable response in terms of compressive modulus in both cases and a better response from the 3D model for compression strength.

3-6-3- Fatigue Properties

Fatigue behaviour of polymer LS parts has been scarcely studied previously and no fatigue information can be found in manufacturers' data sheets. In a study by Blattmeier et al [49] laser sintered specimens made of a polyamide powder (with 60% used and 40% virgin powder) with treated (with surface finishing) and non-treated surfaces were employed to examine surface influence on their fatigue behaviour in a load increase method. No significant influence of surface finishing was observed on long-term mechanical properties of the parts, and LS parts demonstrated a considerable resistance to crack initiation and propagation in comparison with injection moulded parts.

Eleven cylindrical test specimens, laser sintered from semi-crystalline polyamide 12 powder, have been employed in a tension/compression stress-controlled fatigue test with zero mean stress by Van Hooreweder et al [50] to investigate their thermal and microstructural response. Results obtained from the tests revealed that, for a test frequency of 3 Hz, stress amplitudes

less than 18.9 MPa do not cause temperature rise, and the parts experience a cyclic life of over one million cycles. Furthermore, their microstructural observations showed that crack initiation in the parts started from inclusions in the material caused by unfused powder particles.

In a recent study, Van Hooreweder et al [51] have explored the difference in fatigue behaviour of LS and injection moulded Nylon 12 samples. They showed that, despite their different fracture strength, material density, crystallinity and surface roughness, LS and injection moulded samples have similar fatigue properties (Figure 3-5).

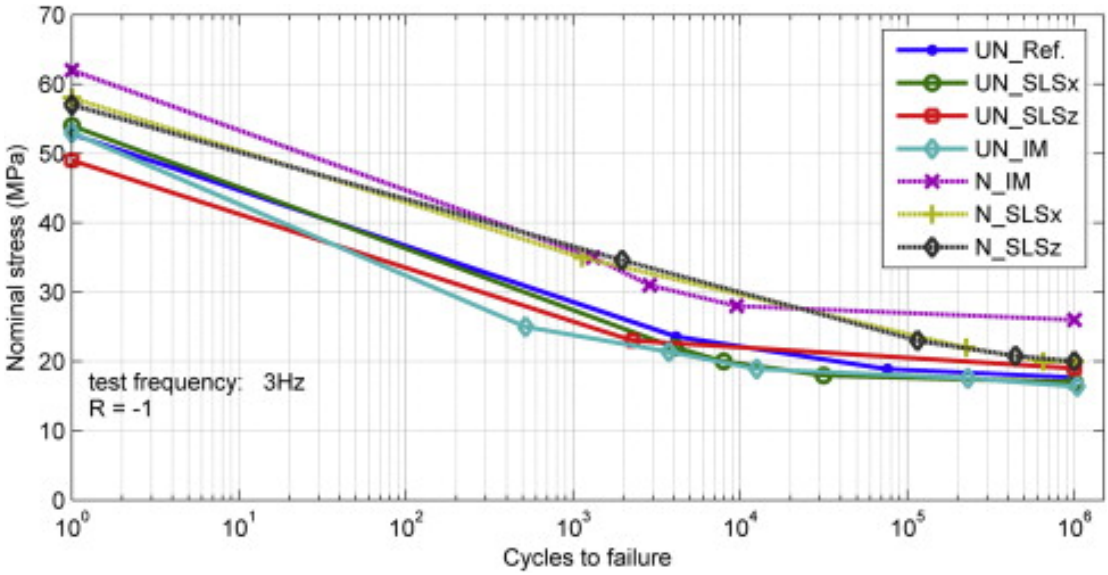

Figure 3-5- Stress vs. Cycles to failure (S-N) curves for un-notched and notched Injection Moulded and Laser Sintered samples built in different directions

Davidson [26] has investigated the long-term mechanical performance of Laser Sintered elastomer shoe midsoles in a force-controlled approach. Munguia et al [52] have looked into rotating-bending fatigue of LS PA12 parts at frequencies of up to 50Hz. They found an endurance limit of 14MPa for these parts, which is not significantly influenced by build orientation.

3-6-4- Fracture Toughness

There have been very few studies on fracture toughness properties of LS parts. Hitt et al [53] determined and compared the fracture behaviour of PA12 parts fabricated by LS and injection moulding under three point bending. Their results indicated that while energy to

initiate crack growth decreases for injection moulded specimens with increasing of specimen thickness, it increases for laser sintered samples. This behaviour could not be related to improved sintering for thicker parts, and they suggested higher molecular weight in thicker samples (as a result of specimens being held in melt state longer) could account for the observed changes.

3-7- Summary

This chapter has provided a detailed description of polymer laser sintering in terms of build procedure, materials and feature resolution. Mechanical properties of LS parts as an area directly relevant to this research has been comprehensively reviewed, revealing that a small amount of studies have been performed on long-term behaviour of these parts and further research is required in case they are to be used in in-service applications.

4. Polymer Characterisation

4-1- Introduction to Polymers

A polymer is defined as a substance composed of extremely large molecules which are formed by linking and cross-linking i.e. polymerisation, of different monomers. A monomer is a small molecule that can be considered as the 'building block' of a polymer. The monomer for Nylon-12 is called laurolactam and hence the polymer is called polylaurolactum [54]. Polymers fit into two categories of thermoplastic and thermosetting polymers.

Thermoplastic polymers become pliable or mouldable above a specific temperature and return to a solid state upon cooling. In most of these materials their chains associate through intermolecular forces, which allows them to be remoulded because the intermolecular interactions spontaneously reform upon cooling. In thermosetting polymers, on the other hand, irreversible chemical bonds are formed during the curing process which break down upon heating (as thermosets do not melt) and do not reform upon cooling. Therefore, thermoplastic polymers are used in the LS process [55].

4-2- Crystallinity

Polymers in the solid state are either fully amorphous or contain both crystalline and amorphous regions. Crystalline regions in a polymer, known as crystallites, are formed when macromolecules are arranged in an orderly manner thus demonstrating long-range crystalline

order. In amorphous regions macromolecules exist without long-range order. Most polymers are in forms of semi-crystalline and amorphous, and purely crystalline polymers are very rare. Semi-crystalline polymers contain both crystalline and amorphous regions and amorphous polymers contain only amorphous regions.

The amorphous and crystalline regions of a semi-crystalline polymer are illustrated in Figure 4-1. It should be noted that in the molten state all polymers are amorphous and crystalline regions are formed during solidification. Polycarbonate is a common example of an amorphous polymer and Nylon-12 is an example of a semi-crystalline polymer.

The degree of crystallinity (% crystallinity) is the fraction of the entire crystalline phase within a specimen. The % crystallinity of a material can vary according to processing conditions and highly depends on the thermal history of the material during processing [56].

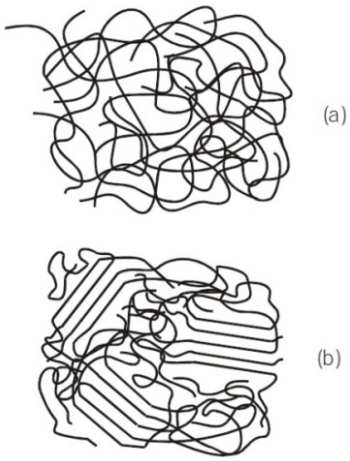

Figure 4-1- (a) amorphous polymer and (b) semi-crystalline polymer with crystalline and amorphous regions

In a semi-crystalline polymer, the degree of crystallinity and size and distribution of the crystallites, have a large effect on the mechanical properties of the material such as modulus of elasticity, yield stress and ultimate stress. Increase in the degree of crystallinity of the material results in tougher and stiffer behaviours [57].

4-3- Molecular Weight

Each sample of a polymer consists of molecular chains of varying lengths and therefore molecular weights. The molecular weight is important in determining polymer properties. Molecular weight distribution is also important in determining viscous flow properties, which may also affect the mechanical properties of a solid polymer indirectly by influencing the final physical state. Direct correlations of molecular weight to mechanical properties such as stiffness, strength, viscoelasticity and toughness have been obtained.

Bretz et al. [58] have studied the effect of molecular weight (MW) on fatigue crack propagation of Nylon 66 and Polyacetal notched specimens and reported that increasing MW results in a decrease in the fatigue crack growth rates and an increase in the apparent toughness (K_{cf}) in both materials.

If molecular weight is too low, the transition temperatures and the mechanical properties will generally be too low for the polymer material to have any useful commercial applications [54, 55].

4-4- Viscoelasticity

Solids store the energy obtained from the work done by external forces during deformation and this energy is available to restore the body to its original shape when forces are removed. Viscous liquids on the other hand, flow irreversibly under the action of external forces. Polymers can display all the intermediate range of properties between these two states depending on temperature and the time scale. A material is termed viscoelastic if it can simultaneously store and (through viscous forces) dissipate mechanical energy. Deformation of a viscoelastic material causes the dissipation of vibrational energy as heat.

A polymeric material usually consists of a carbon atomic structure that is connected together firmly as long molecular chains. Under loading, relative motion of these chains can create a time lag between load and deflection. Subject to cyclic loading, the time lag appears as a phase delay between load and deflection, which is known as damping.

By attention to the selected temperature and frequency zones the proper viscoelastic material for specific application can be manufactured [56, 59].

4-4-1- Constitutive Equation for Viscoelastic Materials

The response of a viscoelastic material to loading is not only affected by the current conditions, but any previous load or deformation history has an effect on it. The following linear constitutive equation is based on the principle that the effect of sequential changes in strain are additive [60].

$$\sigma(t) = \int_{-\infty}^{t} \mathrm{G}\,(t-\tau)\dot{\varepsilon}(\tau)d\tau \qquad (4\text{-}1)$$

$G(t-\tau)$, is the value of the relaxation modulus $G(t)$ at the elapsed time for each applied strain. The transform $(t-\tau)$ can be applied to the convolution integral (Equation 4-1) to obtain frequency domain behaviour. For steady-state harmonic oscillations the strain rate is defined as,

$$\dot{\varepsilon}(\tau) = j\omega\varepsilon(\tau) \qquad (4\text{-}2)$$

where ω is the cyclic frequency and $j = \sqrt{-1}$. The Fourier transform of Equation 4-1, for the infinite time, is given as,

$$\sigma(\omega) = \int_{-\infty}^{+\infty} \left[j\omega \int_{-\infty}^{+\infty} G\,(t-\tau)\varepsilon(\tau)d\tau \right] e^{-i\omega t}dt \qquad (4\text{-}3)$$

Using the convolution theorem for Fourier transform,

$$\begin{aligned} \sigma(\omega) &= j\omega \int_{-\infty}^{+\infty} G\,(t)e^{-i\omega t}dt\varepsilon(\omega) \\ &= j\omega G(\omega)\varepsilon(\omega) \\ &= G^{*}(\omega)\varepsilon(\omega) \end{aligned} \qquad (4\text{-}4)$$

where $\boldsymbol{G^{*}(\omega)}$ is the complex modulus. The complex modulus is represented as,

$$G^* = G_{real}(1 + j\eta) \quad (4\text{-}5)$$

$$\eta = \frac{G_{imag}}{G_{real}} \quad (4\text{-}6)$$

where $\boldsymbol{G_{real}(\omega)}$ is the real part of the complex modulus and is also called the storage modulus and $\boldsymbol{\eta(\omega)}$ is the loss factor.

The inverse transform can be used to find the relaxation modulus from the complex modulus[48],

$$\mathrm{G}(t) = \frac{1}{2\pi}\int_{-\infty}^{+\infty}\frac{G^*(\omega)}{j\omega}e^{i\omega t}d\omega \quad (4\text{-}7)$$

4-4-2- Master Curve

In order to present the complex modulus of a material (loss factor and Young's modulus) in a simple way, these data are presented in the form of Master Curves. For viscoelastic materials a master curve can be generated from a limited number of test results that allow estimation of properties at many different combinations of temperature and frequency. The following section explains the steps that are needed to obtain the master curve [61].

For viscoelastic materials, an equivalent change in material properties can be achieved by altering the temperature or the frequency, which is known as temperature-frequency superposition principle. Material properties can be transformed between the temperature and frequency domain. Measurements taken over the available frequency range at a number of different temperatures can be shifted according to the temperature-frequency superposition principle, to give frequency dependent values at all range at any reference temperature.

Method of reduced variables

The method of reduced variables is based on the temperature-frequency superposition principle. In this method the effect of a change in temperature on viscoelastic properties is to multiply the frequency scale by a shift factor constant for a given temperature.

In the reduced modulus stage, due to the changing of modulus of a viscoelastic material with temperature, to generate a master curve at a reference temperature (T_0) from a number of curves of the Young's modulus (*E)* at different temperatures (*T),* values of *E* at temperature *T* should be reduced to E_0 at T_0, by means of the following equation,

$$E = \frac{E_0 T}{T_0} \tag{4-8}$$

This is due to dependency of stored energy on temperature as would be predicted by the theory of rubber elasticity.

The loss factor has no reduced form because it is a ratio of reduced modulus. This step shows a vertical shift of the data at the reference temperature.

A temperature shift curve is constructed for each set of reduced modulus and loss factor. Each data curve is then shifted horizontally (parallel to the frequency axis for higher or lower frequency), to produce a single curve for modulus and a single curve for loss factor. The approach that has been used for shifting the data along the frequency axis is named WLF (William-Landel-Ferry) equation. William-Landel-Ferry [59] have shown empirically that the shift factor for polymers is given by,

$$\log \alpha_T = -\frac{C_1(T - T_0)}{C_2 + (T - T_0)} \tag{4-9}$$

where T is the temperature, T_0 is a reference temperature, chosen as the glass transition temperature in this equation, to construct the compliance master curve and C_1, C_2 are empirical constants adjusted to fit the values of the superposition parameter α_T.

As an example, Figure 4-2 illustrates the assembly of the master curve for the Young's modulus based on frequency-temperature superposition principle. Data obtained in a range of temperatures, T_1 to T_6 are shifted along the log-frequency axis to form a master curve over an extended frequency range at a reference temperature T_4. The shift along the log frequency

axis required to superimpose data measured at temperature *T* on the master curve is also shown [62].

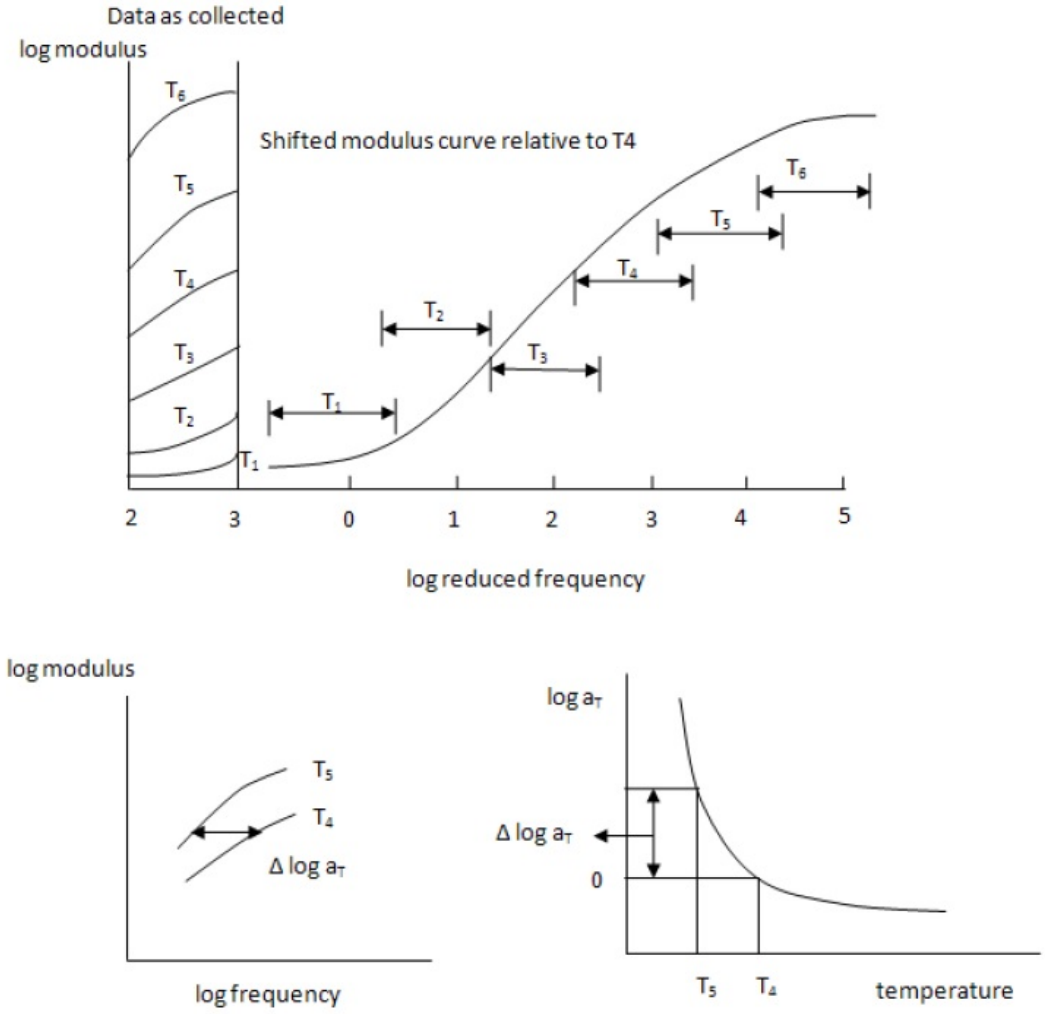

Figure 4-2- Production of the master curve for Young's modulus based on frequency-temperature superposition principle. a) Data collected at temperatures *T*1 to *T*6 in the frequency range of 100-1000 Hz are superimposed on the *T*4 curve by applying horizontal shifts to each isothermal curve. b) The value of each shift required to construct the master curve. c) The relationship of shift factor and temperature [62].

4-5- Mechanical Properties

As described in previous sections, mechanical properties of polymers is highly dependent on testing conditions such as the rate of load application, temperature or amount of strain. For

example, increase in temperature or decrease in strain rate leads to decrease in tensile modulus, i.e. decreasing the strain rate has similar influence on the strain-strength characteristics as increasing the temperature: the material becomes softer and more ductile.

Mechanical properties, such as elastic modulus, in amorphous polymers change dramatically with temperature, going from glass-like brittle behaviour at low temperatures to a rubber-like behaviour at high temperatures, with the transition occurring around the glass transition temperature. However, the fall in modulus over the glass transition region for semi-crystalline materials is much less than for amorphous polymers [61]. Also, the change in modulus or loss factor with temperature or frequency is much more gradual in semi-crystalline polymers than in amorphous polymers, indicating a broader relaxation time spectrum.

In addition to test conditions, mechanical properties of polymers can be influenced by changes in molecular level. Some of these aspects are as follows; Cross-linking (bonds between different molecular chains in thermoset polymers) and entanglements of molecular chains strengthen the polymer. Crystallinity increases strength as the secondary bonding is enhanced when the molecular chains are closely packed and parallel. Deformation by drawing, analogous to strain hardening in metals, increases strength by orienting the molecular chains [63].

4-5-1- Fracture of Polymers

Previous studies have shown three stages in fracture of polymers [64]:

1) Formation of localized microsites of fracture with strongly overloaded inter-atomic bonds, which results from non-uniform load distribution.

2) Scission of overstressed bonds by thermal fluctuations with subsequent formation of sub-microcracks.

3) Coalescence of incipient microcracks into large main cracks, which leads to the eventual breakdown of a solid.

Thermoplastic polymers can have both brittle and ductile fracture behaviours while glassy thermosets have brittle fracture at low temperatures and brittle or ductile fracture at high

temperatures. Polymers often suffer crazing before brittle fracture. Crazes are associated with regions of highly localized yielding which leads to the formation of interconnected microvoids [63, 64].

4-5-2- Creep

In elastic solids, as shown in Figure 4-3, strain pattern exactly follows the pattern of loading with exact proportionality to the magnitude of applied loads. Although there are some similarities in response of a viscoelastic material to loading, some differences still exist. In the most general case the total strain of ε is the sum of three separate parts ε_1, ε_2 and ε_3 where ε_1 and ε_2 are termed the immediate elastic deformation and the delayed elastic deformation respectively and ε_3 is the Newtonian flow, the part of deformation which is identical with the deformation of a viscous liquid obeying Newton's law of viscosity.

However, because of the linear behaviour of the material, the magnitude of the strains is exactly proportional to the magnitude of the applied stress. Thus a simple creep compliance J(t) is defined as only a function of time:

$$\frac{\varepsilon(t)}{\sigma} = J(t) = J_1 + J_2 + J_3$$

where J_1, J_2 and J_3 correspond to ε_1, ε_2 and ε_3 respectively.

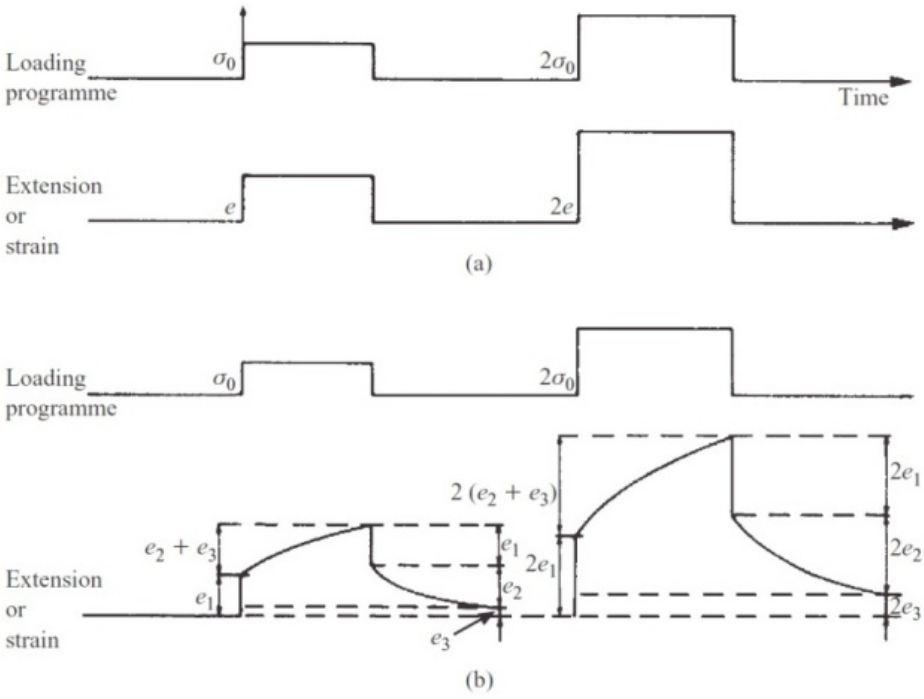

Figure 4-3- (a) Deformation of an elastic solid; (b) deformation of a linear viscoelastic solid [63]

As the flow viscosities are very large for rigid polymers at relatively low temperatures, the term J_3, which defines the Newtonian flow, can be neglected. Linear amorphous polymers do show a finite J_3 at temperatures above their glass transition temperature, however below that their behaviour is dominated by J_1 and J_2.

Variation of creep compliance with time at constant temperature over a very wide time scale is shown in Figure 4-4 for an idealized amorphous polymer with only one relaxation transition. This suggests that the observed behaviour will depend on the time scale of the experiment relative to some basic time parameter of the polymer (called the retardation time for creep). The value of this parameter for a given polymer relates to its molecular constitution. This leads to understanding the influence of temperature on polymer properties. [61, 62].

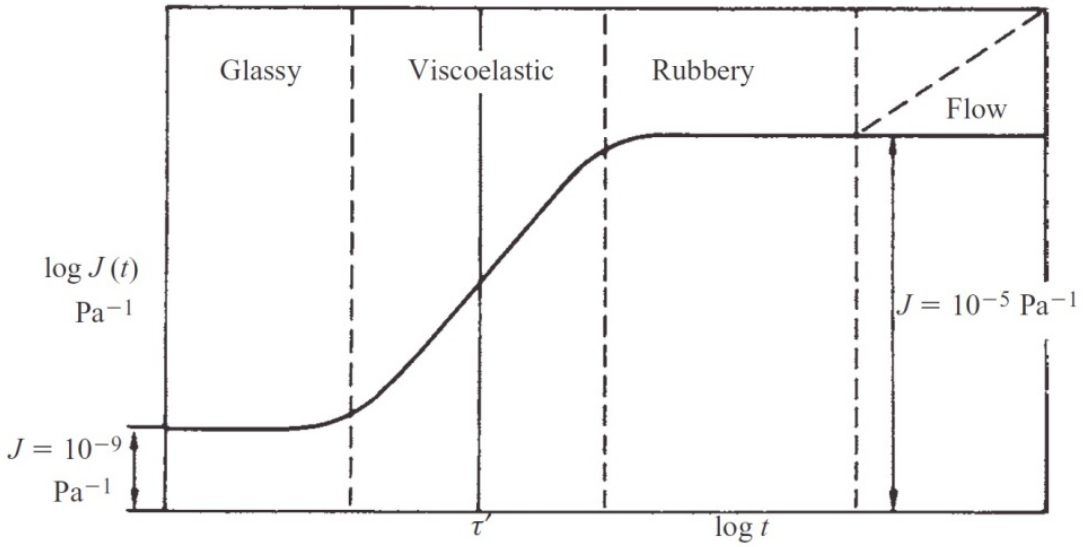

Figure 4-4-The creep compliance J(t) as a function of time t; $\tau'$is the characteristic time (the retardation time) [63]

4-6- Summary

An introduction to polymer materials and their properties has been provided in this chapter. As stated, polymers performance under dynamic loading depends on their molecular properties and the loading and experimental conditions such as environment, frequency and temperature. The following chapter looks into fatigue properties of polymers.

5. Fatigue of Polymers

5-1- Introduction

The increasing demand of engineering polymers for load-bearing applications in the past decades requires a thorough understanding of their fatigue performance.

The phenomenon of fatigue is generally described as the loss of strength or other important properties as a result of cyclic loading [67]. Subject to fluctuating loads, materials fail at stress levels much lower than their strength under monotonic loading conditions, and the time of their failure for a constant applied stress is much less than their creep rupture time. These aspects lead to a considerable technological interest in improving the fatigue resistance of polymers [68].

In order to do this, understanding the mechanisms involved in the fatigue failure of polymers, the influence of important external or experimental variables and significant material variables is of utmost importance. This chapter introduces the fundamental aspects influencing the fatigue life of polymer components.

5-2- Failure Mechanisms

Fatigue failure in polymers can occur by either thermal softening or pure mechanical failure or a combination of the two effects, depending on the stress amplitude and frequency of load application.

5-2-1- Thermal Fatigue

Under cyclic loading of polymers, some energy is dissipated in each cycle due to their viscoelastic nature. If the rate of heat dissipation in the part is higher than the heat transfer rate out of it, this leads to a temperature rise in the test specimen up to a point it can no longer withstand the load and experiences a thermal failure. This phenomenon is known as hysteresis heating and is one of the major causes of fatigue failure in polymers. Thermal effects are promoted by the use of high frequencies, high stress levels and polymers with large viscoelastic effects. [66-68].

The quantity of heat liberated per unit volume during one cycle is proportional to the work of deformation irreversibly expended as a consequence of hysteresis:

$$Q \sim \sigma_0 \varepsilon_0 Sin\delta \qquad (5\text{-}1)$$

where σ_0 and ε_0 are respectively the stress and strain amplitudes and δ is the phase angle between them.

The specific form of this relation is determined by the test conditions. Two systems are widely used in practice; given strain amplitude (ε_0= constant) and given stress amplitude (σ_0 = constant).

Since a temperature rise leads to a fall in modulus, the system with constant strain amplitude corresponds to a decrease in the resulting stress amplitude which leads to a decrease in the work of deformation, and hence a fall in heating. In this event we get rapid stabilization of temperature and thermal failure does not occur.

On the other hand, in the case of constant stress amplitude, the same process (a fall in modulus with temperature rise) leads to a completely different phenomenon. Here we get an increase in strain amplitude and, consequently, an increase in the work of deformation, which means increased heat release leading to thermal failure [71].

5-2-2- Mechanical Fatigue

Mechanical failure of polymers under alternating loading conditions usually involves initiation of a craze or of a damage zone, developed from a surface stress concentration site in unnotched specimens. This is followed by development of a cavity or micro-crack in the plastically deformed region with subsequent crack propagation until some critical crack size is reached at which catastrophic fracture occurs [70]. In notched test specimens a damage zone is formed at the crack tip.

5-3- Fatigue Testing

5-3-1- Purposes of Fatigue Testing

The purposes of fatigue testing are:

To estimate the relationship between stress- (load-, strain-, deflection-) amplitude and cycle life-to failure for a given material or component

To compare the fatigue properties of two or more materials or components.

For these estimates to be reliable, the results of the testing sample should be drawn at random from a population of specimens and tested in accordance with acceptable testing procedures [72].

5-3-2- Fatigue Test Variables

In order to conduct a fatigue test, certain control variables should be established based on the objective of the test.

Stress-Controlled Testing

The magnitude of alternating stress or stress range and the amount of mean stress have been found to have a strong effect on the fatigue life of a component [68, 69]. From the stress- log cyclic life plots (often referred to as S-N curve diagrams) achieved from different polymers, it can be revealed that the cyclic life of any material increases with decreasing stress amplitude. Also, below a certain stress level, some materials seem to possess infinite life.

In these types of tests, failure may take place by either of two modes: nucleation and growth of a crack or hysteresis heating. Hysteresis heating, in this case, leads to a decrease in elastic modulus. As a result larger deflections are generated under constant stress conditions, contributing to even greater energy losses and producing an auto-accelerating tendency for rapid specimen heating. A point is reached whereby the specimen is no longer capable of supporting the loads introduced by the test machine within the deflection limits of the test apparatus [67].

Deflection-Controlled Testing

Some components in some situations are loaded with certain limits of deflections, such as various springs and shoe soles. For these cases, it is found that the initial stress range induced by the applied deflection limits decay with repeated cycling as shown in Figure 5-1. ASTM standards have suggested defining the fatigue life when the stress level decreases to 70% of its initial value [72].

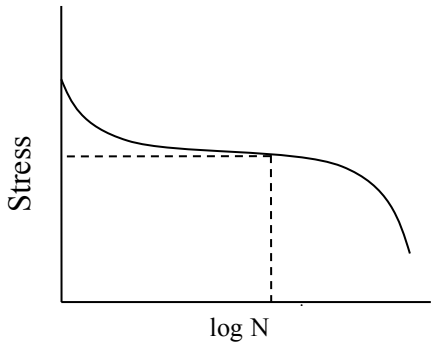

Figure 5-1- Stress decay curve. Fatigue life N^* corresponds to cyclic stress level equal to 70% of initial stress value

During this kind of fatigue testing, cyclic-induced material property changes may also occur and it is argued that stresses should not be calculated from deflection-controlled test conditions, in case they are not being monitored, due to dynamic modulus changes during the test.

The advantage of deflection-controlled testing is a decreased tendency toward hysteretic heating, as the applied stress decreases under these conditions. It should be noted that the fatigue behaviour of polymers may well depend upon the nature of the fatigue test itself, as a result of the hysteretic heating characteristic of them [67].

Strain-Controlled Testing

A close connection exists between constant-deflection and constant-strain testing. The most important of which is neither of the test conditions lead to thermal failure.

Strain-controlled fatigue tests are thought to be useful in evaluating the cyclic life of components that contain blunt notches and other moderate stress concentrations, most of them conducted under fully reversed tension-compression loading conditions [68].

Although the number of studies performed on polymers is relatively small, almost all of them report observation of cyclic softening in polymers subject to strain-controlled fatigue [61, 63, 70, 71] an example of which is illustrated in Figure 5-2.

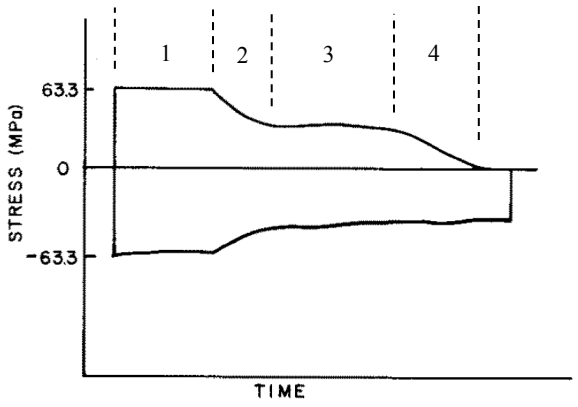

Figure 5-2- Variation of maximum tension and compression stress in PC at an alternating strain of 5%- the cyclic softening stages are illustrated in the graph [68]

For the case of ductile polymers such as Polycarbonate (PC) and Nylon 66 four distinct regions are observed [72].

1-The incubation state, where the stress is essentially constant, is a variable of both the initial state of the material and the imposed strain amplitude. At sufficiently high strain amplitudes, the sample might begin to soften on the first cycles.

2-The transition stage where the stress response reduces in both tension and compression as cyclic softening sets in. In this region the stress-strain curve changes rapidly with the peak stress decreasing and the cyclic hysteresis increasing from one cycle to the next. The transition region extends over a few cycles in all ductile polymers. However, the changes

induced in mechanical response and molecular packing in this region have a profound effect on the fatigue resistance of the material.

3-The cyclic steady state stage in which the polymer is in fully softened condition. In this stage the ductile polymer maintains a new, steady-state stress-strain relation as cyclic deformation proceeds. The energy dissipated from cycling of the specimen through a complete cycle remains constant from one cycle to the next.

4-The final crack propagation stage prior to fracture, where the tensile stress peak decreases from cycle to cycle due to the increase in crack area and the compressive stress peak remains approximately constant. In this stage, when the crack attains a critical area, catastrophic tensile fracture occurs over the remainder of the surface.

A contradiction to the above results, would be a study performed by Tao and Xia [64] on an epoxy resin where, under strain-controlled testing condition, the material response has switched from cyclic softening to cyclic hardening for larger mean strain ratios.

5-3-3- Effect of Test Conditions

Various test conditions including cyclic frequency, test temperature, loading rate and environment have an effect on the test results.

Frequency

The influence of test frequency, to a great extent, depends on the viscoelastic nature of the polymer in the temperature region of investigation. In polymers where hysteresis heat losses are significant, great energy dissipations are caused by an increase of frequency [65].

Arad et al [75] investigated the strain rate dependence of the failure process in Polycarbonate and Nylon 66 specimens in cyclic tests at frequencies ranging from 0.1 to 20 Hz. Fatigue crack growth rate in both materials was influenced by variations in loading frequency and cyclic waveform. The trend in the variation of the cyclic rate of crack growth with frequency was found to be consistent throughout the range of tests on Nylon, i.e. a gradual decrease in crack growth rate as frequency is raised. In the case of PC, however, this trend was not continuous throughout the whole range of test frequencies.

Temperature

In several polymers, lifetimes to fracture decrease and fatigue crack propagation (FCP) rates increase subject to temperature rise. Martin et al [79] studied effect of temperature change in a range between -172-100°C on fatigue crack growth of notched Polycarbonate samples and reported that fatigue resistance of the samples decreases with rising temperature at temperatures above -50°C. Similarly, in a study by Mai et al [80] on effect of temperature on fatigue properties of Polystyrene parts, it was shown that crack growth rate increases with increase in temperature. However, studies have shown an increase in the fatigue resistance of nylon 66 when exposed to elevated temperature prior to testing [68].

Stress/Strain variables

As a result of their viscoelastic properties, polymers behave with sensitivity to the application of different loading modes, stress amplitudes, strain amplitudes, strain rates and wave forms. Various studies have been conducted on the effect of these parameters on fatigue behaviour of different polymers [68, 69, 73, 74].

Shen et al [81] carried out a series of stress-controlled and strain-controlled cyclic loading with and without mean stress/strain at various amplitudes and loading rates on an epoxy resin. They discovered that the cyclic stress-strain response of the material was amplitude-dependent and rate-dependent. For stress-controlled cyclic loading with mean stress, ratcheting strain was accumulated, which was of viscoelastic nature. For strain-controlled cyclic loading with mean strain, the mean stress relaxation occurred, which contributed to the observed longer life in comparison to the stress-controlled cyclic loading with mean stress.

Environment

Since fatigue fractures in most polymers develop from surface sources, fatigue behaviour is sensitive to the environment and enhancement, or deterioration, of fatigue resistance should be possible by use of appropriate surface environments [68].

Bretz et al [82] investigated the effect of moisture on fatigue crack propagation of Nylon 66 parts and reported that the FCP rates decreased as the water content increased to about 3%. However, the FCP rates were reportedly higher at saturation (8% water content) than that observed in dry specimens.

5-3-4- Material Variables

As described in section 4-5, mechanical response of polymers is not only sensitive on test conditions, but it also highly depends on their molecular structure and material variables and fatigue is no exception to this rule. Fatigue performance of polymers is sensitive to a number of material and molecular variables. These variables include glass transition temperature, molecular weight, crystallinity and cross linking [83].

Glass Transition Temperature

The heat released per unit time $\dot{Q}$ is determined by the following relationship;

$$\dot{Q} \sim \sigma_0^2 \omega \frac{Sin\delta}{E} \qquad (5\text{-}2)$$

where ω the cyclic frequency, and E is the dynamic modulus of elasticity.

It can be observed from this equation that the heat generation rate within the polymer is dependent on the $\frac{Sin\delta}{E}$ ratio, which highly depends on the glass transition temperature of the polymer. As the polymer reaches its glass transition temperature region, which is also characterized as the softening temperature, the modulus drops sharply and δ gets to its peak resulting in a large $\frac{Sin\delta}{E}$ ratio and as a result higher energy release rates leading to rapid failure of the part [71]. Therefore, it is assumed that polymers with higher T_g have a longer fatigue life than polymers with lower T_g, as more cycles is required for them to reach the rapid energy release state.

Molecular Weight

As described in section 5-2-2, fatigue fracture is initiated by crazing and formation of a damage zone at the crack tip in glassy and semi-crystalline polymers respectively. This leads to initiation of a microcrack, which propagates through the crazed or damaged zone with subsequent cycling. As a result, if craze strength could be enhanced and chain rupture could be inhibited more fatigue cycles could be endured and a higher stress, for a given number of

cycles, could be realized. One promising means of doing this is to increase molecular weight [68].

Increase of molecular weight has been shown to increase craze stability and in some polymers there is evidence of a delay in the craze initiation process. Also, many craze parameters such as craze length, craze width and craze density are molecular weight dependent and increase with increase of molecular weight. Therefore, increase of molecular weight, leads to improvement in fatigue life of two to three decades and to greater resistance to fatigue crack propagation [84].

Sauer et al [85] have shown that increase of molecular weight not only increase the fatigue life of the polymer, it also increases the endurance limit of both amorphous and semi-crystalline polymers.

Microstructure

In general, semi-crystalline polymers are considerably more fatigue resistant than are the glassy amorphous polymers. This is attributed to two characteristics. First, the two-phase structure of semi-crystalline polymers, with rigid crystallites imbedded in a compliant amorphous phase, offers more resistance to crack propagation. Another reason is that crystallite deformation modes can absorb some of the fracture energy [68].

It is reported that if fatigue failure due to excessive thermal heating is avoided, at comparable molecular weights, fatigue resistance and endurance limit of semi-crystalline polyethylene is considerably greater than that of amorphous polystyrene [86]. Also, Starkweather et al. [87] have discovered an increase in the fatigue crack propagation resistance and endurance limit of nylon polymers with increased crystallinity.

Fatigue threshold of ultra-high molecular weight polyethylene (UHMWPE) is reported to be highly sensitive to local microstructure and it is believed that this behaviour is linked to orientation of the lamellae and tie molecules relative to the advancing crack front. Thus, it is expected for any process which alters the microstructure of the polymer to affect its near-threshold fatigue behaviour [88].

Cross-linking in polymers is also considered to affect their fatigue performance [68]. Cross-linking, whether carried out by chemical or irradiation means, generally increases rigidity,

and reduces ductility. This prevents creep or crazing of the material, causes embrittling of the polymer, inhibits local plastic deformation and leads to possible crack tip blunting. Thus lower fatigue crack resistance is expected.

5-4- Summary

An introduction to fatigue and failure mechanisms of polymers has been provided in this chapter. Cyclic testing variables were presented and the effects of testing conditions and material parameters were reviewed, showing that fatigue behaviour of polymers is significantly dependant on these conditions. The present study attempts to provide this information for LS polymer parts.

6. Hypothesis and Research Objectives

6-1- Background

LS is proved as a suitable AM approach for producing medical, automotive and aerospace applications due to the chemical stability and initial mechanical properties of the parts. However, use of LS parts is still somewhat limited in long-term applications, which is partly due to the lack of information on their in-service behavior. Although tensile properties of LS Nylon 12 have been largely investigated and reported to be comparable with injection molded specimens, dynamic behavior of these parts has scarcely been studied.

As described in Chapter 5, several factors, both internal and external, have been identified as parameters that could influence cyclic performance and fatigue life of polymers. Therefore, any parameter that is considered to affect the internal structure of the polymer parts might influence their cyclic performance as well. Structural properties of the polymers such as molecular weight and degree of crystallinity, are influenced by the manufacturing process and parameters associated with it.

As described in Chapter 3, one of the distinctive advantages of LS is the freedom of design offered by this technique, which enables optimisation and design options leading to creating parts with complex geometries. However, very little investigation has been made into the effects of geometry on mechanical properties of the parts. Datasheet values reported by manufacturers for many commonly required properties are only for standard specimen sizes.

It has been suggested that properties of parts with varying section-thicknesses might be different due to different thermal conditions they experience which may ultimately lead to different molecular parameters.

Source of fatigue crack initiation has been identified as either surface defects such as scratches or tool marks, or internal defects such as inclusions and voids [66, 81]. During the LS process the high temperature sintered powder is in contact with the unsintered powder cake surrounding it. As a result, unsintered or partly sintered powder particles attach to the surface of parts. Due to unfused powder particles attached to their surface, LS parts have a rougher surface than IM parts. Micrographs of the surface of a LS part are shown in Figure 6-1.

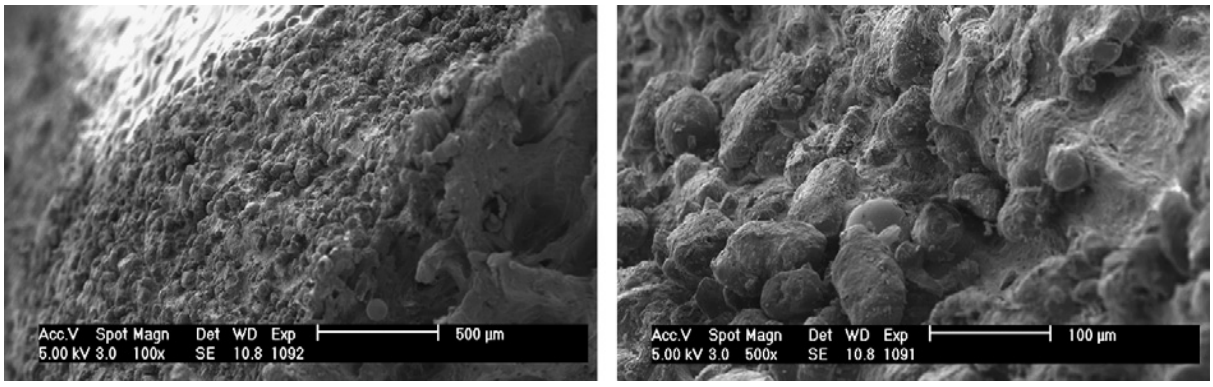

Figure 6-1- Unfused powder particle on the part's surface [50]

While achieving a higher level of porosity is an advantage in production of porous structures, the presence of porosity in Laser Sintered parts is known as one of the shortcomings of this manufacturing technique. Increased percentage of porosity which leads to lower density of parts has been anticipated to affect mechanical properties of porous parts manufactured by both conventional and additive manufacturing techniques [31, 48, 96, 97].

Various studies on fatigue of polymers have identified hysteresis heating and thermal failure as the main cause of fatigue failure in different polymer materials [68, 92, 93]. However, this effect has not been extensively studied in AM parts previously and no studies have investigated if the temperature rise relates to geometry of parts.

6-2- Hypothesis

In this study, it was hypothesized that the imperfections caused by the unfused particles, might initiate the nucleation of flaws and lead to initiation of a fatigue crack. Since the ratio of powder particle size to section thickness is smaller in thinner samples, this effect was hypothesized to have greater influence on fatigue performance of parts with smaller section thicknesses. It was also hypothesized that parts with different section thicknesses would show different fatigue performances due to their molecular variables induced by thermal conditions.

Another hypothesis was that the pores induced in the samples as a result of the sintering process could influence their fatigue performance by acting as crack initiation points. Therefore, parts with higher porosity would have lower fatigue lives and worse performance under cyclic loading, same as other mechanical loading conditions.

6-3- Objectives

Based on the background information and the hypothesis provided, objectives of this research work were defined as follows;

Investigate the viscoelastic behaviour of the LS Nylon 12 parts, and understand its dependence on temperature and frequency to obtain a better understanding of the dynamic performance of the parts.

Investigate the fatigue performance of LS Nylon 12 parts with different section thicknesses subject to tension-tension cyclic loading.

Investigate the influence of section thickness on tension-compression cyclic performance of LS Nylon 12 parts.

Investigate the influence of porosity on cyclic behaviour.

Investigate the thermal behaviour and thermal history of the parts subject to cyclic loading with a low frequency.

7. Viscoelasticity and Mechanical Properties

7-1- Introduction

Polymers are viscoelastic materials whose performance changes with time and temperature. To get a better understanding of the behaviour of the material, it is important to establish how and to what extent these changes occur. Therefore conducting an experiment to determine the material's viscoelasticity, and its changes by time (frequency) and temperature is vital. This chapter describes the stages through this process.

7-2- Methodology

The objective of these series of experiments was first to obtain a better understanding of the viscoelastic behaviour of LS Nylon 12 i.e. to determine changes of mechanical properties of the material with temperature and frequency. The second objective was to determine mechanical properties of the samples based on their section thickness. The results from these tests were employed to establish the test conditions in investigating the cyclic performance of parts.

To assess the viscoelastic performance, Dynamic Mechanical Thermal Analysis (DMTA) was employed, in which a cylindrical specimen made of LS Nylon 12 was cycled in a closed chamber with low strain while the temperature and frequency of the test were varied step by step.

For mechanical testing, tensile test Nylon 12 samples with three different section thicknesses were designed and manufactured. Tensile tests were performed to measure the Elongation at Break (EaB), Ultimate Tensile Stress (UTS) and Young's Modulus of the parts for each section thickness.

7-3- Test Sample Design

DMTA test parts were designed in the shape of a simple cylinder with the dimensions shown in Figure 7-1 based on test machine requirements.

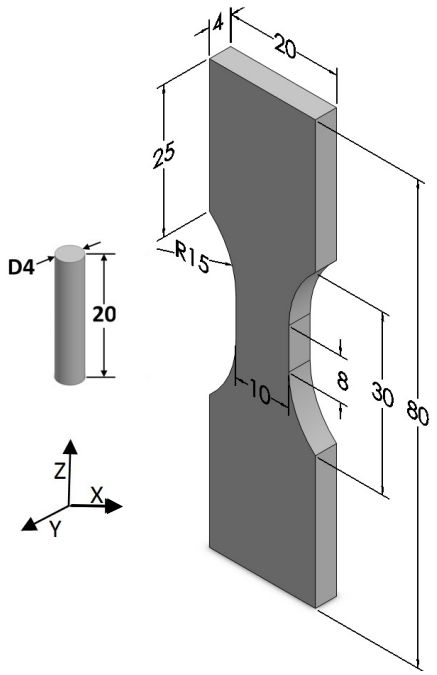

Figure 7-1- Dimensions of the test specimens (all dimensions in mm)

In designing of the mechanical test specimens several issues were considered. It was decided for the sample geometry to remain unchanged for both mechanical and cyclic testing. Samples were supposed to be made at three different section thicknesses and the thinnest section thickness was to be small enough so the ratio of particle size to section thickness was

considerable. Section thicknesses of the samples were chosen as 2, 4 and 6mm based on robustness, particle size to section thickness ratio and grip size.

Since cylindrical samples, as suggested by ASTM for compressive loading, with smaller diameters would buckle instantly under compressive load, length of the samples was reduced based on the effective length found from buckling analysis. Buckling analysis was performed for the maximum load assumed to be applied on the thinnest samples. Eulor's column formula (Equation 7-1) was employed for this analysis.

$$F = \frac{\pi^2 EI}{(KL)^2} \qquad (7\text{-}1)$$

Where;

F=600N based on a stress level equal to 70% of the reported values for UTS of LS Nylon 12 (as required by ASTM for producing S-N curves)

E=2GPa based on values reported by literature for Young's Modulus of LS Nylon 12

K=0.5 as the column is assumed to be fixed on both ends

Cross-section of the column=2mm×10mm (thickness of the thinnest sample×width of ASTM tensile samples)

These values result in L=30mm, which was chosen as the effective length of the samples.

7-4- Part Manufacturing

All specimens (DMTA and cyclic loading) were manufactured in one build of a CO_2-laser EOS P100 laser sintering machine to eliminate any possible difference in build conditions of different runs. Mixed (50% virgin, 50% used) EOS PA2200, as used by industry, was used to manufacture the parts. Parts were built in the ASTM zx direction with their long axis perpendicular to the build platform as shown in Figure 7-2, so that they would be loaded in their most critical direction, and were all manufactured in one horizontal plane. All parts were numbered and positioned on the build platform according to a pattern, so that the exact position of each sample on the bed would be known.

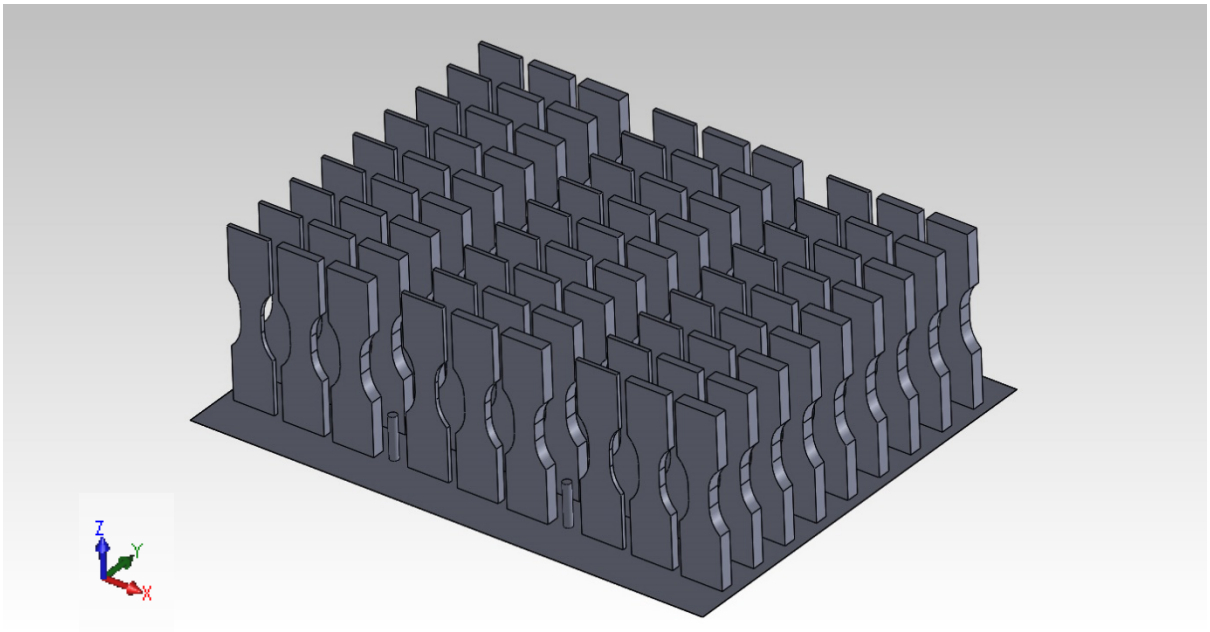

Figure 7-2- Orientation and placement of parts in the build chamber

Standard machine parameters, as shown in Table 7-1, were used for manufacturing of the parts. After the build process, parts were left in the machine to cool down for a duration equal to the build time, and were then removed from the chamber and cleaned.

Table 7-1- Standard process parameters used for the LS build

Process Chamber Temperature	170°C
Laser Power	21W
Speed	2500mm/s
Layer Thickness	0.1mm
Laser Beam Diameter	0.43mm
Scan Spacing	0.25mm

The energy density used to manufacture the samples was equal to:

$$ED = \frac{21}{0.25 \times 2500} = 0.033\, J/mm^2$$

Volumetric energy density can be obtained by dividing the energy density value by layer thickness:

$$Volumetic\ ED = \frac{ED}{0.1} = 0.33\ J/mm^3 z$$

7-5- Dynamic Mechanical Thermal Analysis

Dynamic Mechanical Thermal Analysis (DMTA) is a method to study the mechanical response of viscoelastic materials, subject to a sinusoidal strain, as a function of temperature and time [94].

7-5-1- Theory

When viscoelastic bodies are subjected to sinusoidal loading, their resulting strain is neither in phase with the stress, as in perfectly elastic materials which follow Hooke's law, nor 90° out of phase, as in purely viscous fluids which follow Newton's law. These materials exhibits a characteristic in between where some phase angle (δ) can be observed in the resulting strain [95]. Figure 7-3 illustrates this behaviour.

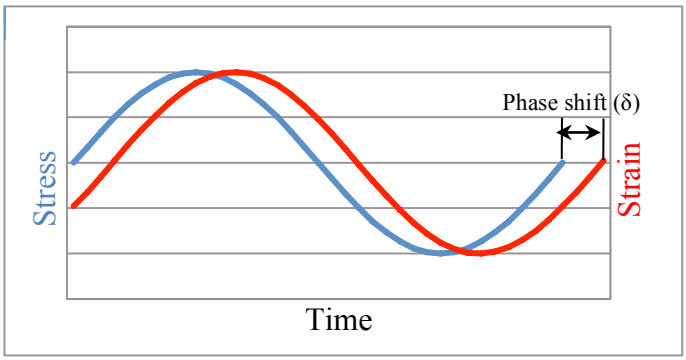

Figure 7-3- The relationship between applied stress and resultant strain and the phase shift

Viscoelastic materials show a combination of both elastic and viscous characteristics, meaning the materials behaviour depends on both strain and strain rate. Two types of moduli are defined for these materials; Storage or elastic modulus ($E^{'}$) which represents the elastic behaviour of the material and its ability to restore energy, and loss or viscous modulus ($E^{''}$) which represents the viscous behaviour of the material and its ability to dissipate energy. The

combination of these moduli provides the complex modulus of the material (E^*). Also, the ratio of the viscous modulus to the elastic modulus is the tangent of the phase angle shift (δ) and illustrates the damping ability of the material[64, 65]. Figure 7-4 and Equations 7-1 and 7-2 show the relations of these parameters.

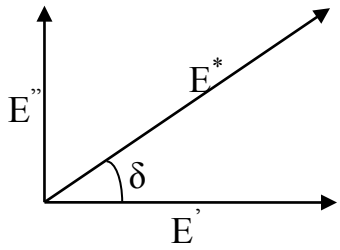

$$E^* = E' + iE'' \qquad (7\text{-}1)$$

$$Tan\delta = E''/E' \qquad (7\text{-}2)$$

Figure7-4- The viscoelastic moduli

The ability to measure these parameters in different temperature and frequencies enables the full characterisation of the viscoelastic material.

7-5-2- Experimental Approach

In order to obtain the viscoelastic behaviour of the material, a test specimen of known geometry is clamped in the fixtures of the machine, one movable and one stationary, and is then enclosed in a thermal chamber. A sinusoidal deflection with very small amplitude is applied to the sample with a defined frequency while the analyser slowly moves through the specified temperature range, and the force required to produce this deflection is measured.

In addition to selecting the rate of temperature change, the frequency of oscillation can be controlled across a range, to study the frequency dependent behaviour of the material. The stiffness of the specimen (K) is the ratio of the force amplitude to the displacement amplitude, which depends on the specimen geometry.

The complex modulus of the specimen can then be calculated using the stiffness, and its real part, in phase with the displacement, forms the elastic modulus, while the imaginary part, out of phase with the displacement, forms the viscous modulus. The data provided by the machine is elastic modulus (E'), viscous modulus (E'') and loss factor (Tan Delta) versus temperature or frequency [83–85].

7-5-3- Data Analysis

Various characteristics of the viscoelastic material can be determined using the data obtained from DMTA. These characteristics are described in this chapter.

Temperature Dependant Behaviour

In order to study the temperature dependant behaviour of the viscoelastic material, typically the storage modulus, loss modulus and tan delta are plotted against temperature.

The storage modulus plot presents a full picture of the load-bearing characteristics of the material as a function of changes in temperature while the loss modulus and tan delta curves help to identify the regions where relatively large changes in properties occur over relatively narrow bands of temperature. These regions show material transition stages and the most important of them is the glass transition. The glass transition region can be observed in the plots as a rapid decrease in the storage modulus and a maximum peak in the loss modulus and tan delta [95].

Degree of Crosslinking and Crystallinity

Although in amorphous systems, the glass transition results in a large loss in storage modulus, normally two to three orders of magnitude, in semi-crystalline and crosslinked systems the reduction is less severe due to the supporting influence of the crystalline or crosslinked network. Therefore, in a given material system the decline in storage modulus associated with the glass transition is a relative indicator of the degree to which the structure is more ordered [97].

Time-Temperature Superposition Principle (Master Curve)

The principle articulates that temperature has no influence on the shape of the plot for the relationship between viscoelastic parameters versus frequency or time. Thus data obtained for a range of isotherms covering a few decades of frequency or time is shifted empirically along those axes to produce a master curve. The shifting is conducted using Williams-Landel-Ferry (WLF) equation (Equation 4-9 in section 4-4-3) and the resultant plot is known as a Master Curve of the material, which is a curve of the viscoelastic parameters in frequency out of the range of the data collection [98].

7-6- DMTA Testing Method

As described in sections 7-3 and 7-4, a cylindrical sample, made by laser sintering of EOS PA2200 (50% virgin, 50% used) using an EOS P100 machine and by standard machine parameters recommended by the EOS Company, was used for this experiment.

A viscoanalyzer system by Metravib was employed to perform Dynamic Mechanical Thermal testing on the sample. A schematic of the test setup is illustrated in Figure 7-5. In order to calculate the Moduli of the material, the machine requires exact dimensions of the sample. Measured by Vernier callipers the dimensions of the sample were recorded as: a diameter of 3.97mm and height of 20.25mm. To minimize error, three measurements from different parts of the sample were made and averaged.

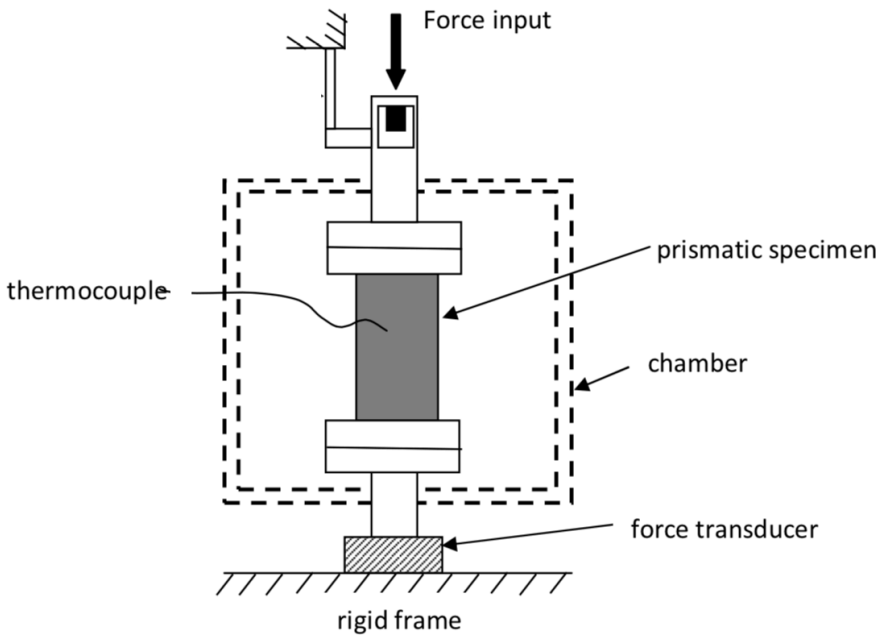

Figure 7-5- Schematic of the DMTA setup

Based on the instructions by ASTM D5026 standard for dynamic mechanical properties of plastics, a sinusoidal strain of 0.001 (measured by the machine) was defined as the input signal of the machine. The applied strain value is very small to avoid hysteresis heating of the sample during testing. The machine parameters were then set as a starting temperature of 26.5˚C, the room temperature in the laboratory, and a final temperature of 110˚C. The Sample was heated at a 2°C/min rate and the stabilisation period between each heating cycle was 2 minutes, so that the sample was heated evenly. The frequency was also set to vary in

each temperature step from 1 to 100 Hz in 11 different steps. Figure 7-6 shows the sample set up in the machine before the testing was started.

Figure 7-6- DMTA experimental setup

The machine measures the stiffness of the material in each step, which is then used by the Dynatest software to calculate the moduli and loss factor of the material. The sample was bonded to the fixtures with super glue and was then sealed in the thermal chamber to enable change of temperature during the experimental process.

7-7- Mechanical Experiments

In this section measurement of physical properties of parts and experiments leading to assessing tension-tension fatigue performance of the samples are explained.

7-7-1- Measurement of Physical Properties

The temperature evolution history in LS process has a significant influence on the properties of parts such as dimensions and mechanical properties due to mechanical stresses induced as a result of temperature variation during the process [99], [100].Therefore, the distribution of temperature on the powder bed surface should be as homogeneous as possible to achieve equal part properties throughout the whole build space, minor part warpage and narrow tolerances. However, experience shows very inhomogeneous temperature distributions [101].

Due to this variation in properties and to ensure test samples were chosen from a random population, physical properties i.e. weight, dimensions and surface roughness of the samples were measured and presented as Manhattan charts with regards to parts position in the build bed. It could be observed from the results that all section thicknesses built at the far left corner of the bed had larger mass and cross-sectional areas than other parts within the same range of section thickness, which implied that bed temperature must have been higher at this corner. These results were also employed in next chapters to find a correlation between the varying behaviour of samples with the same section thickness and their physical properties.

Weight

Samples were weighed by a laboratory scale. Figure 7-7 shows Manhattan charts of the samples' mass versus their location on the build platform for each section thickness.

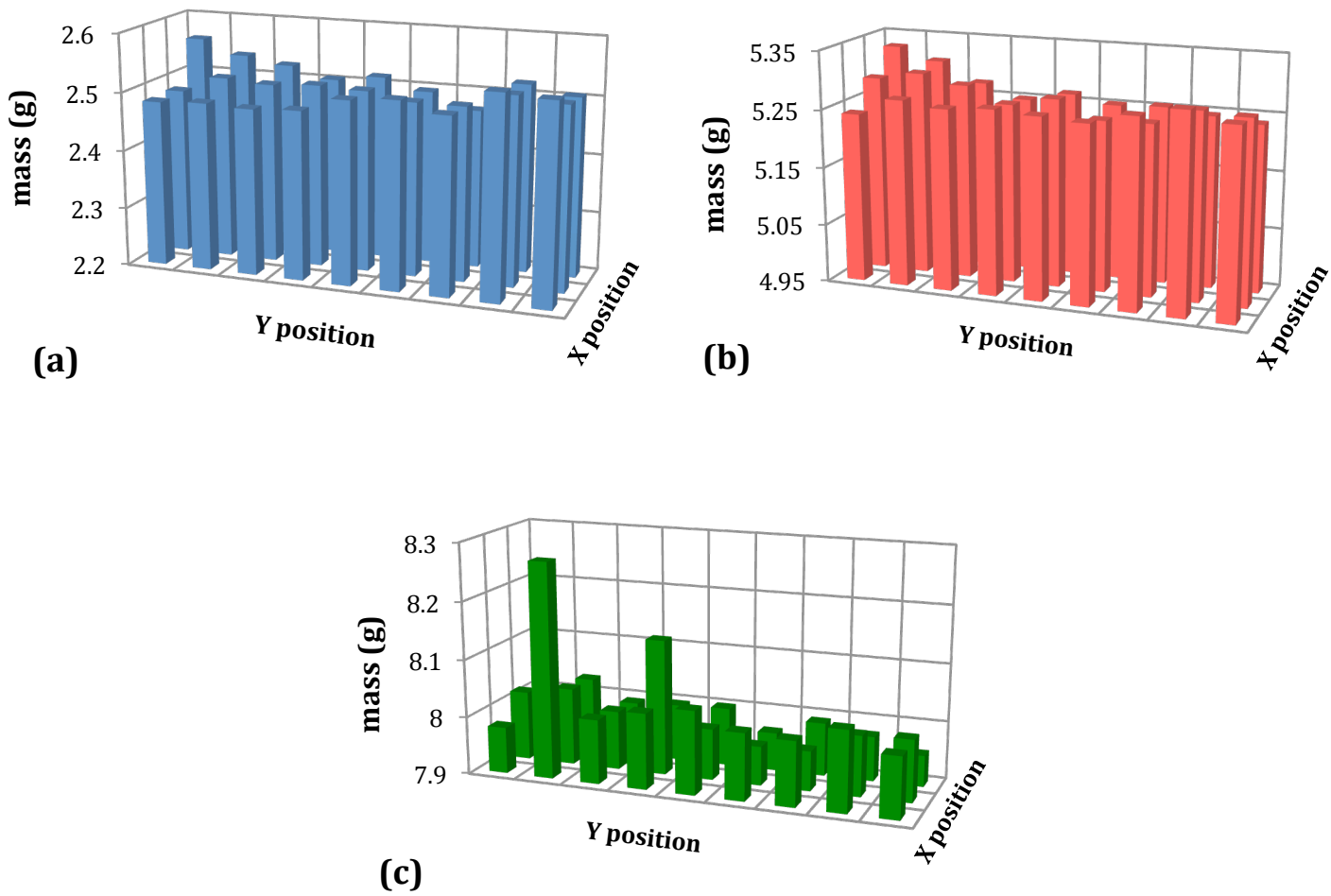

Figure 7-7- Manhattan charts of a) 2mm b) 4mm and c) 6mm samples' weight versus their location on the build platform

Dimensions

Height, Width, and Cross sectional dimensions of the gauge area of the samples were measured using Vernier Callipers. Three measurements were made on each dimension and averaged. Cross sectional areas of the parts in different locations of the build platform are shown in Figure 7-8.

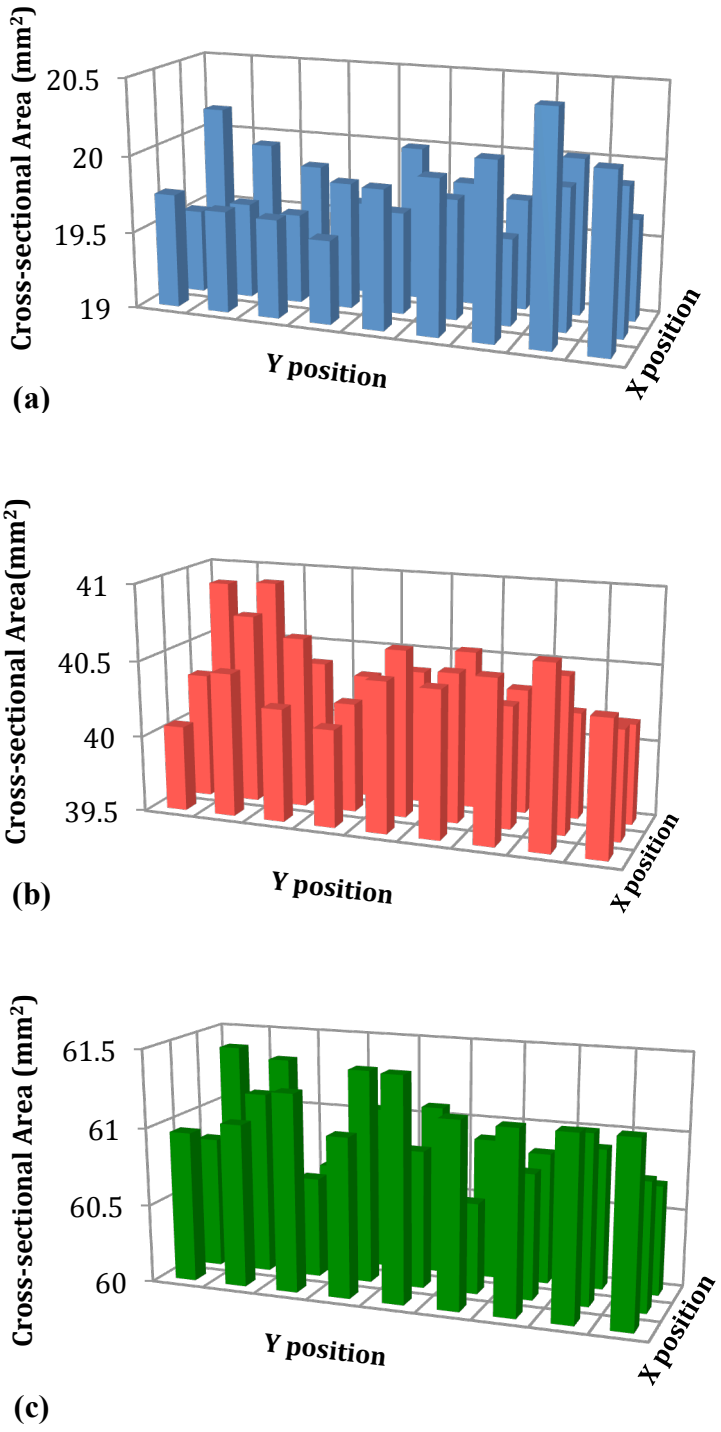

Figure 7-8- Manhattan charts of a) 2mm b) 4mm and c) 6mm samples' cross-sectional area versus their location on the build platform

Surface Roughness

Surface roughness of the samples was measured by a Surftest column type apparatus. A measuring probe with radius of 1μm was used to scan a straight track of 30mm in the longitudinal direction at 0.5mm/s and average surface roughness (R_a) was recorded. Special care was taken to limit the measurement force. Surface roughness of parts with accordance to their position on the build platform are shown in Figure 7-9.

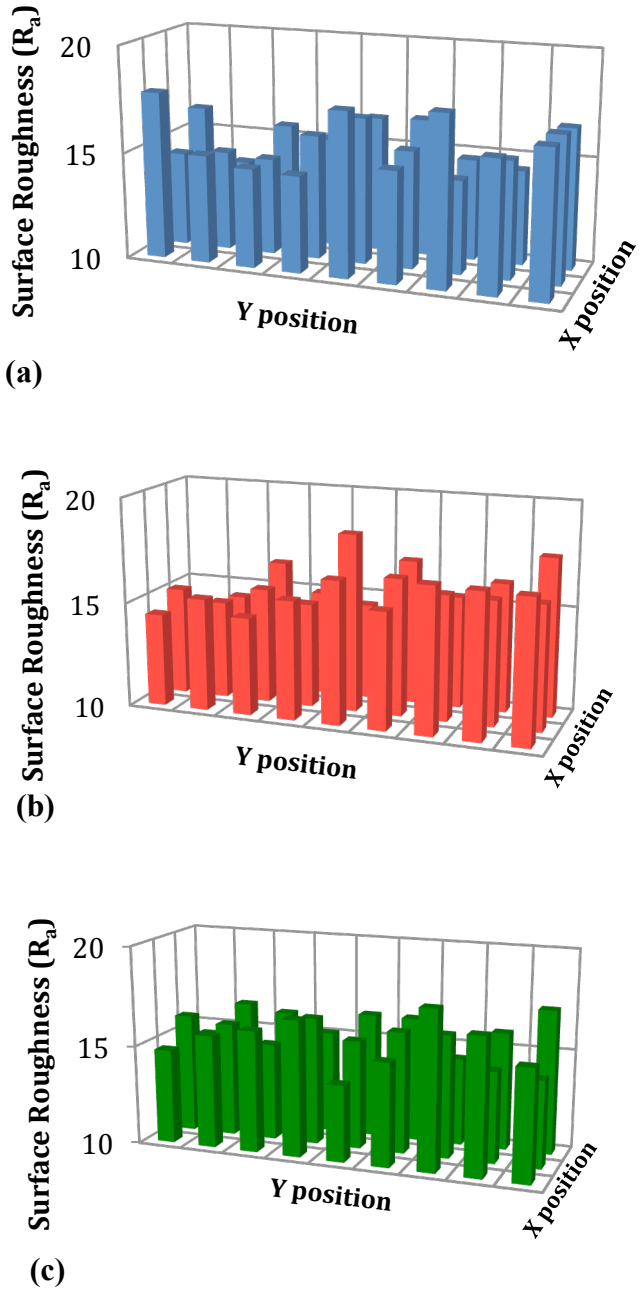

Figure 7-9- Manhattan charts of a) 2mm b) 4mm and c) 6mm samples' surface roughness versus their location on the build platform

7-8- Tensile tests

In order to measure the Elongation at Break (EaB) and Ultimate Tensile Strength (UTS) of the samples, to employ as a starting point in the cyclic tests, tensile tests were conducted on the specimens. Tests were performed by an MTS 858 Table Top System and were set up as shown in Figure 7-10(a).

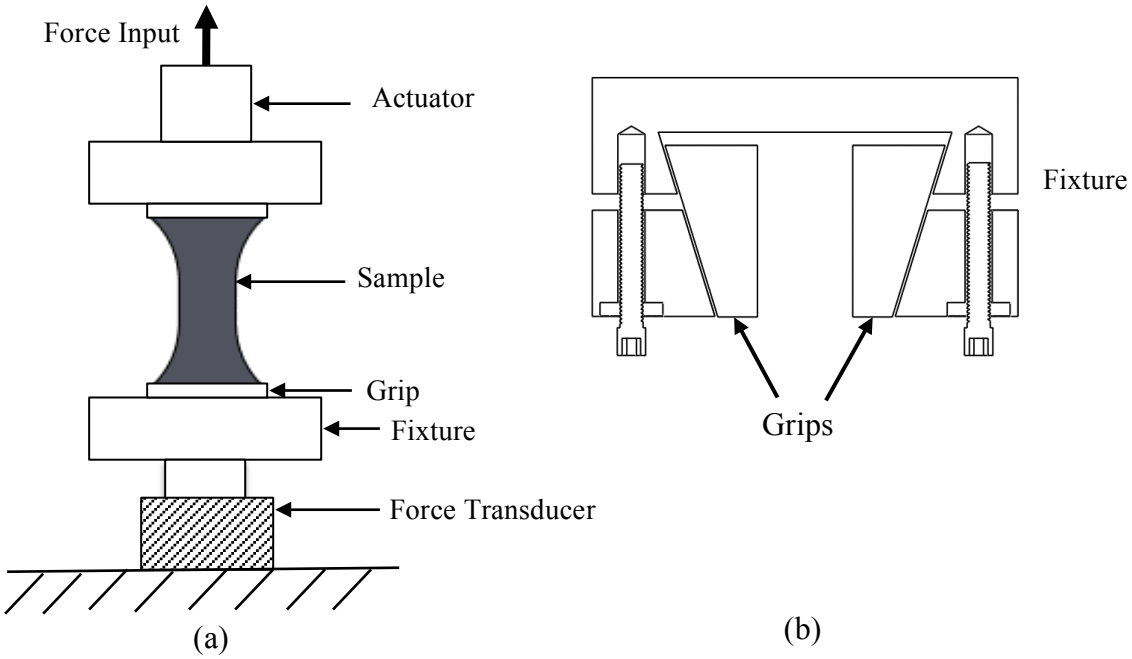

Figure 7-10- a) Schematics of the experimental setup, b) section view of the top fixture

Test Specimens were stored in lab conditions of 25±2ºC and 50±10% relative humidity for at least 48 hours prior to testing. 15 specimens, 5 of each section thickness, were fixed in the machine using wedge grips (as shown in Figure 7-14(b)), to prevent slipping and sliding of the samples while being pulled, and an increasing displacement with 5mm/min rate was applied to the samples until they broke while the force was recorded.

7-9- Results and Discussion

7-9-1- Dynamic Mechanical Thermal Analysis and Viscoelasticity

As discussed in the previous section, various graphs can be produced from the experimental data depending on the required application.

Temperature Dependent Behaviour

Figure 7-11 shows the change of storage modulus (E'), and loss factor (tan delta) of Laser Sintered Nylon 12 with temperature in a frequency range of 1 Hz to 31 Hz.

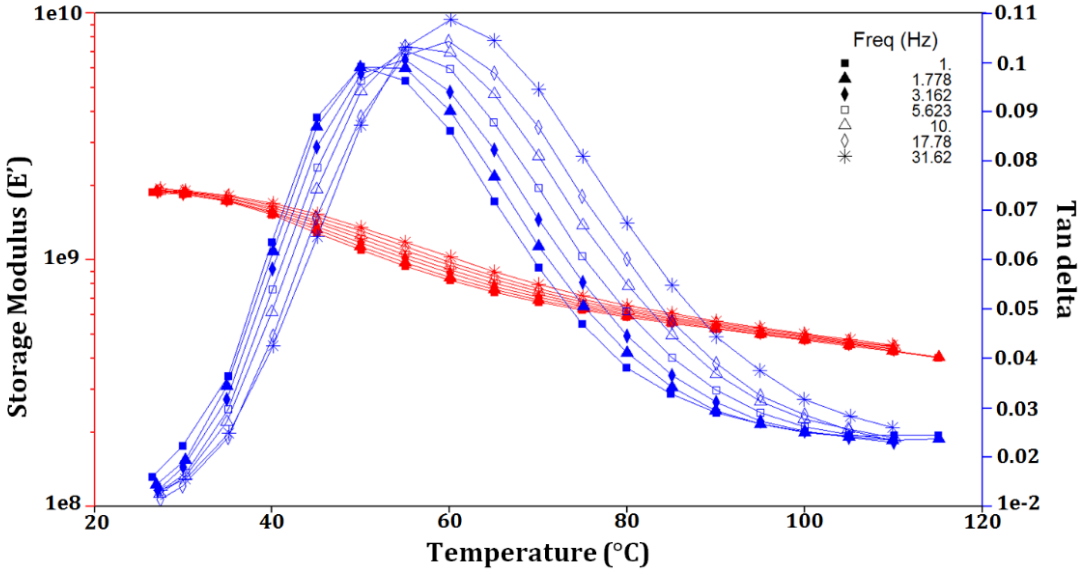

Figure 7-11- Storage Modulus and Loss factor change with temperature in different frequencies

The storage modulus plot (red) presents a full picture of the load-bearing characteristics of the material as a function of changes in temperature while the tan delta curves (blue) help to identify the regions where relatively large changes in properties occur over relatively narrow bands of temperature. These regions show material transition stages and the most important of them is the glass transition. The glass transition region can be observed in the plots as maximum peak in the tan delta graphs [59].

The storage modulus of the material at ambient temperature was recorded as 1.9 GPa which is close to the values previously reported (2GPa) [37] and decreases continuously with increase in temperature. The glass transition temperature (T_g) is observed in the range of 48-

62°C at approximately 2 Hz which is comparable to the amounts reported for the solid [102] although the T_g of a polymer changes by the degree of crystallinity [102].

It can be seen in the plot that at higher frequencies, the storage modulus demonstrates higher values and the glass transition temperature shifts to a higher temperature. The glass transition is associated with the beginning of long-range cooperative segmental mobility in the amorphous phase, in either an amorphous or semi-crystalline polymer. In general, any factor that affects segmental mobility and those that influence the free volume available for segmental motion will affect T_g.

Master Curve Derivation

Deriving a master curve provides a basis on the way the moduli or loss factor of the material change in a range of frequencies greater than the ones tested. This information can be employed in subsequent experiments with lower or higher frequencies.

As discussed in section 4-4-3, in order to produce a master curve, the experimental modulus data were plotted for each tested temperature against the frequency range used in the experiment as shown in Figures 7-12 and 7-13.

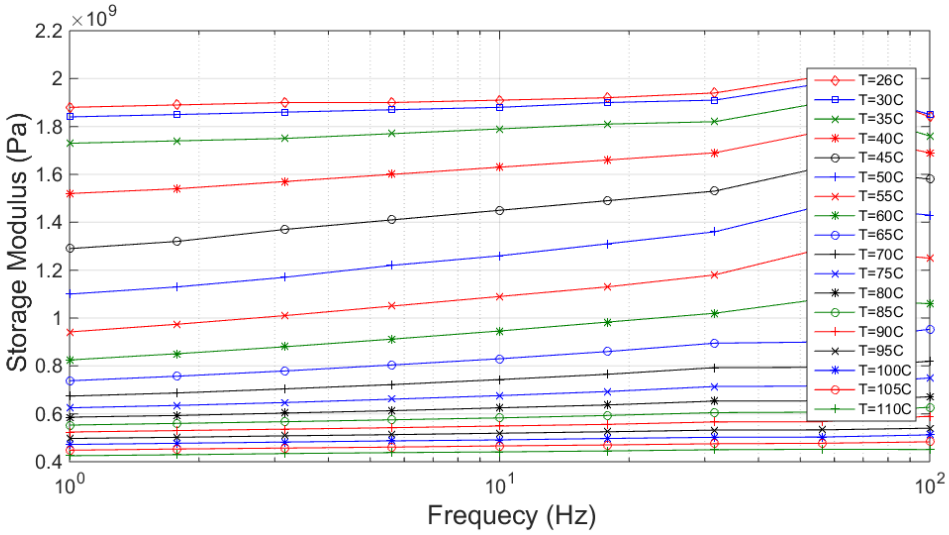

Figure 7-12- Modulus plots in different temperatures vs. frequency

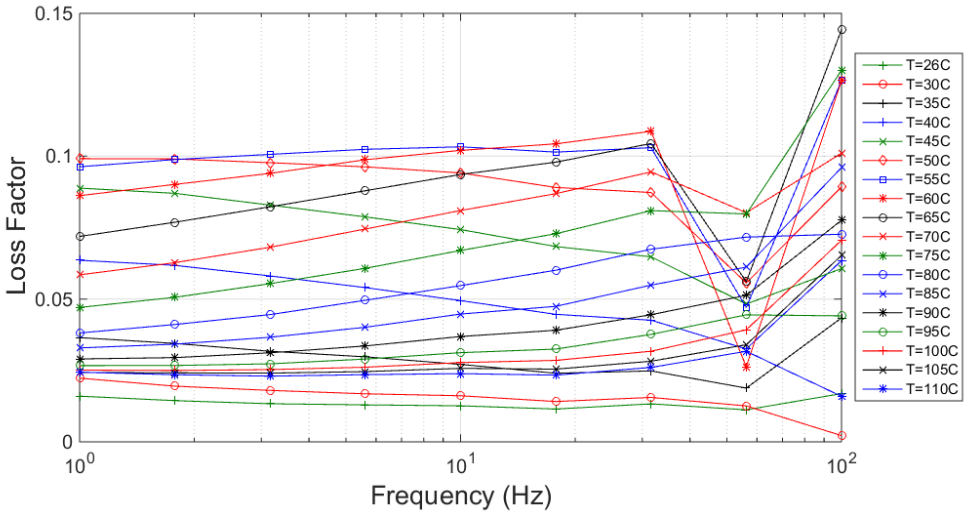

Figure 7-13- Loss factor plots in different temperatures vs. frequency

From the plots it can be observed that results obtained for frequencies above 40Hz appear to be inaccurate. The reason for this inaccuracy is most likely the presence of resonance in the measurement system. Each of these temperature plots was then shifted horizontally to coincide with the reference temperature graph (at temperature of 65°C), leading to the shift factor graph shown in Figure 7-14.

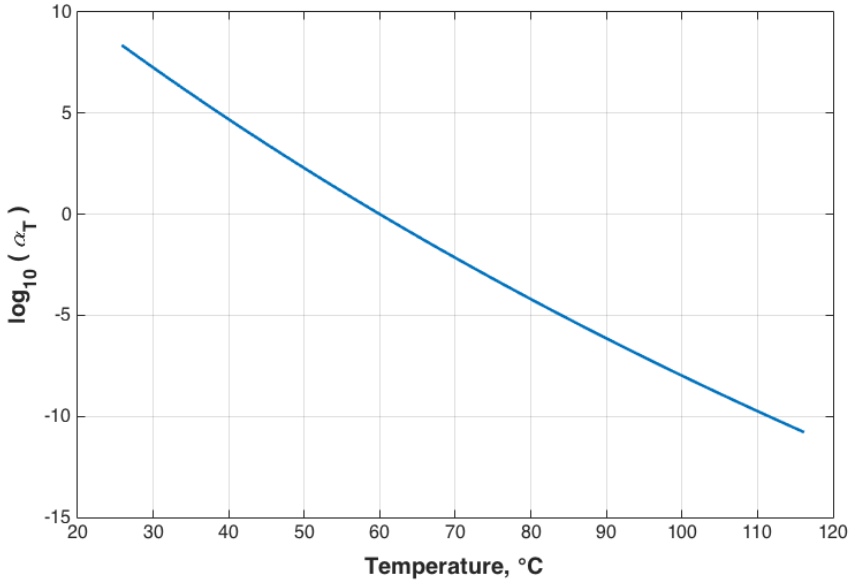

Figure 7-14- Temperature shift function versus temperature

The resulting plots also known as the master curves of the material can be observed in Figure 7-15 for reference temperature of 65ºC. This curve contains more information than any initial curve obtained at a single temperature.

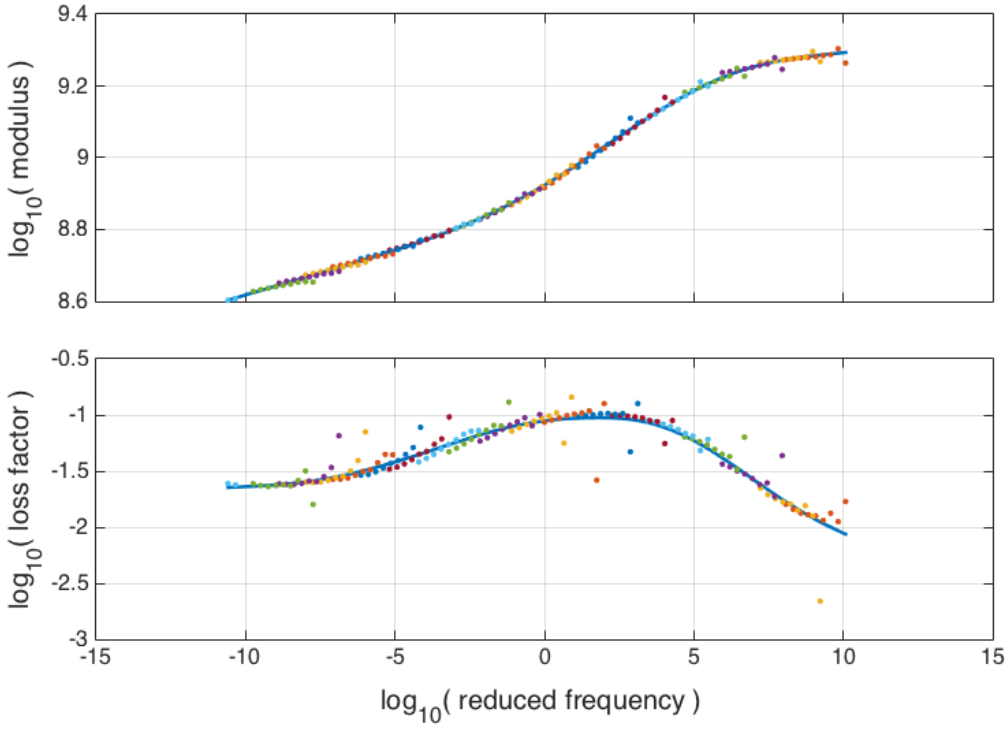

Figure 7-15- Master curves showing Young's modulus and loss factor, at reference temperature 65◦C

Prony series calculation and Prony parameters for a 20 prony terms are presented in Appendix A for future reference.

7-9-2- Tensile Tests

The stress-strain plots for parts with three different section thicknesses subject to tensile loading are shown in Figure 7-16. Stress is calculated based on nominal engineering stress which is the applied force divided by nominal cross-sectional area, and strain is equal to displacement of the sample divided by the total (from grip to grip) length of the sample experiencing displacement. These have been matched to maximum stress and strain results obtained from linear finite element analysis in ABAQUS for the same force levels on the sample.

As the stress-strain curves in Figure 7-6 suggest, an increase in ultimate tensile strength (UTS) can be observed with increase of section thickness.

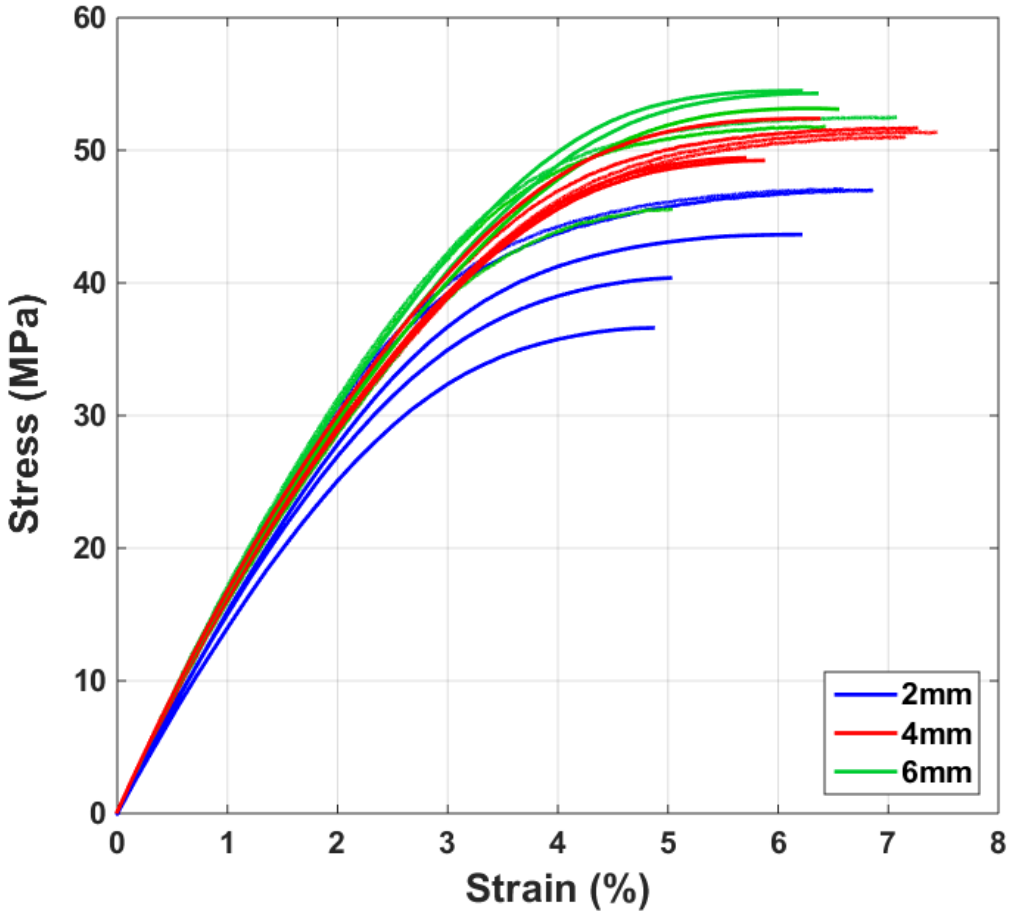

Figure 7-16 - Stress-strain plots of samples subjected to tensile tests

Figures 7-17, 7-18 and 7-19 show values of UTS, EaB and Young's modulus for the range of section thicknesses. Young's modulus values were calculated from the linear part of the graphs. All of the above-mentioned values show an overall increase with section thickness as opposed to results previously reported by Majewski et al [46] although the range of each set of results for each section thickness is similar. The difference between these two findings may be due to the different heating approaches of the build machines in each study. In the present study an EOS P100 machine was used in which room temperature powder is spread over the powder that has been heated up to its melting temperature by the laser. While in the study by Majewski et al the powder is preheated before being spread over the high

temperature powder. Therefore, higher heat transfer rate of sample surfaces and the thicker samples over the thinner ones in the present study might have led to a larger difference in degree of melting of samples with different section thicknesses and as a result larger difference between their mechanical properties.

In order to examine the statistical significance of the differences observed between the three groups of section thicknesses, non-parametric Kruskal-Wallis test was performed on the obtained values of UTS, EaB and Young's modulus in all the samples in SPSS. The results (presented in Appendix B) suggest that while the distribution of EaB data is the same across the three cross section groups (p=0.378), a statistically significant difference exists between the UTS (p=0.007) and Young's modulus (p=0.043) data in each group of section thickness.

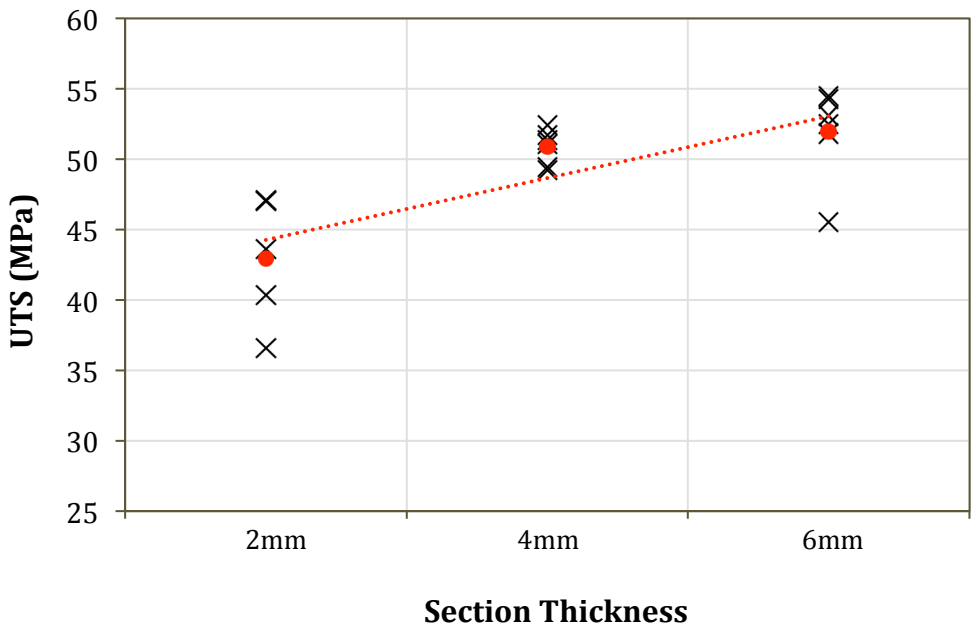

Figure 7-17 - Ultimate tensile stress vs. Section thickness

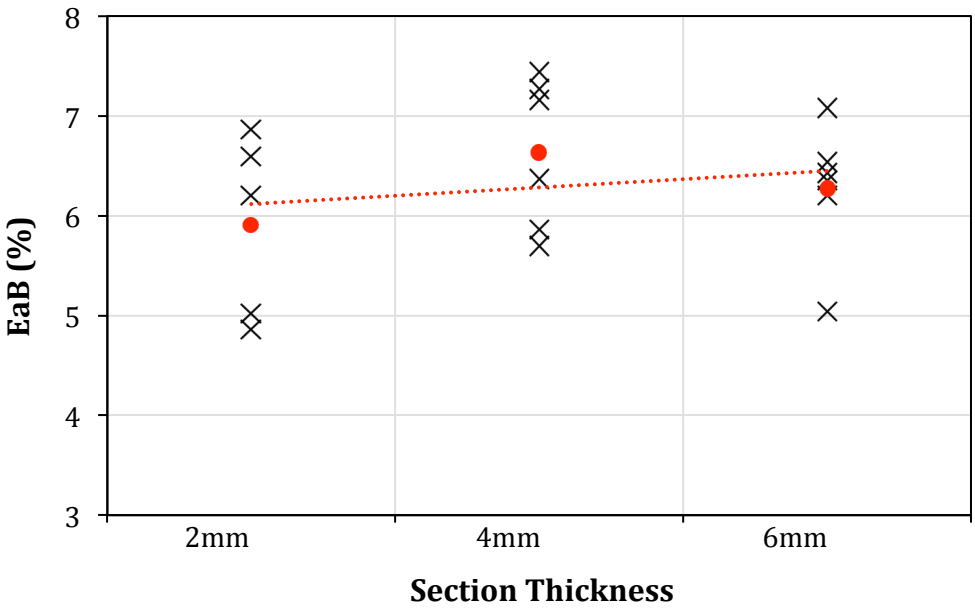

Figure 7-18- Elongation at break vs. Section thickness

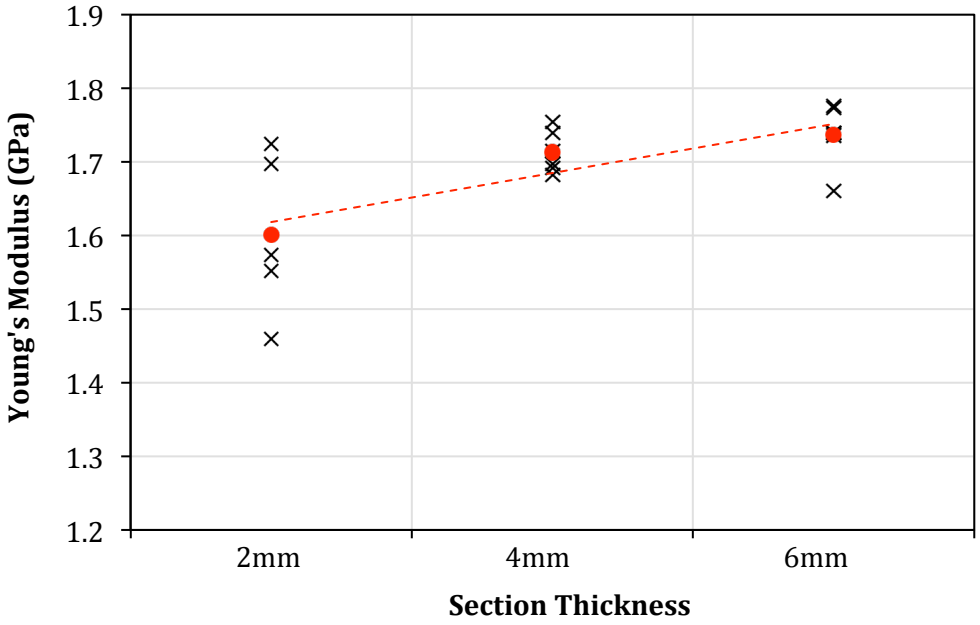

Figure 7-19- Young's Modulus vs. Section thickness

It may be that parts with larger section thicknesses have higher molecular weight, which leads to their better mechanical properties. The thermal load during the build process is presumed responsible for the increase in molecular weight and there is an argument that parts that are exposed to elevated temperature at a longer time have an increase in their molecular weight [37].

7-10- Summary

Understanding the behaviour of the material was the main objective of this chapter. To do so, a series of experiments were designed and conducted to establish the most important aspects of material characteristics. This included simple physical and geometrical identification as well as more advanced mechanical testing.

To obtain a better understanding of dynamic performance of the material, DMTA tests were performed to investigate the viscoelastic behaviour of the material and its changes with temperature and frequency. Master curves were produced to provide the viscoelastic parameters in a broader range of frequencies.

8. Effect of Section Thickness on Tension-Tension Fatigue Performance

8-1- Methodology

A new set of samples with the same dimensions and manufacturing parameters as described in sections 7-3 and 7-4 were manufactured and used for this set of experiments. Samples were subjected to tension-tension displacement-controlled cyclic loading and their performance was studied based on the load history required for the tests. Effect of section thickness of the samples on their fatigue life was studied for the highest suitable displacement level for cyclic testing. Stress relaxation tests were performed to compare the samples behaviour with their response under tension-tension cyclic loading.

8-2- Tension-Tension Cyclic Tests

The same experimental setup as used for the tensile tests, with addition of a thermocouple attached to the surface of the sample to measure its surface temperature, was employed for cyclic experiments. The test setup is shown in Figure 8-1.

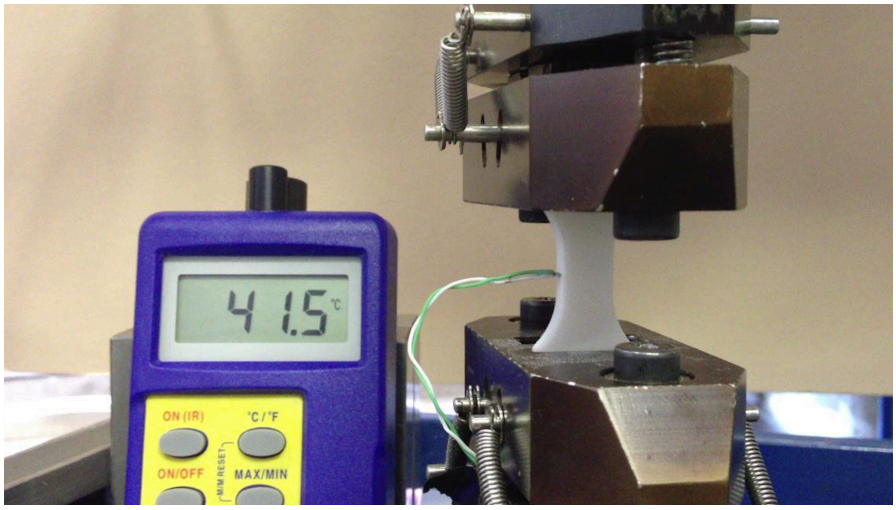

Figure 8-1- Tension-tension cyclic test setup

To produce the strain-fatigue life curve, 4mm samples as the middle range thickness were selected. Samples were fixed in the MTS machine with wedge grips. Tension-tension displacement-controlled cyclic loading was applied to the samples based on the instructions by ASTM D7791 standard test methods for uniaxial properties of plastics; the highest maximum peak for each section thickness was selected as 80% of the lowest EaB of the tensile test samples (1.8mm). Four other maximum displacement, as shown in Table 8-1, were also selected based on the same standard. In order to prevent compression in the samples, an amplitude of 0.4mm was selected, so that the minimum peak was above zero. Four samples were tested at the highest maximum displacement level and three samples were tested at each of the other displacement levels. Samples either broke or were removed from the machine after 24 hours (180000 cycles) if they did not break.

Table 8-1- Tension-tension cyclic test parameters for a 4mm sample

Maximum Displacement 1 (mm)	1.8
Maximum Displacement 2 (mm)	1.6
Maximum Displacement 3 (mm)	1.4
Maximum Displacement 4 (mm)	1.2
Maximum Displacement 5 (mm)	1
Frequency (Hz)	2
Temperature (°C)	26

The lower fixture of the machine, which contains the force sensor, was fixed. To avoid hysteresis heating, the upper fixture oscillated sinusoidally at a low frequency of 2 Hz, by the actuator. The required force and fatigue life of samples were recorded. A schematic of loading history for one cycle is illustrated in Figure 8-2. Tests were carried out at room temperature (25±2°C).

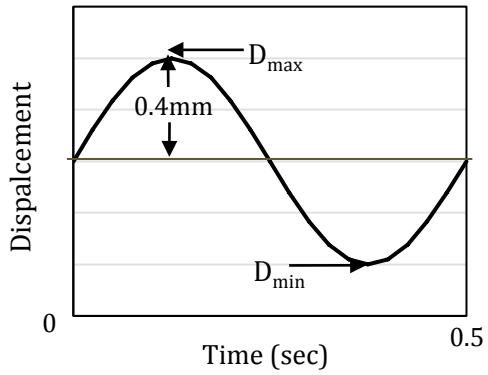

Figure 8-2- Schematic of loading history for a tension-tension cycle

8-3- Effect of Section Thickness

Six samples of each section thickness were selected to study the effect of section thickness of the samples on their fatigue performance. Samples were tested at the highest displacement level (1.8mm), with the same parameters and under the same conditions as described in Section 8-1-1. Fatigue life of the specimens was recorded.

8-4- Stress Relaxation

Stress relaxation tests were performed to compare the behaviour of the samples under stress relaxation with their cyclic response. Three samples with section thickness of 4mm were chosen for this set of tests and their stress against time plots were compared with the same plots of displacement-controlled cyclic tests.

According to the instructions from ASTM E328 for stress relaxation test methods, samples were fixed in the MTS machine as described in section 7-6-2. The starting displacement was chosen as the mean displacement in cyclic tests with the highest displacement peak; 1.4mm.

Samples were pulled to the starting displacement in 1 minute and were held at that position for 24 hours. The force required for holding the displacement was recorded. A schematic of the displacement history applied on the samples is shown in Figure 8-3.

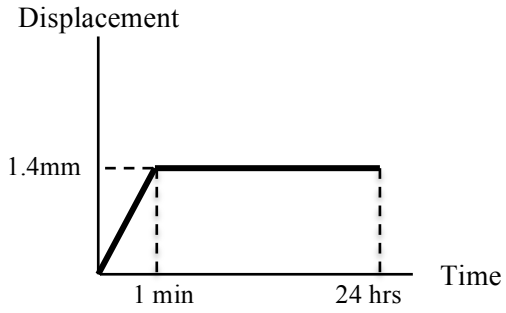

Figure 8-3- Schematic of stress relaxation displacement history

8-5- Results and Discussion

8-5-1- Tension-Tension Cyclic

Although the aim of these tests was to produce a strain-fatigue life curve, this could not be achieved as samples under the same displacement level experienced fatigue lives of up to 3 orders of magnitude different. Results from these experiments are presented in Table 8-2.

Table 8-2- Fatigue life of 4mm samples subject to displacement controlled tension-tension excitation

Number of Samples	Maximum Displacement (mm)	Fatigue Life of Each Sample (N)
4	1.8	>180000
		>180000
		1975
		833
3	1.6	>180000
		12562
		3486
3	1.4	>180000
		>180000
		46800
3	1.2	>180000
		5
		95420
3	1	>180000
		>180000

		133530

8-5-2- Section Thickness

Table 8-3 presents fatigue life of the 18 samples with three different section thicknesses tested at maximum displacement level of 1.8mm and displacement amplitude of 0.4mm. It can be observed from the results that the majority of samples, with exception of 3 samples, show high cycle fatigue performance.

Table 8-3- Fatigue life of samples with different section thicknesses subject to the same displacement level

Section Thickness (mm)	Cycles to Failure (N)
2	18
	13250
	11
	10136
	6558
	>180000
4	>180000
	>180000
	10850
	37956
	51
	>180000
6	31816
	2402
	127698
	>180000
	>180000
	>180000

In order to investigate the effect of section thickness of the samples on their fatigue life, number of cycles to failure of each sample was plotted against their section thickness for the examined displacement level as shown in Figure 8-4. In order to examine the statistical significance of the differences observed between the three groups of section thicknesses, non-parametric Kruskal-Wallis test was performed on the obtained values of fatigue life in all the samples in SPSS, considering the maximum life time of unbroken samples to be 180000. The

result (presented in Appendix B) suggests that the distribution of fatigue life data is the same across the three section thicknesses. In other words no stastical signifance exists between the fatigue lives of different section thicknesses.

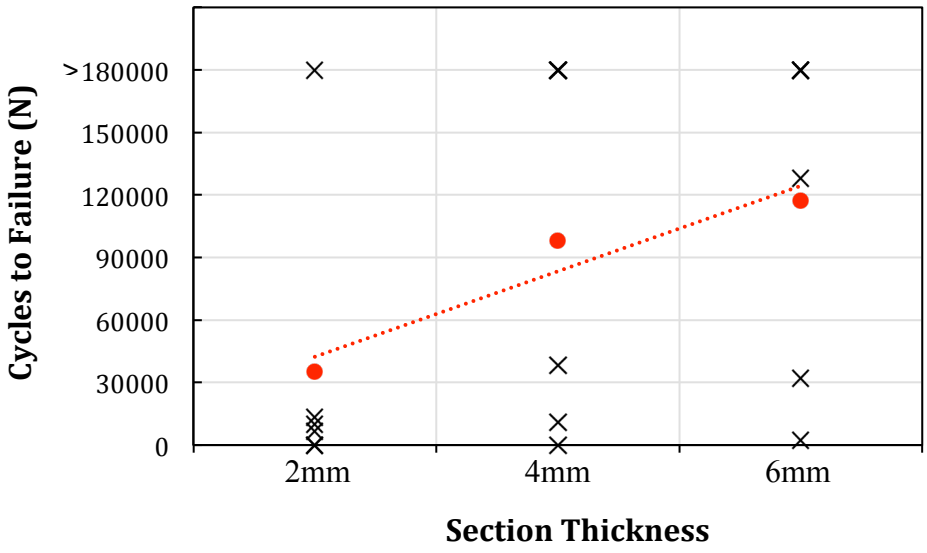

Figure 8-4- Fatigue life of samples with different section thicknesses under displacement-controlled tension-tension loading (max displacement=1.8mm, amplitude=0.4mm)

Applying the same test conditions to other specimens with the same size and built with the same machine parameters shows the variable behaviour of this material under tension-tension cyclic loading. This behaviour was observed in all displacement levels and all section thicknesses as shown in Tables 8-2 and 8-3.

Fatigue life of all three section thicknesses was plotted against their density and surface roughness in Figure 8-5 to investigate possible correlations. It should be noted that in order to find a trend line for the results, maximum fatigue life has been considered as 180000 cycles. As can be observed from the graphs, most of the R-squared values are smaller than 0.1, which confirms that fatigue life of 2mm and 4mm samples is independent of their densities and surface roughness and fatigue life of 6mm samples is independent of their surface roughness.

However, a good fit seems to exist between fatigue life of the 6mm samples and their densities. It can be presumed from the results that although fatigue life of samples with

different section thicknesses is not significantly different, its dependence leans more towards density as samples become thicker.

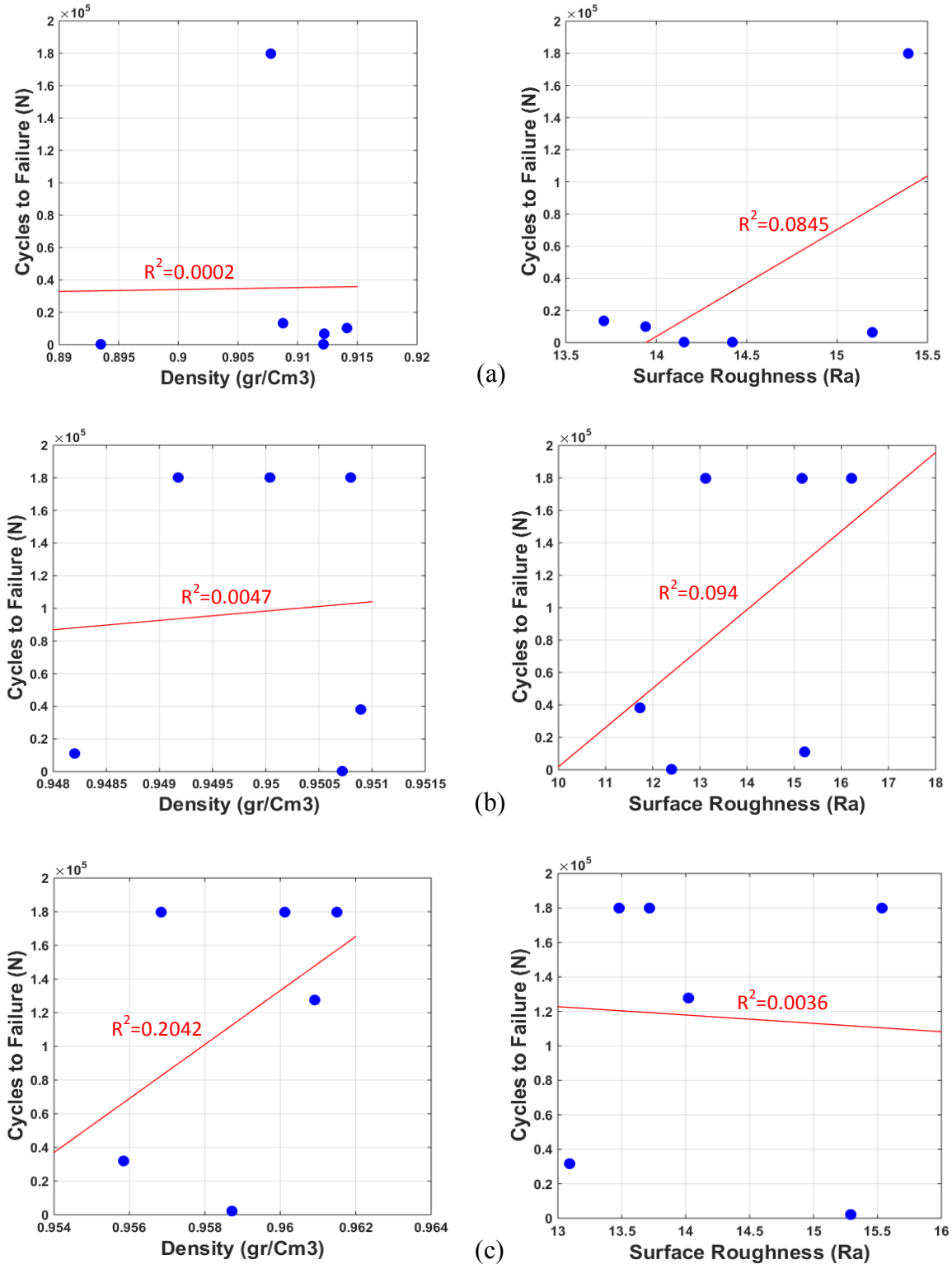

Figure 8-5- Density and surface roughness of a)2mm, b)4mm and c)6mm versus their fatigue life

To study the behaviour of the samples under tension-tension cyclic loading, their stress history including the evolution of the peak stress was plotted. Figure 8-5 illustrates the results for two samples with section thicknesses of 2 mm and 4 mm under the loading conditions described in section 8-1.

Although the minimum displacement was set to prevent compression, both samples experienced compression at some point during the test. While the recorded maximum and minimum values of stress decrease over time, the difference between maximum and minimum remained constant showing no sign of cyclic softening until the final stages of cycling prior to failure. This could be an indication of cyclic creep, suggesting that the samples appear not to have experienced fatigue until the final cycles.

It is thought that the samples experienced a small amount of creep in each cycle which did not recover in the subsequent cycles and caused a total increase in the specimen length and as a result a compression load on the specimen during latter stages of the test. No significant change in specimen temperature was observed during the tests.

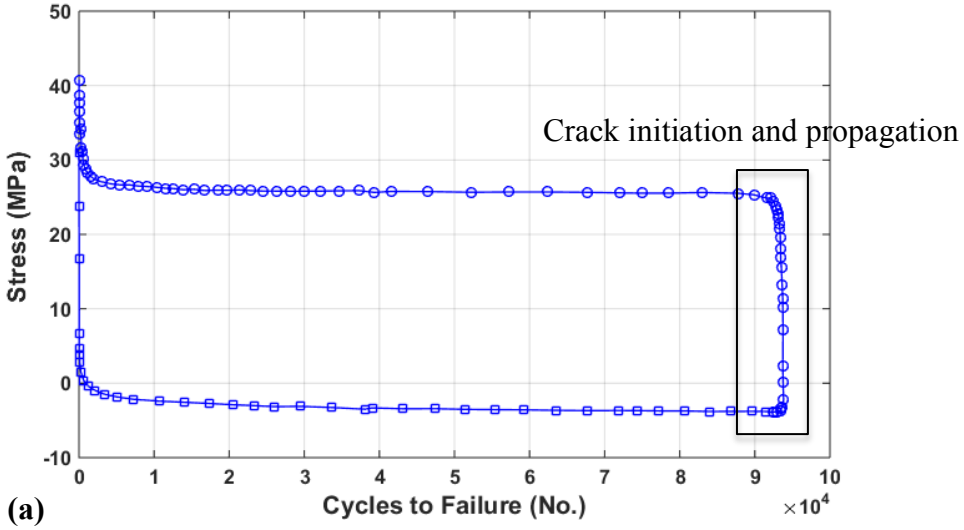

(a)

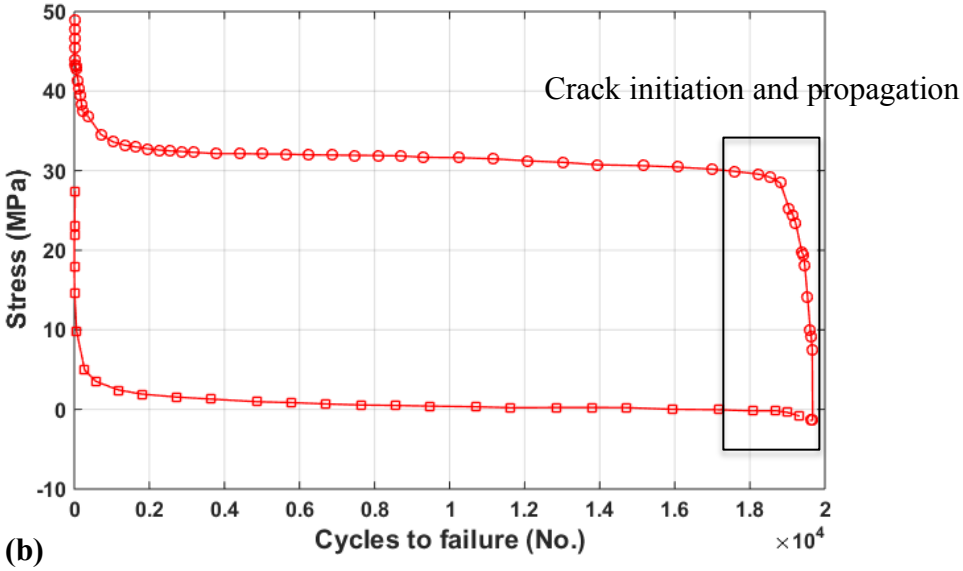

Figure 8-5- Stress vs. Number of Cycles to failure plots of a a)2mm and b)4mm sample (the top line in each graph shows the maximum and the bottom line shows the minimum stress points)

8-5-3- Stress Relaxation

In order to study the results in one figure, peak stress plots of two broken and two unbroken cyclically loaded samples, mean stress plots of the same samples and stress relaxation plots are shown in one graph in Figure 8-6.

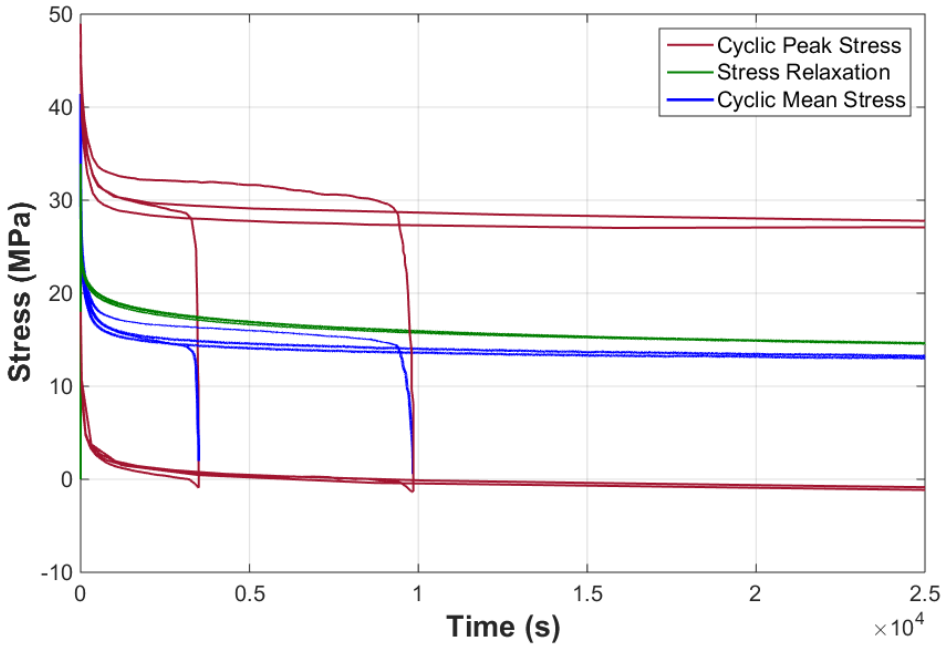

Figure 8-6- Stress vs. cycles to failure plots of 4mm samples under cyclic and stress relaxation tests

It can be observed that the cyclic peak stress and stress relaxation plots follow similar paths up to the crack initiation points, which can be more clearly observed in comparing the stress relaxation and cyclic mean stress plots. However, the amount of stress decay is clearly larger in cyclic samples. It is apparent that the samples exhibit a combination of creep and fatigue behaviour. This phenomenon also known as cyclic creep has been reported in previous works on tensile cyclic loading of epoxy polymers as well [73, 78].

8-5-4- Hysteresis

The initiation and subsequent evolution of fatigue damage in a specimen can be examined by inspecting the hysteresis curves at different number of cycles and loading conditions. Figure 8-9 shows the hysteresis behaviour of two 4mm specimens (sample 62 and sample 41) during their cyclic life time. One of the specimens has broken but the other one remained unbroken.

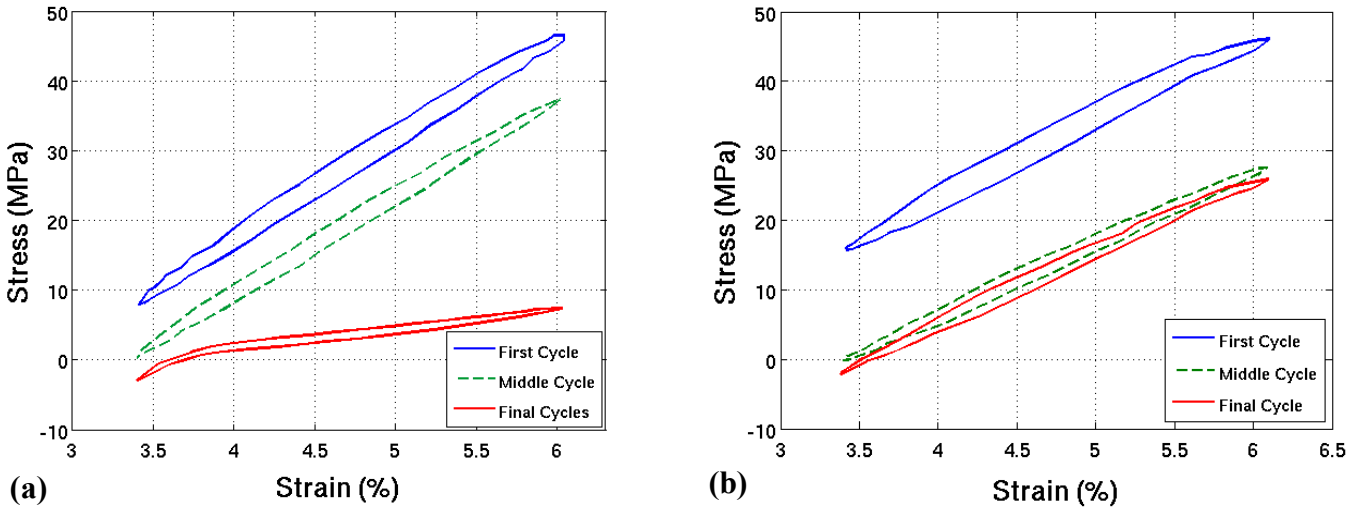

Figure 8-9- Hysteresis loops of 4mm specimens under the same test conditions (a) broken samples #68 (b) removed sample #41

In both cases, the stress level in the hysteresis loops drop up to a certain number of cycles, after which a change of slope is observed in the tension part of the hysteresis loop of the broken sample while the compression part of the loop remains unchanged. Looking closer at the final cycles on the failure plot in Figure 8-5; this change of slope is when the distance between minimum and maximum force peaks starts to decrease. This effect is consistent with previous observations and attributed to the production and growth of crazes after some

induction period and demonstrates brittle crack propagation in the sample [75]. This can be distinguished from Figure 8-9(b) where all the hysteresis loops have the same slope up to the point when the specimen has been removed.

The area inside the loops is indicative of the energy dissipated by the samples during the cyclic loading. This dissipated energy reduces from first cycle to the final one in both samples as illustrated in Figure 8-9(a), although the amount of decrease is visibly higher in the broken sample. Similar observation has been reported by Lesser [103] for IM Polyacetal samples under load controlled tensile cyclic tests and has been attributed to subcritical crack growth in the samples.

8-5-5- Fractography

Scanning Electron Microscopy was employed, in order to study the fracture surface of the broken samples. Samples were cut parallel to and 5mm below the fracture surface and were gold coated with an Edwards sputter coater S150B to make the sample conductive so that electrons would be able to pass through to enable employing of SEM. A Philips XL 20 SEM machine was used to study the fracture surfaces of the samples.

Micrographs of the fracture surfaces of a tensile test and a tension-tension cyclic test samples are provided in Figure 8-10. No sign of necking, which is a clear indication of ductile fracture or deformation in the loading direction, can be seen on fracture surfaces of the samples (A and B). Although a dimpled like area, which might be an indication of ductile failure, can be observed in a part of the micrographs of the tensile sample and in the fatigued sample (C and D), it can be concluded that both tests have resulted in a brittle fracture with the fracture surfaces perpendicular to the loading direction and dominated by normal stresses.

The voids visible in both samples (E and F) are due to the porous nature of the samples and are not signs of depressions due to plastic deformation. In the fatigued sample (G) a flow to the left can be observed in the fracture surface which is not the case for the tensile sample (H), this suggests that fracture has initiated at some point at the right side of the sample and been drawn to the left. Curled broken fibrils can be observed in Figures I and J due to crazing. Similar observations have been reported by Ho et al for laser sintered PC parts [45] in tensile test and Pruitt et al [104] for PC samples under tension fatigue.

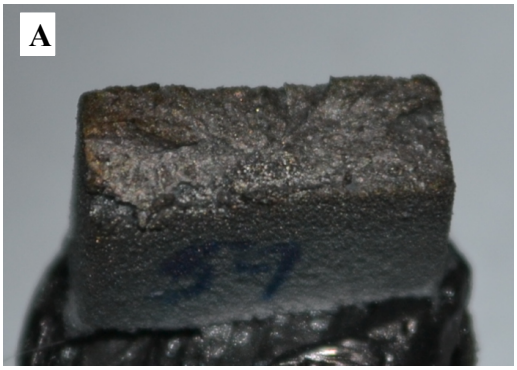
A

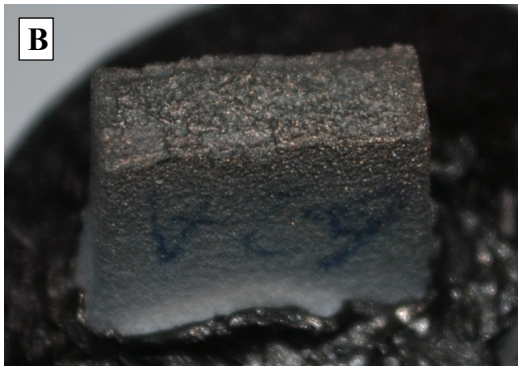
B

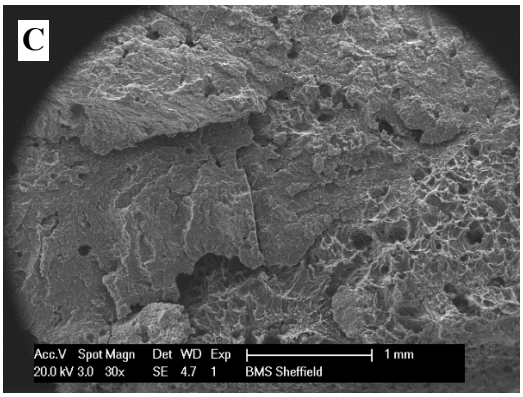
C
Acc.V Spot Magn Det WD Exp 1 mm
20.0 kV 3.0 30x SE 4.7 1 BMS Sheffield

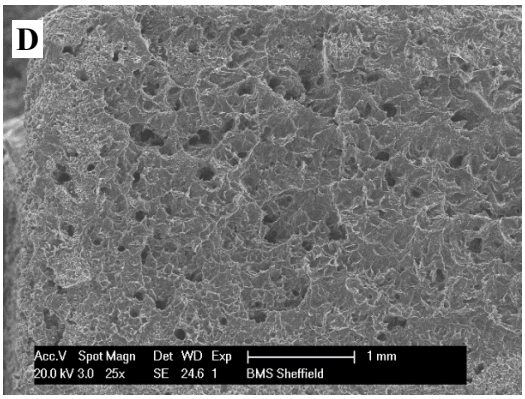
D
Acc.V Spot Magn Det WD Exp 1 mm
20.0 kV 3.0 25x SE 24.6 1 BMS Sheffield

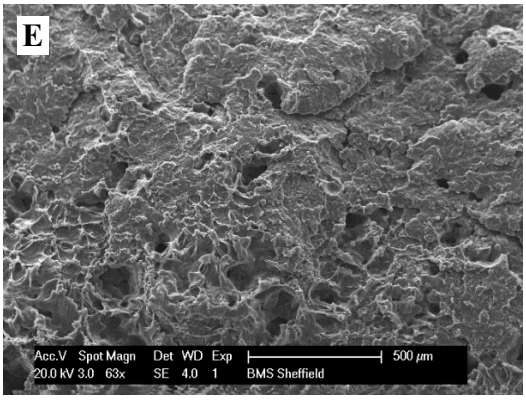
E
Acc.V Spot Magn Det WD Exp 500 µm
20.0 kV 3.0 63x SE 4.0 1 BMS Sheffield

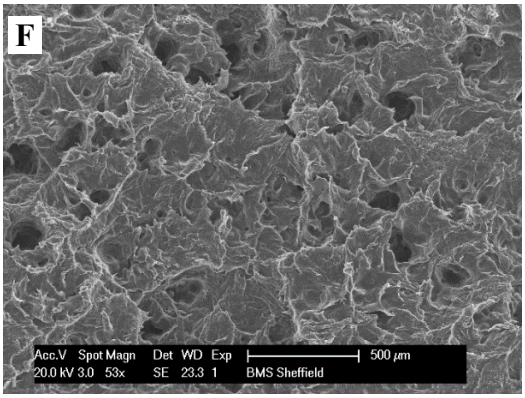
F
Acc.V Spot Magn Det WD Exp 500 µm
20.0 kV 3.0 53x SE 23.3 1 BMS Sheffield

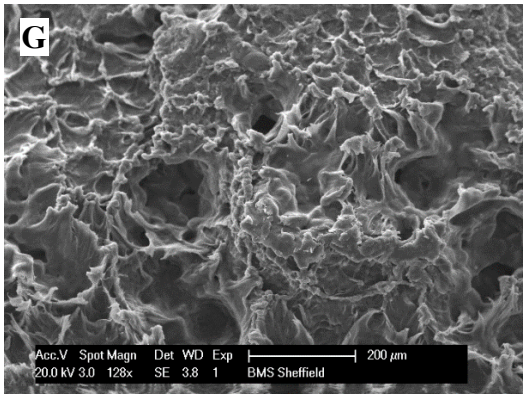
G
Acc.V Spot Magn Det WD Exp 200 µm
20.0 kV 3.0 128x SE 3.8 1 BMS Sheffield

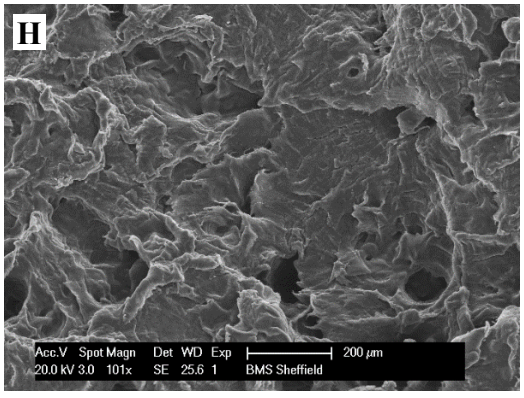
H
Acc.V Spot Magn Det WD Exp 200 µm
20.0 kV 3.0 101x SE 25.6 1 BMS Sheffield

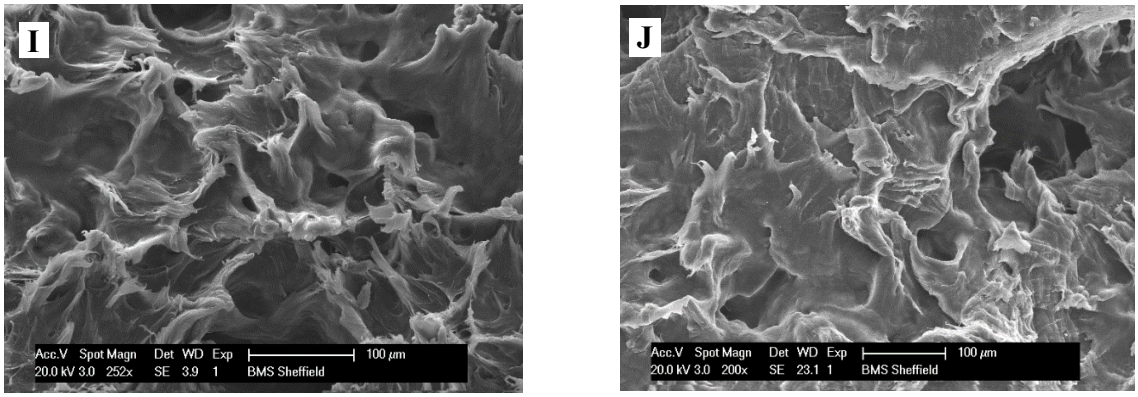

Figure 8-10- Micrographs of the fracture surface of specimens: tensile test (A, C, E, G,I); cyclic test (B, D, F, H,J)

8-6- Summary

Samples with three different section thicknesses were subjected to tension-tension cyclic loading to investigate their fatigue performance and the effect of their section thickness on this performance. Fatigue life of samples of all three section thicknesses appeared to not to be significantly different. However, fatigue life of samples was shown to be dependent on their their density in thicker samples.

Samples appeared to creep during the tension-tension test and experience compression, introducing creep and fatigue as two main causes of failure. Study of the hysteresis loops and fracture surfaces of the cyclic samples led to identifying crazing and brittle crack propagation.

9. Effect of Section Thickness on Tension-Compression Fatigue Performance

9-1- Methodology

A new set of samples with the same polymer powder, dimensions and manufacturing parameters as described in sections 7-3 and 7-4 were manufactured and used for this set of experiments. Samples were subjected to tension-compression force-controlled cyclic loading and their performance was studied based on the displacement history required for the tests. Effect of section thickness of the samples on their fatigue life was studied for two stress levels.

Force-controlled experiments were chosen due to the fact that samples experienced a small amount of creep in each cycle, which resulted in increasing of their length. In displacement-controlled loading ±D, during compression, samples were forced to the minimum displacement (-D) and the growth in length resulted in buckling of samples after a few cycles.

9-2- Tension-Compression Cyclic Tests

To apply tension-compression cyclic loading on the samples, samples were fixed in the MTS machine as described in Chapter 7. A force-controlled tension-compression cyclic load was applied to the samples at room temperature with a frequency of 2Hrz. The load was applied

first as a sine-tapered wave to prevent sudden loading and fracture of the samples, and progressed to a sine wave after four to five cycles. This Load was applied in the form of ±F, so zero mean stress was incurred ($R = \frac{F_{max}}{F_{min}} = -1$) and displacement of samples was recorded (schematic of loading history for one cycle is illustrated in Figure 9-1).

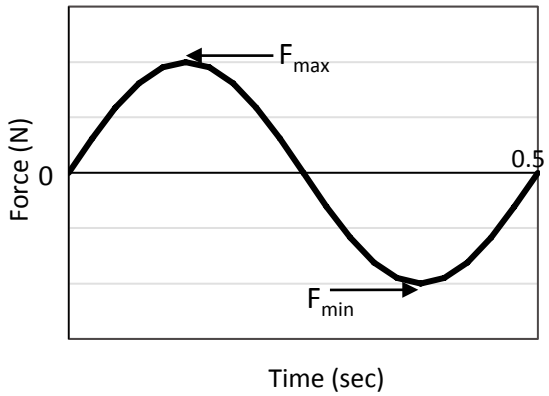

Figure 9-1- Schematic of loading history of a tension-compression cycle

In order to get an estimation of how samples responded to different load levels, the number of cycles they lasted before failure, and produce an S-N curve for the material, a number of 4mm samples, as the middle range of the samples produced, were subjected to load (stress) levels as shown in Table 9-1. Their number of cycles to failure were recorded and are shown in the same table.

Table 9-1 – Summary of loads and cycles to failure for 4mm tension-compression samples

Number of samples	Load (N)	Max Stress (MPa)
3	1200	30
3	1050	26
3	900	23
3	800	20
2	650	16

9-3- Effect of Section Thickness

Although buckling analysis of the test samples was based on the 2mm samples subject to the highest loading condition, these samples buckled under a much lower load in real testing

conditions. Therefore, only 4mm and 6mm samples were used for this set of experiments. Five samples of each section thickness were randomly selected and subjected to force-controlled tension-compression excitation at two stress levels of 20MPa and 30MPa to provide a reasonable time of failure. Experiments were conducted at room temperature and with a frequency of 2 Hz. Displacement and fatigue life of samples were recorded.

9-4- Results and Discussion

9-4-1- Tension-Compression Cyclic Tests

Table 9-2 presents fatigue life of the 4mm samples subjected to different stress levels of tension-compression loading.

Table 9-2- Fatigue life of 4mm samples subject to tension-compression cyclic loading

Number of Samples	Load (N)	Max Stress (MPa)	Number of Cycles to Failure	Average Fatigue Life
3	1200	30	236	247
			259	
			223	
3	1050	26	440	467
			524	
			428	
3	900	23	1026	953
			878	
			954	
3	800	20	2152	2252
			2353	
			2251	
2	650	16	$>10^6$	$>10^6$
			$>10^6$	

Results from the table are plotted as a stress vs. number of cycles to failure (S-N) curve and are shown Figure 9-2. As the graph indicates, Laser Sintered Nylon 12 parts built in the zx direction show a low cycle fatigue behaviour but do not fail under tension-compression cyclic loading (freq=2Hz) in less than one-million cycles with stress levels lower than 16MPa.

Results shown in this graph are consistent with the S-N curve in Van-Hooreweder et al studies [50], [51] and prove that the samples' geometry is suitable for tension-compression loading.

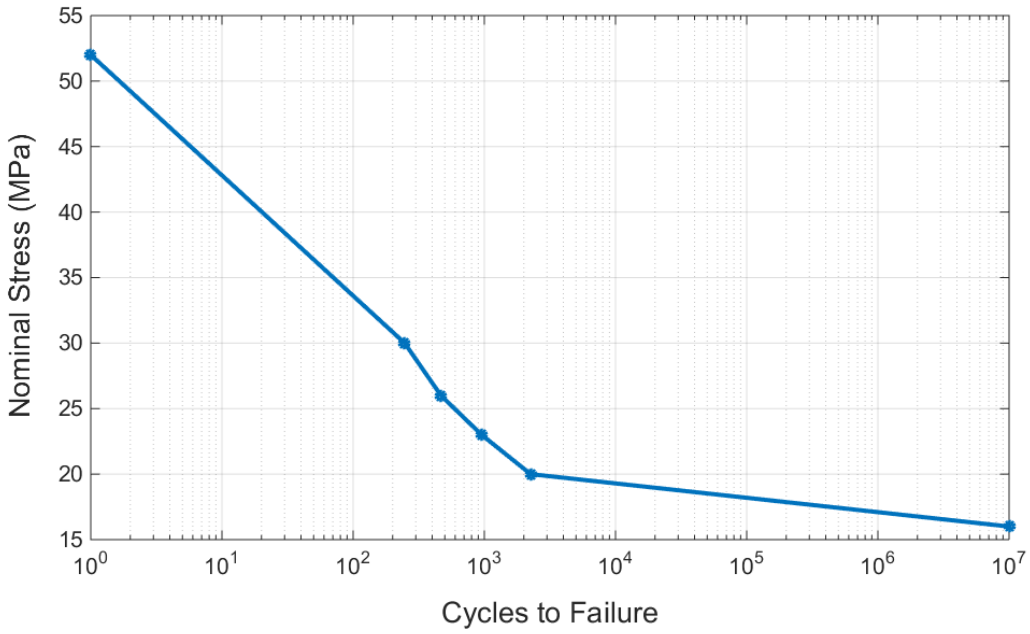

Figure 9-2 – S-N curve of LS Nylon 12 built in z direction (freq=2Hz, temp=ambient)

The evolution of the peak stress (stress history) of a sample subjected to tension-compression cyclic loading with load level of ±800N (±20MPa stress) is shown in Figure 9-3 as an example of the way samples behave under such loading conditions. As mentioned in section 9-1 samples experience a small amount of creep in each cycle (known as cyclic creep) which is evident in the difference between tension and compression displacements. Samples otherwise react to tension-compression loading as expected.

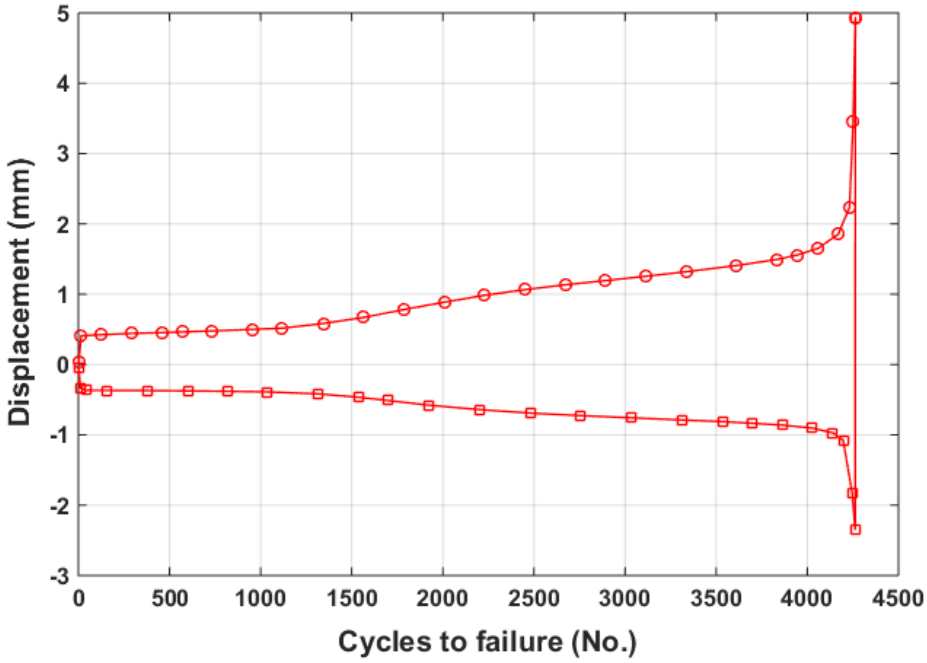

Figure 9-3- Peak stress vs. Number of Cycles to failure plots of a 4mm sample under tension-compression cyclic loading (top line shows the maximum and bottom line the minimum stress points)

9-4-2- Section Thickness

In order to investigate the effect of section thickness of the samples on their fatigue life, number of cycles to failure of each sample was plotted against their section thickness for the two examined stress levels as shown in Figures 9-4 and 9-5.

Results from the graphs imply that although the number of cycles to failure for most of the samples in the same stress level are in a similar range, number of cycles in the lower stress level (20MPa) tend to decrease for thicker samples, while a slight increase is noticeable in the higher stress level (30MPa).

The smaller fatigue life of thicker samples could be attributed to the fact that these samples generate more energy than the thinner ones, which results in their faster temperature increase, hence a more rapid thermo-mechanical failure, this theory is however contradicted in the higher stress level.

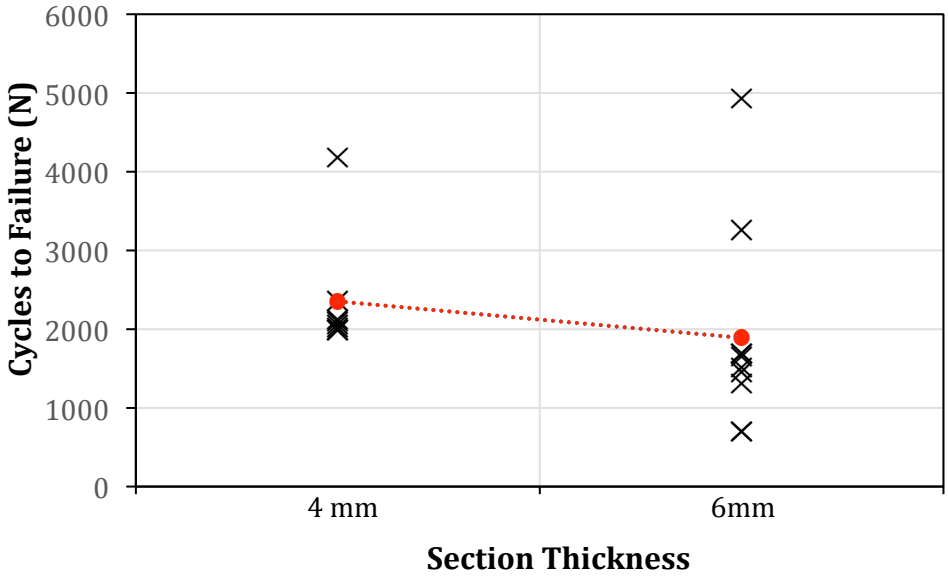

Figure 9-4 - Number of cycles vs. section thickness for stress level of 20 MPa

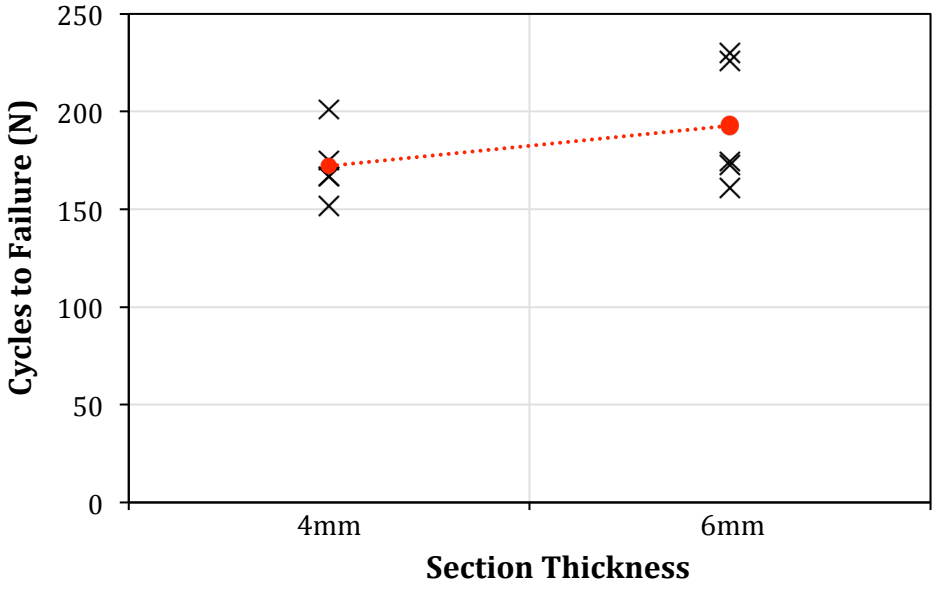

Figure 9-5 - Number of cycles vs. section thickness for stress level of 30 MPa

Statistical analysis was performed on the results from both stress levels to evaluate the significance in the difference between the results for each stress level. The Mann-Whitney U

test was chosen, as the statistical sample size was small and samples were not identically distributed.

The results from the Mann-Whitney U (Appendix B) test revealed a statically significant difference between the fatigue life of samples with section thickness of 4mm and samples with section thickness of 6mm tested with 20MPa maximum stress level (U=15, p=0.026). However, no significant difference was observed between the fatigue life of samples of the two section thickness group tested with 30MPa maximum stress (U=8, p=0.346)

9-4-3- Hysteresis

As explained in Chapter 7, inspecting the hysteresis loops of a sample subject to cyclic loading helps with identification of initiation and evolution of thermo-mechanical fatigue damage within the sample. Figures 9-6a and 9-6c show hysteresis loops of 4mm samples under maximum stress levels of 20MPa and 30MPa respectively. Hysteresis loops of 6mm samples subject to the same stress levels are shown in Figures 9-6b and 9-6d. Loops presented in Figure 9-8 only show the first, middle and final cycles of each sample. First cycle is the cycle after the sine-tapered period where the cyclic load grows to its peak values, and final cycle is the cycle where load levels drop and failure begins.

It can be observed that although both samples have similar amounts of dissipated energy in the first cycle, the difference in these values increases with the number of cycles. The thicker sample shows a visibly larger amount of dissipated energy towards the final cycles. This difference is more noticeable in the lower stress level.

Comparing the hysteresis loops from different stress levels with the same section thickness, the area under the loops is larger in higher stress level during testing. This indicates that at higher stress levels more energy is dissipated from the samples.

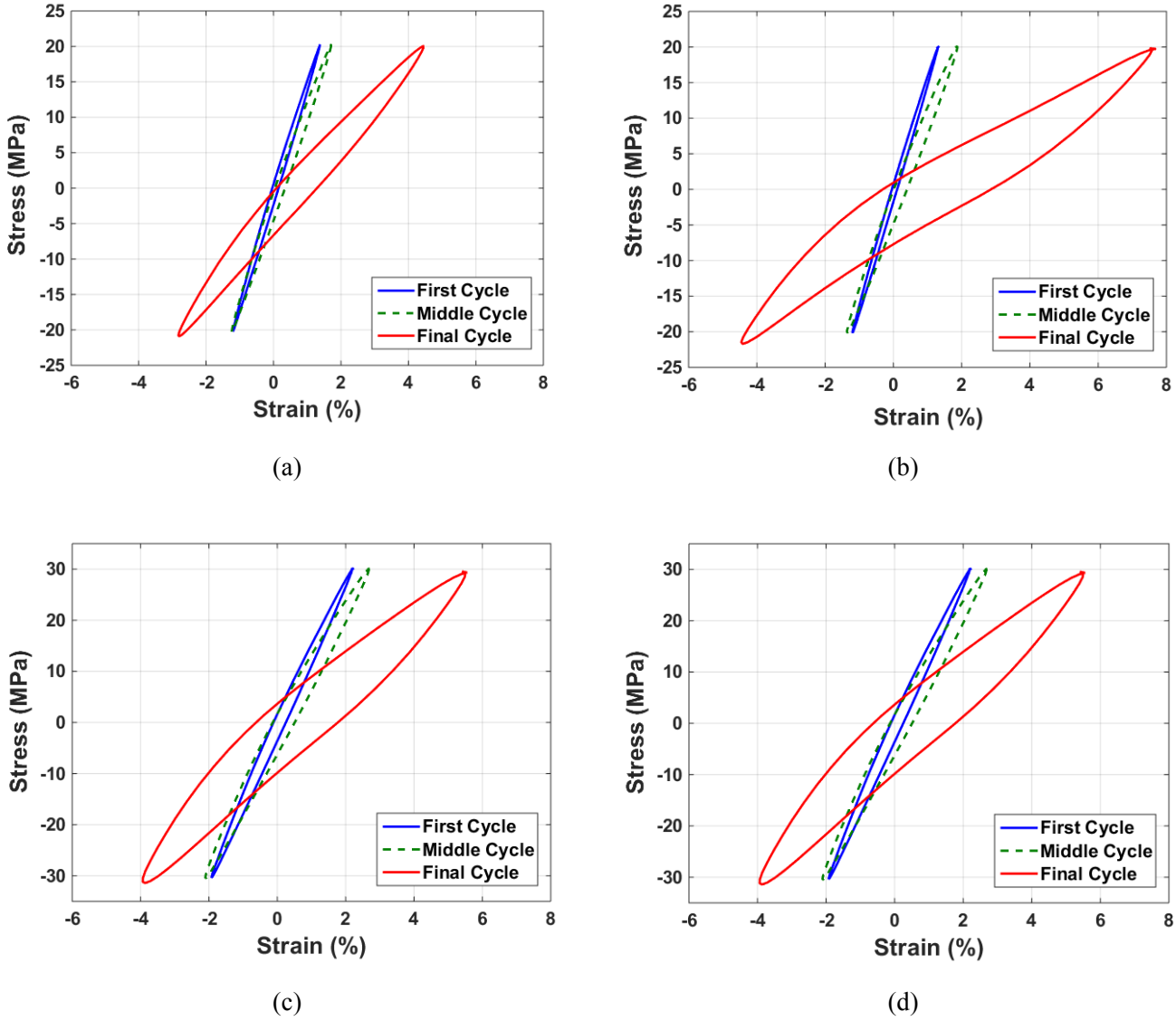

Figure 9-6- Hysteresis loops for 4mm and 6mm samples subject to 20MPa (a and b) and 30MPa (c and d) stress levels respectively

Apart from dissipated energy, the slope of the hysteresis loops shows the stiffness of the material in each cycle. It is clearly visible that the slope of the hysteresis loops in both section thicknesses and both stress levels decreases as the number of cycles increase, showing that the material is changing to a less stiff state. This can be associated with the fact that the dissipated energy causes the sample to heat up. As the temperature of the material increases to its glass transition region and possibly past that, the amorphous polymer chains soften, leading to lower stiffness and larger deformations at the same stress level [105].

The origins of the loops shifts to the right as the number of cycles increases, indicating a continuous increase of strain and proving the presence of a small amount of cyclic creep even when the mean stress is zero.

9-4-4- Fracture Surface

Fracture surface of the broken samples were studied using SEM to get an understanding of their cause of failure. Micrographs of a 4mm and a 6mm sample, both subjected to 20MPa tension-compression stress level are shown in Figure 9-7.

It is clear from fracture surfaces of the samples (A and B) under tension-compression cyclic loading that samples have experienced a ductile fracture dominated by shear stresses. Signs of plastic deformation and necking can be observed in images C and D. Another noticeable fact in these images is that a semi-dome-shaped dent is formed in the centre of the broken cross section. This feature can be observed on both ends of the fracture surface. This may be due to the temperature difference and as a result a difference in the plastic flow between the centre of the sample and its surface, as a result of different amount of heat transfer hence temperature. Similar feature exists in micrographs from Van Hooreweder et al work [50] but has not been acknowledged by the authors.

As temperature of the sample increases and passes T_g, amorphous chain segments begin to translate and rotate causing a plastic flow. Semi-spherical depressions on the surface (E and F), which are larger than an average powder particle, are indications of this plastic flow within the sample. The striations visible in images G and H are indicative of fatigue damage in the samples [68].

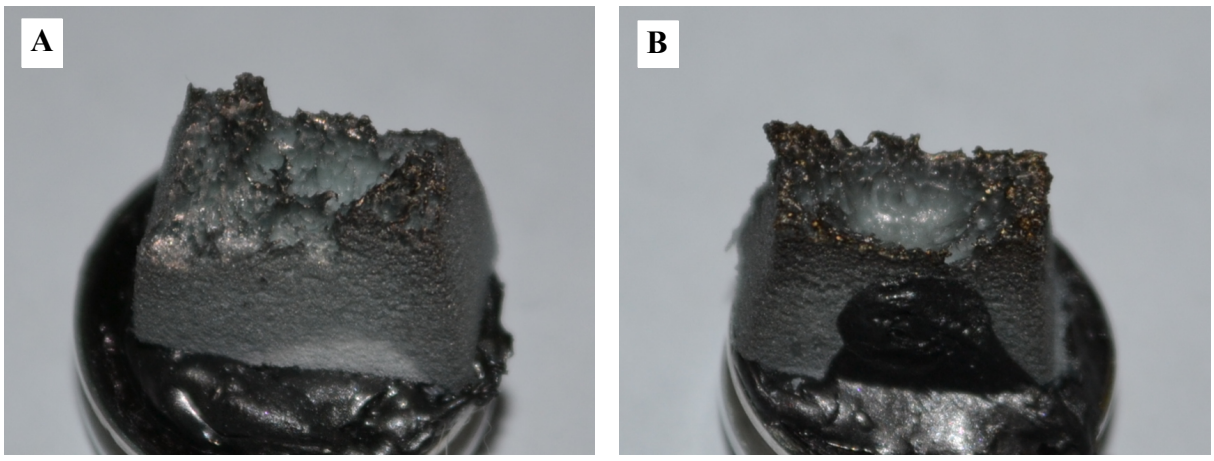

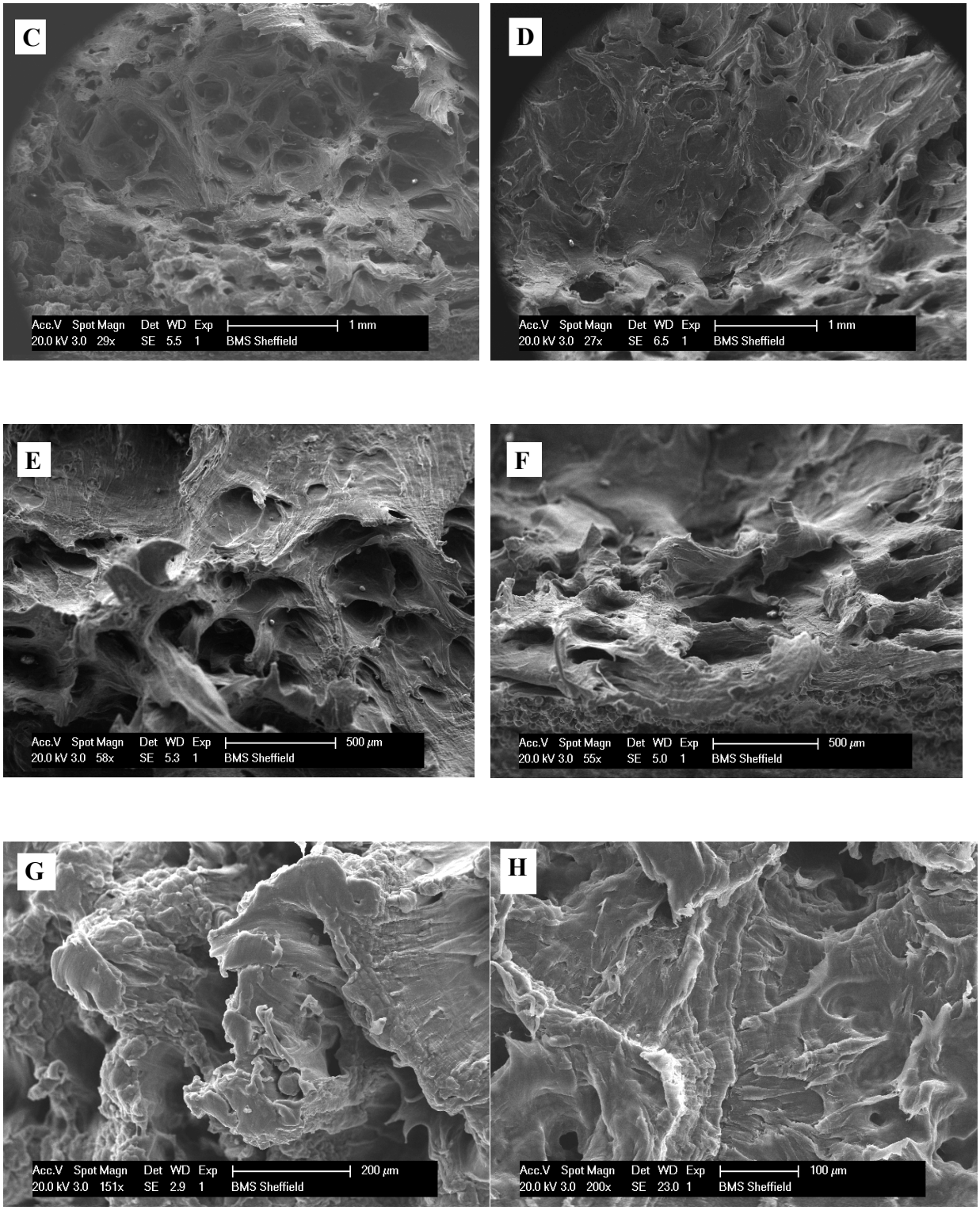

Figure 9-7- Micrographs of fracture surfaces of A,C,E) 4mm and B,D,F) 6mm samples under tension-compression cyclic loading with 20MPa stress

9-5- Summary

Investigation of the cyclic behaviour of parts continued in this chapter by implementing tension-compression force-controlled experiments. Number of cycles to failure plots and Hysteresis loops were presented and studied to investigate the effect of section thickness on tension-compression fatigue performance. It was observed that thicker samples dissipated a larger amount of energy in both maximum stress levels. Fatigue life of samples could not be associated with this finding as plots of number of cycles to failure for different stress levels did not show a consistent influence of section thickness on fatigue life of samples.

10. Effect of Porosity

10-1- Methodology

In order to get a better understanding of the internal morphology of the samples and its influence on their performance, 45 samples, 15 of each cross section, from the same batch as used in Chapter 9 were micro-CT scanned prior to testing. 3D morphological images of the samples were constructed and pore size distribution and porosity within each sample and among samples were studied and compared.

4mm and 6mm Samples were subjected to tension-compression fluctuating loads and their cycles to failure were recorded, which were later used to relate to porosity of the samples.

10-2- Micro-CT

Micro-CT has great advantages when it comes to studying the specimen morphology due to its ability to provide precise quantitative and qualitative information on the 3D morphology of the specimen. The interior of the specimen can be studied in great detail without resorting to physical sectioning nor using toxic chemicals. Moreover, after scanning, the intact samples can be subjected to other tests, allowing comparison of CT data with results from other tests.

10-2-1- Scanner Settings

A Skyscan 1172 scanner was employed for micro-CT scanning of the samples. Samples were glued to the surface of a rotating platform and mounted on to the scanner. Samples were scanned with scan parameters shown in Table 10-1. Three scan fields were defined so the total volume of samples between the grips was scanned. Approximately 700 scan slices were taken and files were reconstructed.

Table 10-1- micro-CT scanning parameters

Current (µA)	167
Voltage (kV)	60
Pixel Size (µm)	13
Layer Thickness (µm)	13
Rotation step (°)	0.7
Scan Rotation (°)	180

10-2-2- Image Reconstruction

The SkyScan NRecon package was used to reconstruct cross-section images from tomography projection images. It was important that all sample files were reconstructed with the same settings to make their morphology results comparable. For the current samples, a dynamic image range of 0-0.05 was chosen. It was also important to reduce the number of scan artifacts by setting the right ring artifact reduction and beam-hardening correction values to prevent obscuring of the CT results. Ring artifact reduction was set to 10 and beam-hardening correction was set to 60% in this set of scans.

10-2-3- CT Analyser settings and Thresholding

CT-Analyser (CTAn) is an application for measuring quantitative parameters and constructing visual models from scanned 3D datasets obtained with SkyScan micro-CT instruments. Architectural characteristics of the samples including porosity, average pore size and pore size distribution were measured and compared between samples using this application; a constant value of thresholding was applied to all of the samples. This was important due to the fact that CTAn uses binary images to calculate these characteristics.

10-3- Tension-Compression Cyclic Tests

In order to investigate the influence of porosity on fatigue behaviour of parts in tension-compression cyclic loading, tension-compression cyclic tests were conducted on five samples from each of the 4mm and 6mm section thicknesses, which had already been µCT-scanned. Experiments were performed at two stress levels of 20MPa and 30MPa, at room temperature and with a frequency of 2Hz.

10-4- Results and Discussion

10-4-1- Micro-CT

Grayscale and coloured 2D micro-CTimages were produced using CTAn software. In the grayscale images regions of different densities vary from black to white, black being the lowest density. The coloured images show regions of different densities in different colours (lowest density is presented in black and highest density is white).

2D images have been selected from the same layer in the centre of parts, layer #1400 (in the CT images) as shown in Figure 10-1 using the layer numbers presented in CT-analyser, so that cross-sections of the same depth within the samples can be compared.

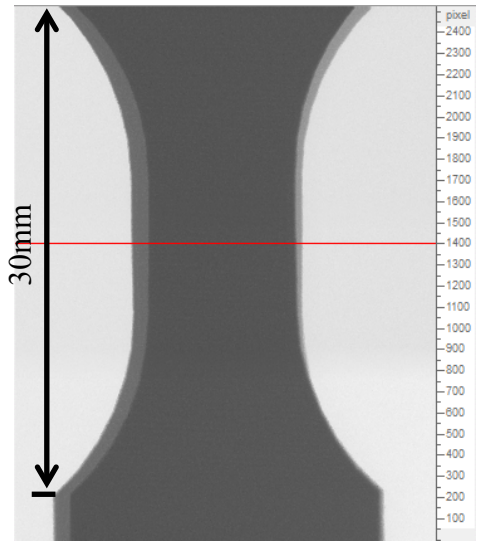

Figure 10-1- presentation of layer selection

Figure 10-2 shows greyscale and coloured images of the 2D layer described for three samples of three section thicknesses as examples. The areas in black show the presence of pores in the structures, and as visually observed, there are a larger number of pores with larger diameters in thicker samples. While a smaller number of pores seems to be present around the edges which is comparable to the results reported by Rusenburg et al [106], the coloured images show lower densities (pink and orange) in comparison with the inner area of all the samples. This contradicts the results reported by Rouholamin et al [107] which might be due to different approaches to sample preparation; Rouholamin et al cut circular samples from larger LS parts, whereas in this work the complete cross-section has been CT-scanned.

No significant difference in densities is visible between the three section thicknesses, although the thicker part seems to possess a larger area with brighter colours (lower density) than the other two parts.

Looking closer at the 2D images throughout the height of each sample, no noticeable defect seems to exist in any of the samples. Therefore, the idea that internal defects might be the reason for samples showing different behaviour under identical loading conditions appears not to be valid in this case.

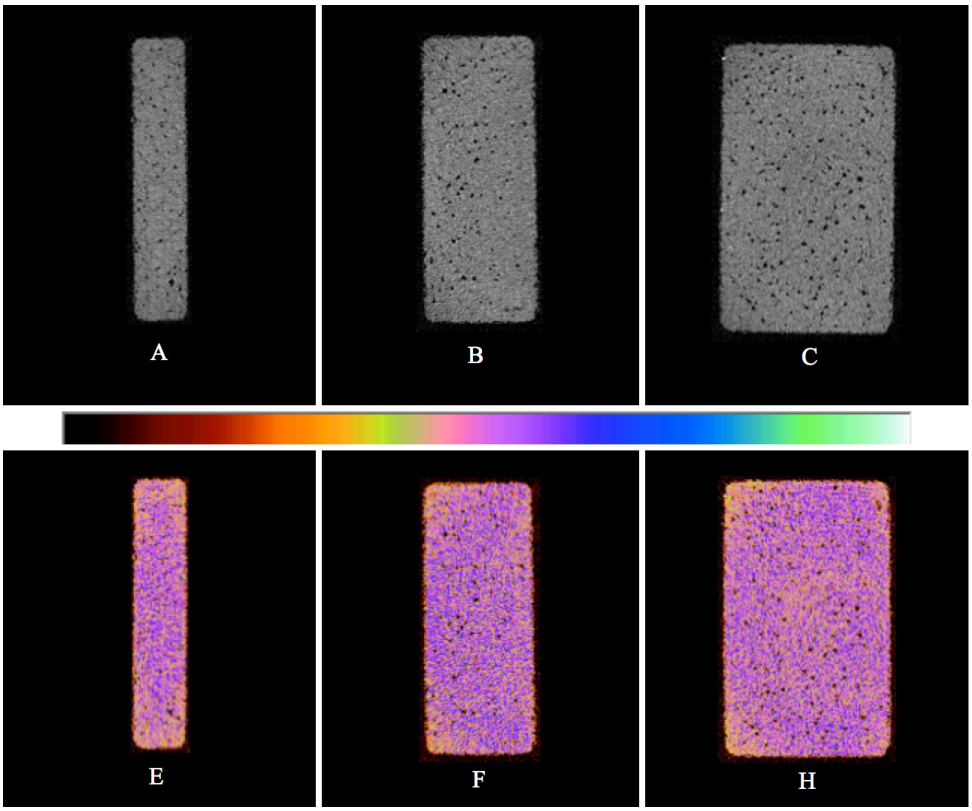

Figure 10-2- 2D Micro-CT images of cross sections of A,E) 2mm, B,F)4mm and C,H) 6mm parts generated in CT-analyser

As mentioned earlier, black areas within the samples indicate the presence of pores. Presence of pores and their distribution can be assumed an influential factor in mechanical properties of LS parts, but have never been studied.

Porosity and average pore diameter was measured for fifteen samples of each section thickness (45 samples in total) from the micro-CT images, using CT-analyser. Figure 10-3 shows the porosity range for each section thickness.

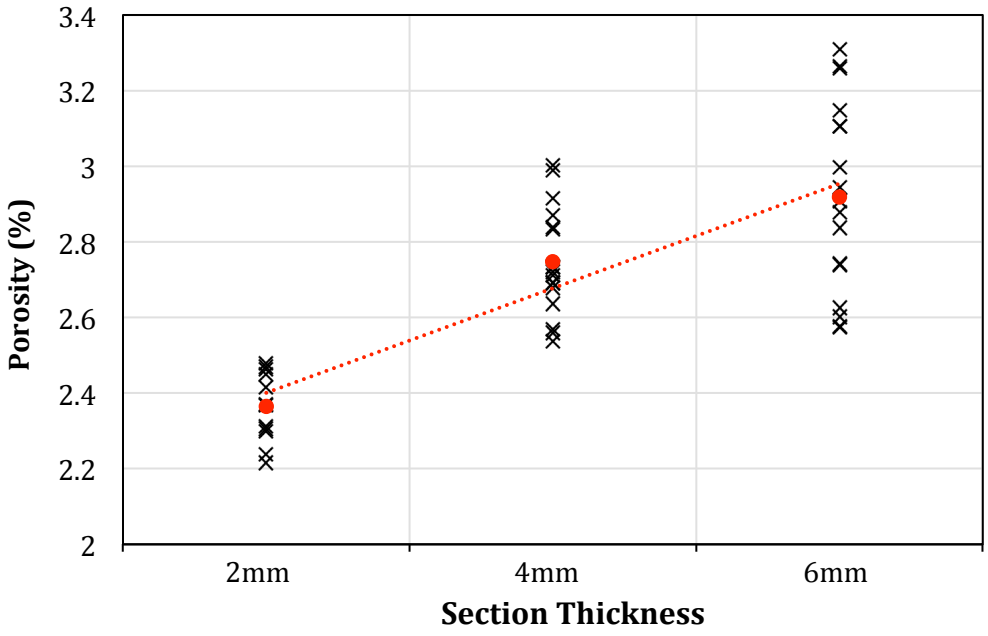

Figure 10-3- Porosity range for samples with 3 different section thicknesses

Although some overlaps can be observed, the trend in Figure 10-3 shows that porosity increases with section thickness. The range of porosity in this study (2%-4%) is comparable, but a little lower than the ranges reported by Rouholamin et al (4%-5%) and Rusenberg et al (3%-7%) which suggests that the LS machine was well toned in terms of process parameters.

The pore diameter range within each sample was also measured for the samples and is shown in Figure 10-4 for all section thicknesses. It can be observed from the figure that while 2mm parts have a larger number of pores with smaller diameters, the percentage of pores decreases in these parts as the pore diameter increases. In the thickest samples on the contrary, although the percentage of pores decreases as the pore diameter increases, the percentage of larger pore diameters is higher in these samples than the thinner samples. This can be attributed to

formation of gas from polymer degradation due to the longer period of time thicker samples stay at elevated temperature.

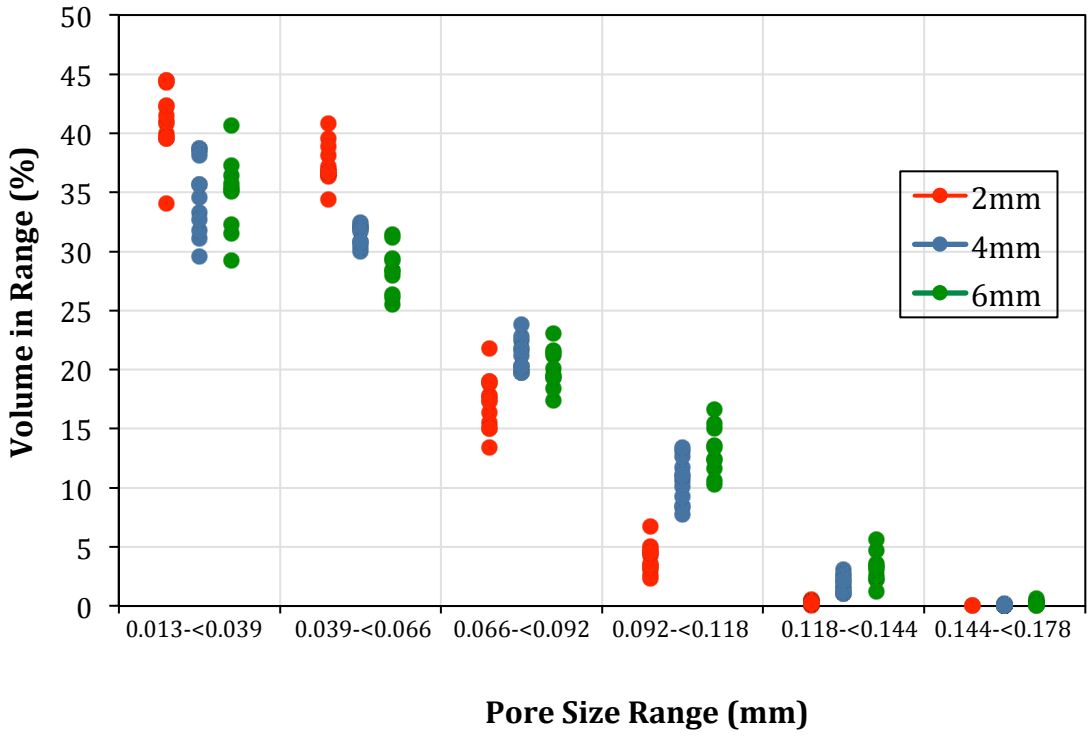

Figure 10-4- Percentage of pore diameters in the three section thicknesses

10-4-2- Effect of Porosity on Cyclic Performance

The number of cycles to failure of each sample was plotted against their porosity to study any existing relationship between them. Looking at the data points in Figures 10-5 and 10-6, no correlation can be observed between the number of cycles to failure and porosity of the samples at any of the thicknesses and stress levels. This can be further confirmed by plotting linear trend lines and generating R^2 (coefficient of determination) values. R^2 values closer to 1 show good fit of the data points to the regression line and are indications of possible correlations between the examined parameters. The graphs and R^2 values show that despite the common belief that mechanical properties highly depend on porosity, tension-compression fatigue life of laser sintered Nylon 12 parts appear not have a relationship with their porosity. This also confirms the results obtained in Chapter 7, showing density has no influence on fatigue life of samples under tension-tension cyclic loading within the ranges studied in this research, that were generated using standard build protocols.

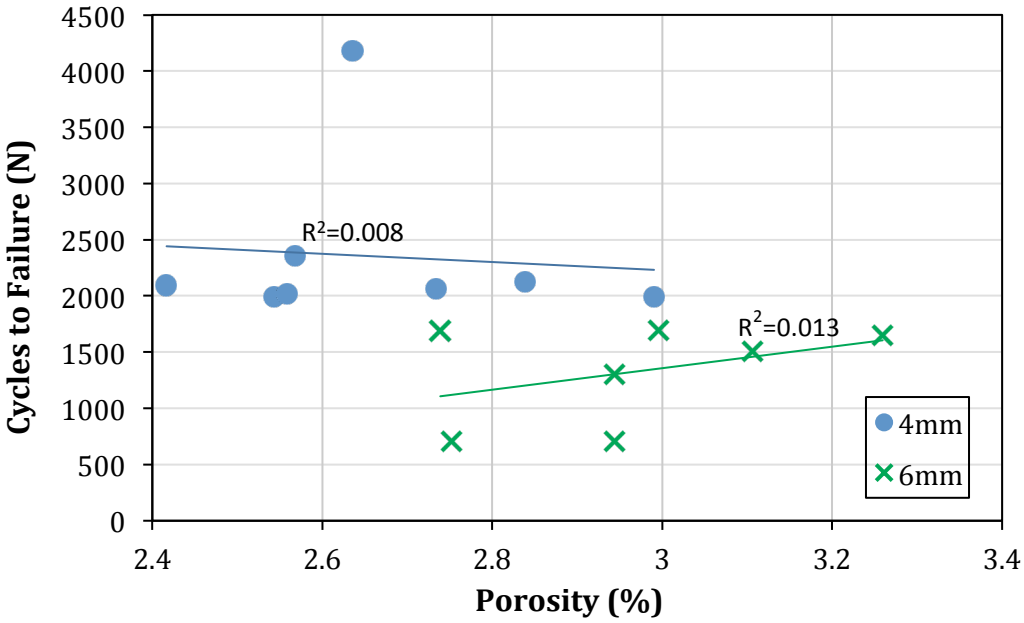

Figure 10-5- Number of cycles to failure vs. porosity for stress level of 20MPa

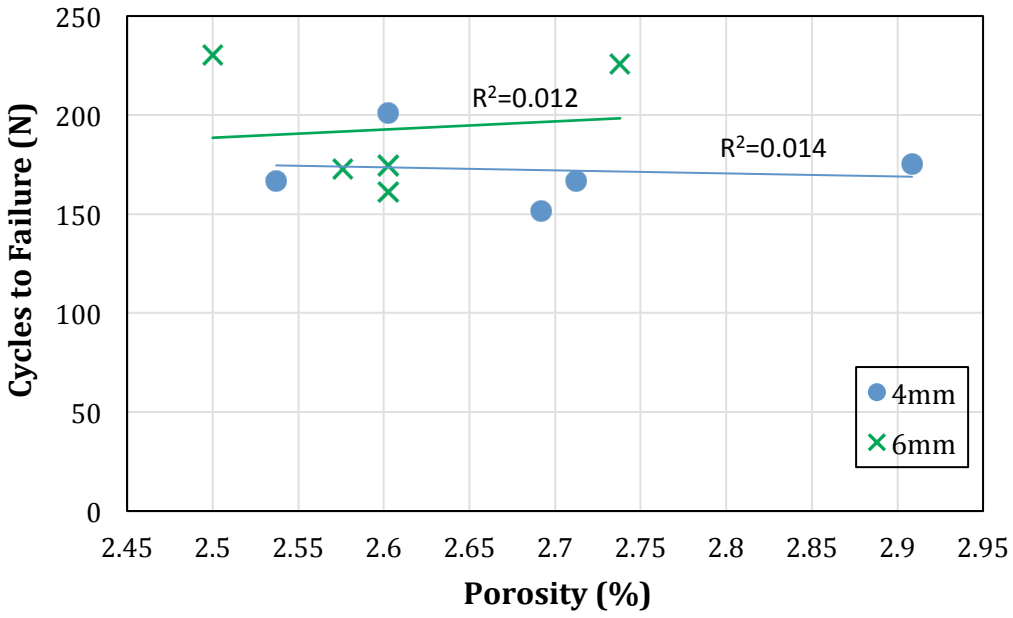

Figure 10-6- Number of cycles to failure vs. porosity for stress level of 30MPa

10-5- Summary

To get a better understanding of the internal morphology of the samples and its influence on their performance, Samples were CT-scanned and their porosity, pore size and pore size distribution was measured. Thicker samples were shown to have a higher percentage of porosity and higher percentage of larger pore diameters which was attributed to the longer period they stay at elevated temperature and the possibility of gas formation.

Scanned samples were subjected to cyclic loading to examine the relationship between their fatigue life and their porosity. Results in this chapter indicated that no apparent relationship existed between porosity of parts and their tension-compression fatigue life.

11. Effect of Sample Temperature

11-1- Methodology

A third batch of samples was manufactured with the same powder and build parameters as the first two batches. As observed in previous tension-compression cyclic experiments, samples seemed to have a rise in their temperature up to the point they broke. In this set of experiments, the temperature of the samples was recorded while they were subjected to tension-compression cyclic loading with test parameters the same as Chapter 9 to observe their exact thermal behaviour.

11-2- Cyclic Tests with Temperature Recording

According to earlier observations and previous studies [68], samples experience temperature rise while cycling under tension-compression loading. Thermal history of the samples was recorded using a thermal camera to enable investigating the effect of this phenomenon on cyclic behaviour of samples.

11-2-1- Test Settings

Samples of 4mm and 6mm section thickness were fixed in the MTS machine as described previously. Samples were subjected to force-controlled tension-compression cyclic loading with test conditions described in Chapter 9.

11-2-2- Thermal (Infrared) Camera

A Micro-epsilon ThermoIMAGER was employed to record the temperature of the samples while under tension-compression testing. The camera was set at a 200mm distance from the sample to cover the entire sample length (Figure 11-1a).

The camera was connected to a computer and "TIM Connect" software was used to control and analyse the real time thermography. An area of interest as shown in Figure 11-1b was defined to restrict temperature analysis to the sample's gauge area and not the surroundings. Maximum temperature within the area of interest was recorded. Frequency of temperature recording was chosen as 100Hz to record one data map per hundredth of a second.

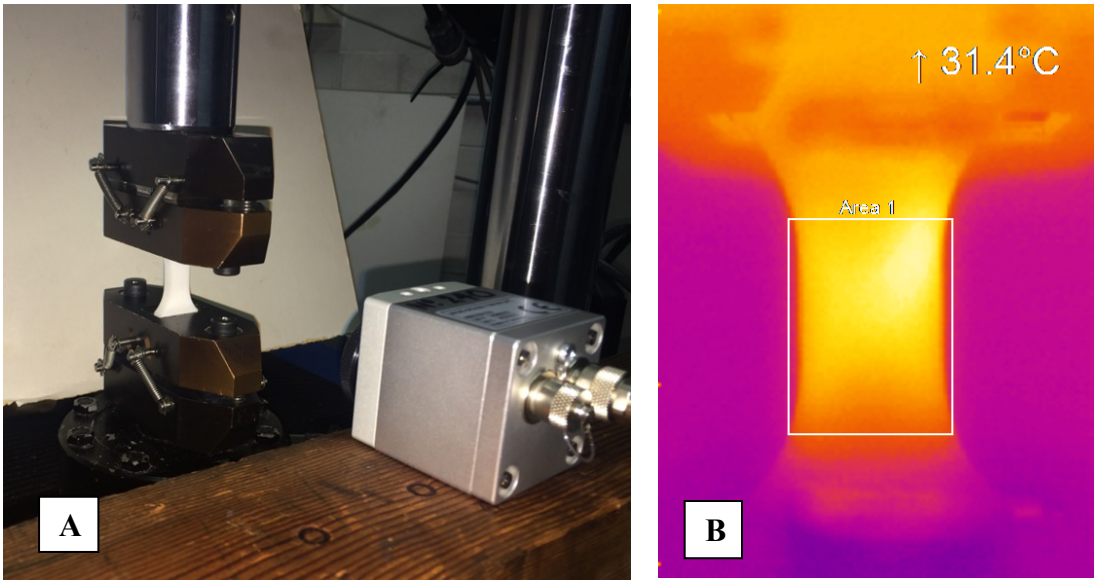

Figure 11-1- a) thermal camera setup, b) sample's thermal image

11-2-3- Thermal Camera Calibration

The thermal camera had to be calibrated to the emissivity of the material under testing to provide accurate thermal data. In order to achieve this, a small hole was drilled in the centre of the thickness surface and gauge length of a sample up to half of its width. A thermocouple was inserted to the hole. Temperature of the sample was recorded by the thermocouple and the thermal camera at the same time, while the sample was subjected to cyclic tension-compression loading. The test setting is shown in Figure 11-2.

The emissivity of the material was altered on the software so both the camera and the thermocouple would show the same temperature throughout testing. Emissivity of the material was recorded as 0.95 which is close to the values reported by the literature [50].

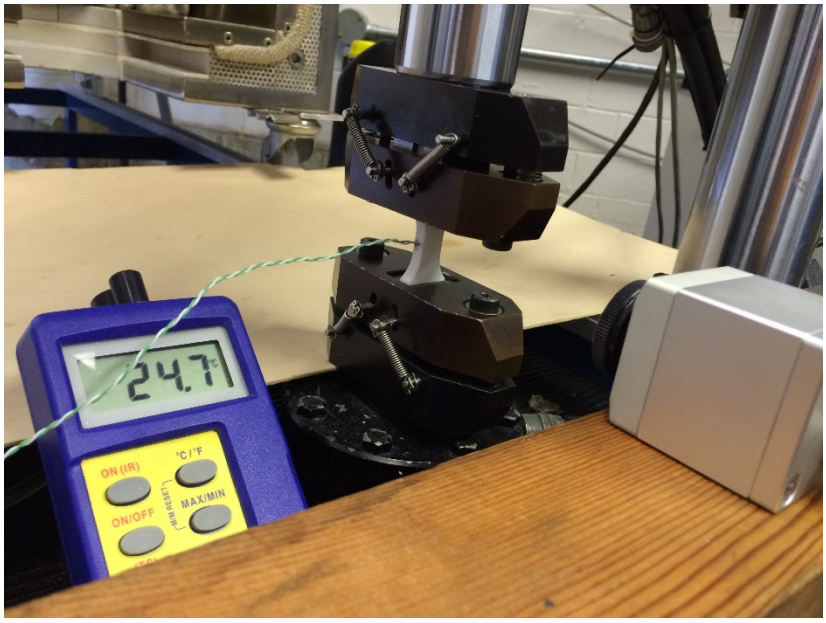

Figure 11-2 – Test setting for calibrating the thermal camera

11-2-4- Results and Discussion

Section Thickness

The number of cycles to failure of samples was plotted against their section thickness for the examined stress levels in this set of samples as well, to compare with the results from last set and examine consistency of the findings. These plots are presented in Figures 11-3 and 11-4.

As can be observed from the figures, the number of cycles to failure of samples in the same stress level are in a similar range. This range is also similar to the previous set of results which shows a good consistency in the obtained data. However, it is clear that the number of cycles increases with section thickness in both stress levels. While this is in line with findings of the previous set for the higher stress level, for the lower stress level it seems that the results contradict each other.

Similar to the previous set, Mann-Whitney U test was performed on the results to evaluate the significance of the difference between the results from each stress level. In both of the

stress levels a significant difference was revealed between fatigue life of samples of the two groups of section thickness (4mm section thickness; U=6, p=0.032 and 6mm section thickness; U=2, p=0.028).

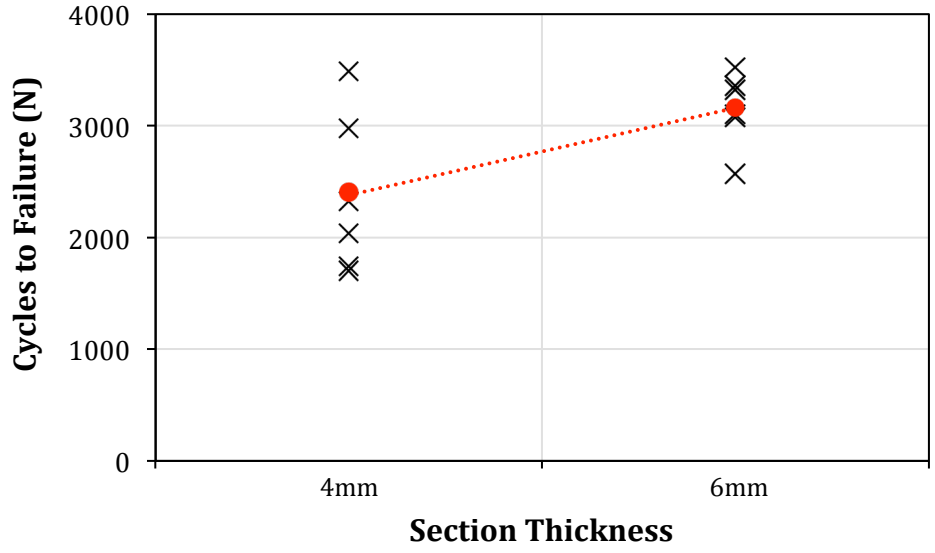

Figure 11-3- Number of cycles vs. section thickness for stress level of 20 MPa

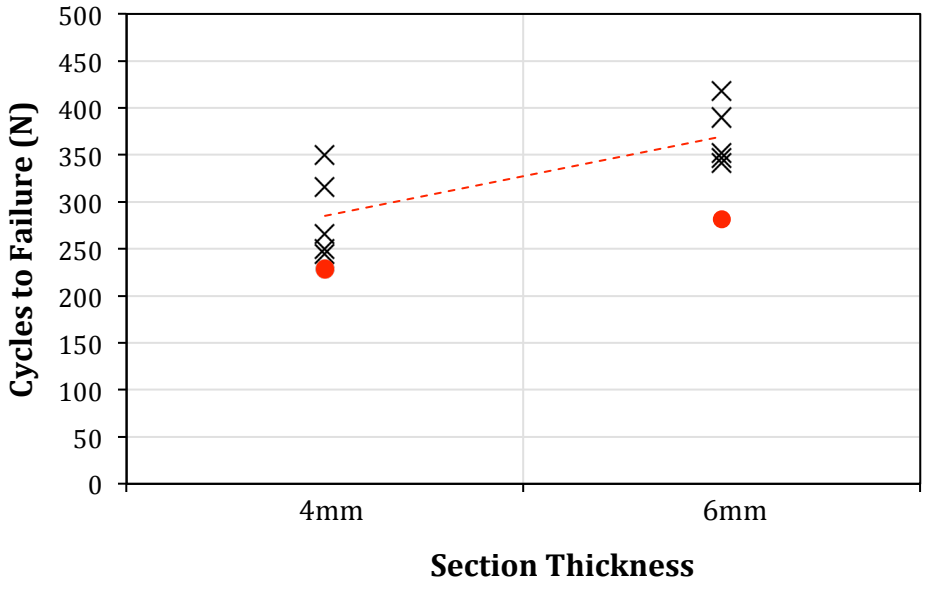

Figure 11-4 - Number of cycles vs. section thickness for stress level of 30 MPa

Temperature

Hysteresis heating seemed to have a major role in failure of samples under tension-compression cyclic loading. Maximum temperature of samples in each cycle was plotted against the number of cycle to produce thermal history plots of samples up to their failure point. These images are presented in Figures 11-5 and 11-6 for stress levels of 20MPa and 30MPa respectively.

The energy dissipated per second can be obtained from the following equation [59]:

$$\dot{E} = \pi f J''(f, T, \sigma)\sigma^2 \qquad (11\text{-}1)$$

where f is the applied frequency, σ is the peak stress and J'' is the loss compliance of the material. Part of this energy is transferred to the surrounding by means of conduction, convection and radiation and the rest results in hysteresis heating of the sample. Hence, the resulting temperature rise of sample is expected to increase with increase of frequency and stress amplitude. This phenomenon can be seen in comparing Figures 10-5 and 10-6. Temperature clearly rises more rapidly in the higher stress level leading to a faster failure of the samples in that stress level.

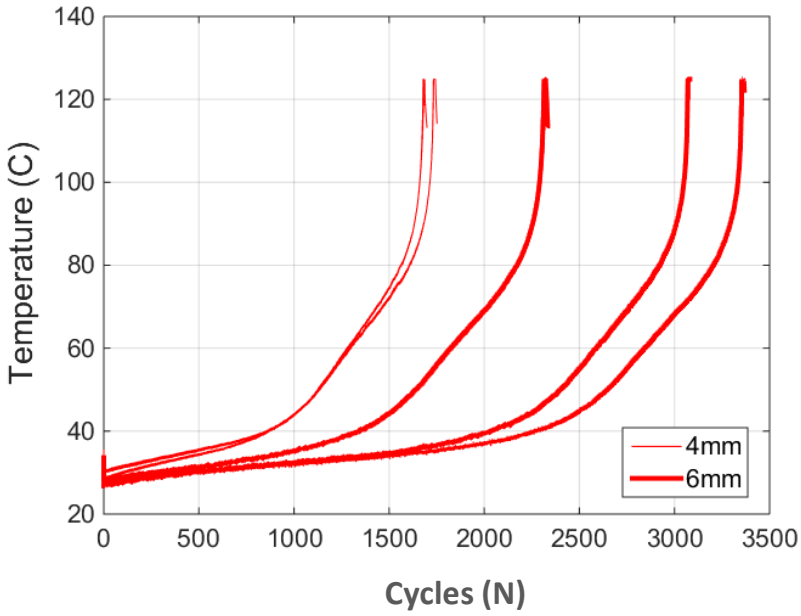

Figure 11-5- Thermal history of 4mm and 6mm samples under 20MPa stress level

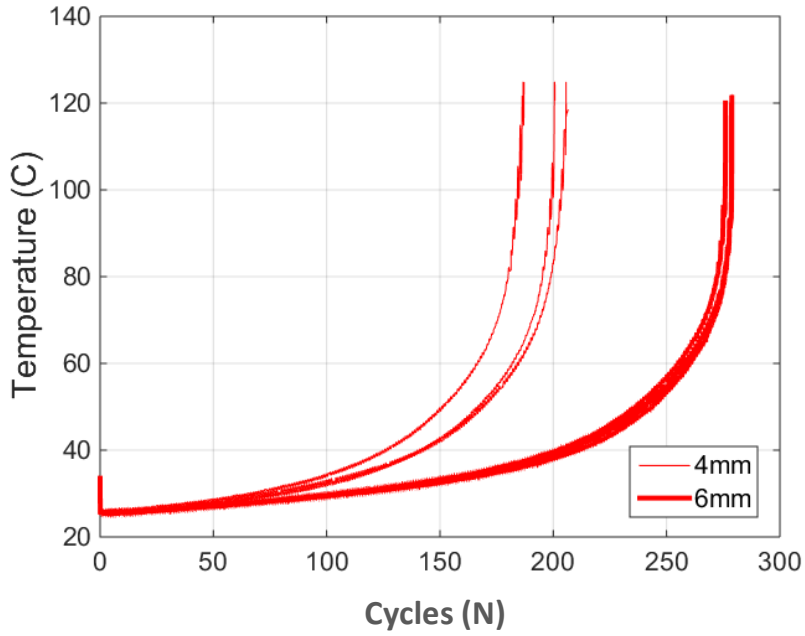

Figure 11-6- Thermal history of 4mm and 6mm samples under 30MPa stress level

One of the inconsistencies observed in the results from the hysteresis loops and the temperature histories of the samples, is that while the thicker samples were shown to dissipate more energy in each cycle their heating rate is lower than the thinner samples.

It can also be observed that in all of the plots, temperature rises linearly at first, up to around 35°C. Similar behaviour has been reported by Van Hooreweder et al [51]. After this temperature, thermal behaviour of the samples changes under different stress levels, while it is similar for different section thicknesses with the same stress level. Once the maximum temperature in a sample hits the T_g range, all samples in the same stress level fail within similar number of cycles. This is more certain in the higher stress level. Figure 11-7a and b show the number of cycles to failure of samples in 20MPa and 30MPa stress levels after their temperature reach 55°C. This temperature was chosen as the mid-range of the samples' T_g.

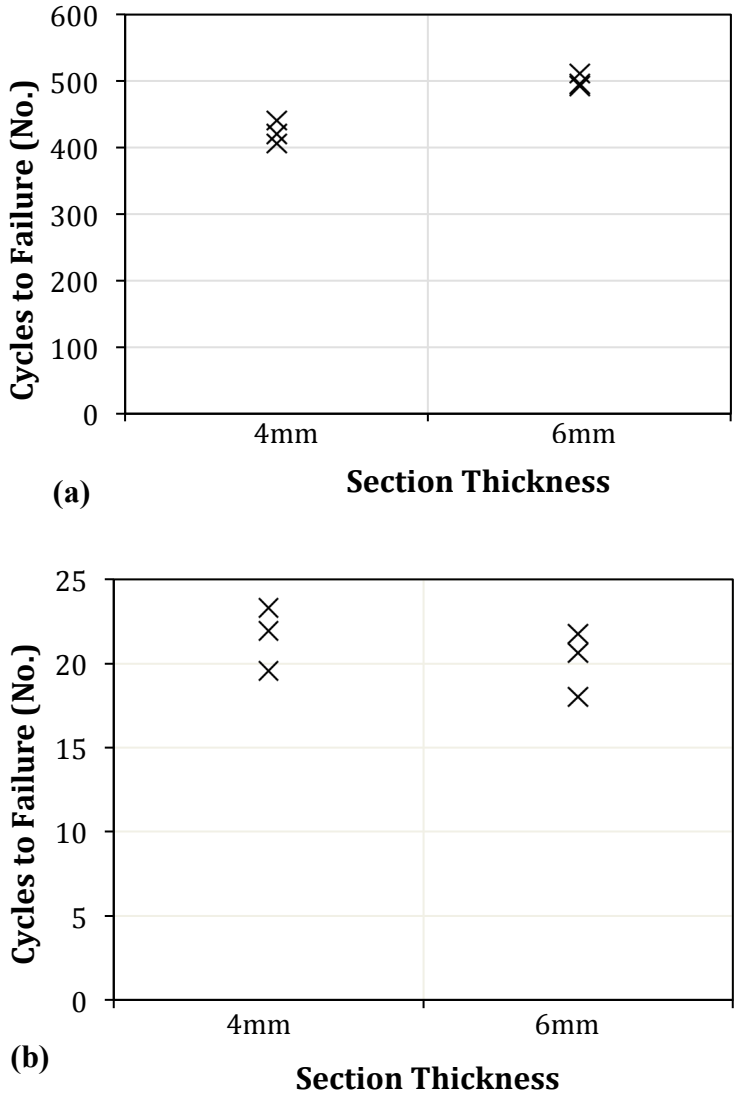

Figure 11-7- Number of cycles to failure past the glass transition temperature (55°C) - a)20MPa, b)30MPa

The reason for this behaviour of the samples can be explained as follows. At the start of testing, amorphous chain segments of the polymer are frozen in fixed positions with their segments vibrating around these fixed positions. Thermal energy at this temperature is not large enough to overcome the potential barriers for larger motions of these segments of the polymer. As the temperature starts to increase, and reaches the glass transition temperature, the amplitude of vibrational motion increases, and eventually the thermal energy becomes large enough to overcome the potential energy barriers to segment rotation and translation. This leads to softening of the amorphous polymers chains, hence fall in elastic modulus as shown in section 7-5-5 and as a result, larger deformation of the sample under the same load.

Larger deformations cause more friction between the chains; therefore larger temperature rise in the sample. This phenomenon continues and accelerates itself until rupture of the sample occurs.

In order to obtain a better understanding of the explained process, strain vs. temperature graphs of two 4mm samples under 20MPa and 30MPa stress levels were plotted as shown in Figures 11-8 and 11-9 respectively. It is clear from the plots that as samples experience cyclic loading, their temperature and their strain due to a constant stress begin to increase. Samples strained to about 30% of their EaB before they hit their T_g range (48-62°C), although the strain value is larger for the larger stress level. As can be observed, after the samples reached the T_g, slopes of the plots increase which means a larger change in strain value for the same change in temperature value.

Although samples showed different behaviours under different stress levels and besides their different number of cycles to failure, it is clear from Figures 10-5 and 10-6 that all of the samples have broken in the same temperature range. Thermal history plots in these figures indicate that once the sample got to a temperature range of 120-125°C all samples have failed no matter their size and stress level. A similar surface temperature at failure (130°C) has been reported by Van hooreweder et al [51].

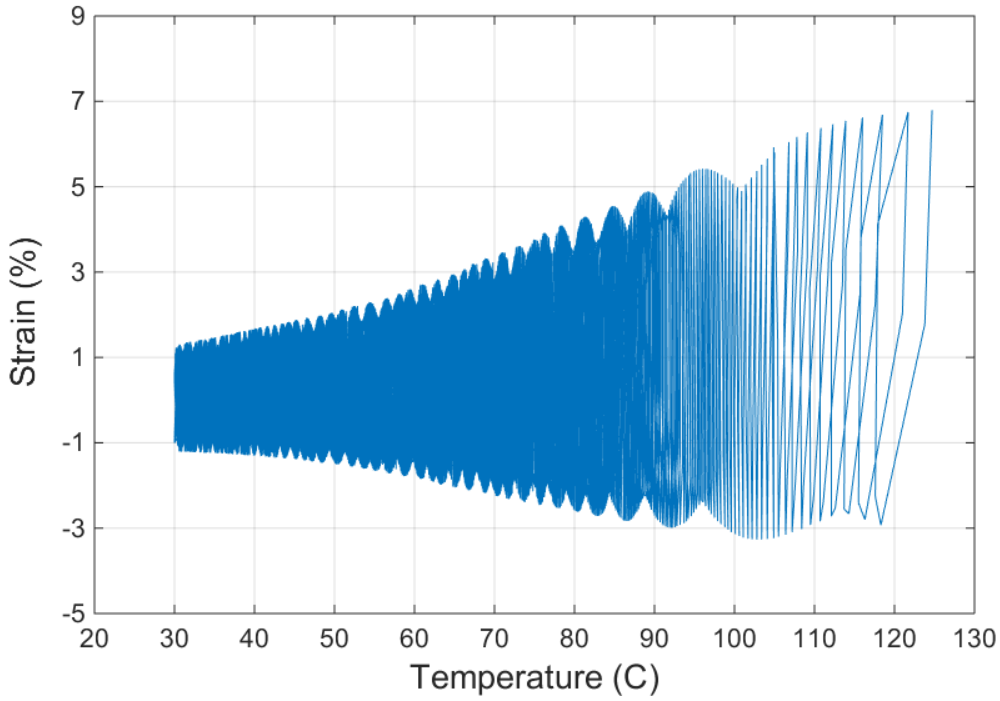

Figure 11-8- Strain vs. temperature for a 4mm sample under cyclic load with 20MPa stress (100 data points per second)

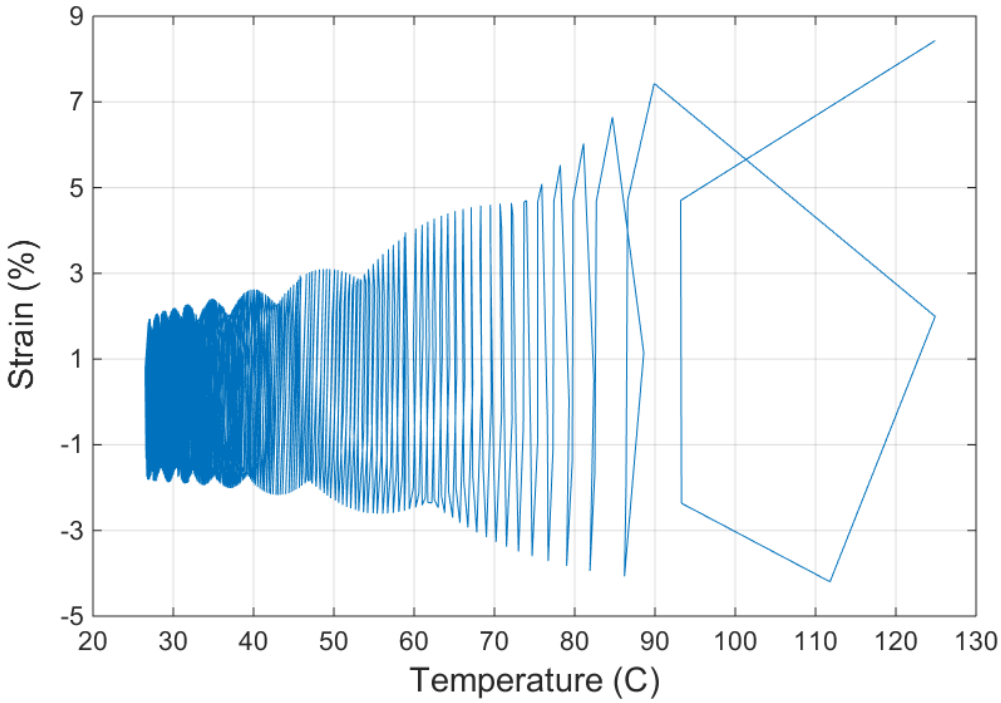

Figure 11-9- Strain vs. temperature for a 4mm sample under cyclic load with 30MPa stress (10 data points per second)

11-3- Cyclic Tests with Cooling and Temperature Recording

Results obtained in Section 11-2 indicated that temperature rise had a major role in failure of samples under tension-compression loading. In this set of experiments forced convection was applied to the samples while they were cycling. The number of cycles to failure of the samples and their surface temperature was recorded to examine the possible influence of cooling on them.

11-3-1- Test Settings

Samples and cyclic loading settings were the same as the test settings described in section 10-2-1. A Micro-epsilon infrared camera was employed to measure surface temperature of the samples. In order to apply forced convection, a 200mm diameter fan heater was used. During this set of experiments, the fan was switched on but the heating elements were not. Since the fan only had one speed, it was moved closer to or further from the sample to create different air speeds for the forced convection. The test setup for this set of experiments is shown in Figure 11-10.

To make the setup repeatable, air speed near the sample was measured using a TSI VelociCalc Plus air velocity meter. The probe of the instrument was placed beside the sample, so air could move through it without any obstacles, while the fan was on. Two fan positions of 1 metre and 3 metres from the sample, and consequently air speeds of 0.5mm/s and 1.5mm/s, were chosen for these experiments.

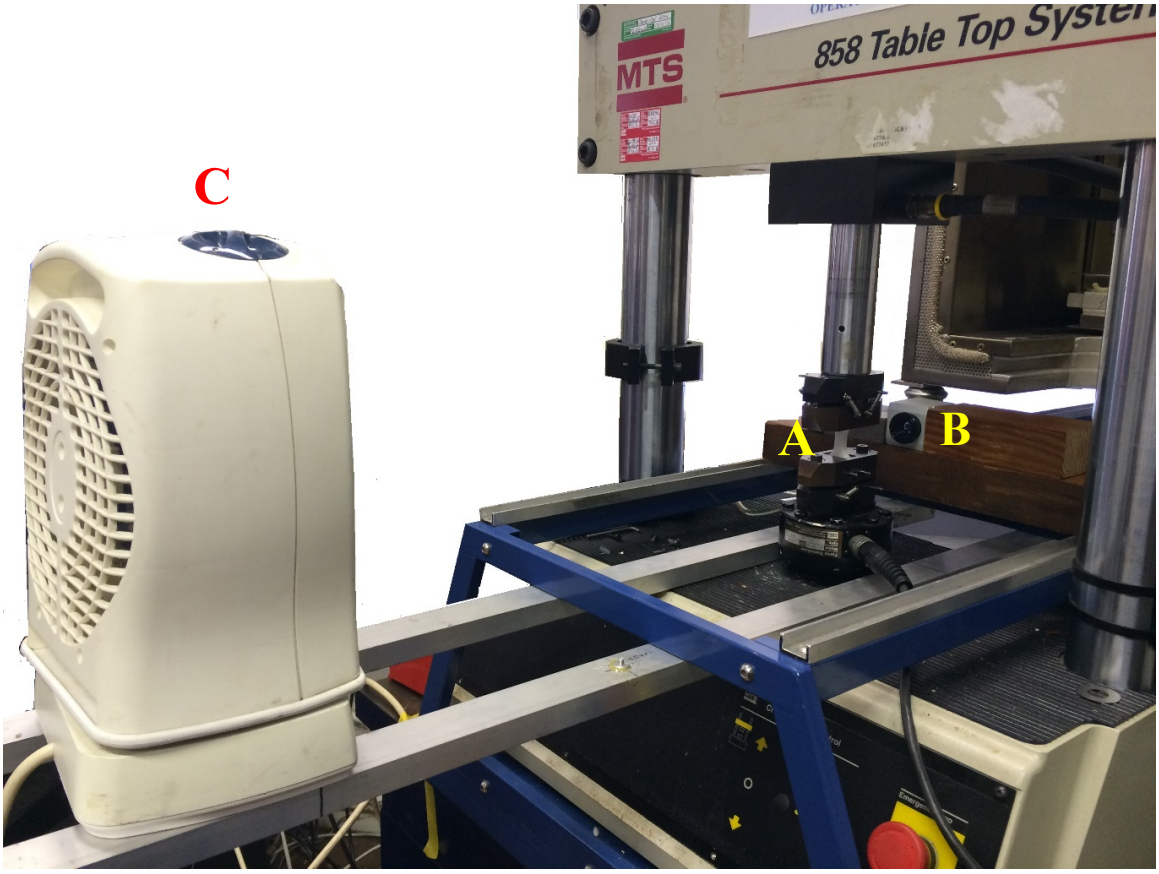

Figure 11-10- Experiment setup for cyclic tests with temperature recording and cooling A)sample, B)infrared camera, C)fan

11-3-2- Results and Discussion

As expected, cooling the samples while cycling under tension-compression loading improved their fatigue life. As shown in Figures 11-11 and 11-12, the number of cycles to failure of the samples increased as they were subjected to forced convection during testing. However, this effect was highly influenced by the rate of heating of the samples due to the stress level and the rate of cooling applied to the samples.

Figure 11-11 shows maximum temperature history of 4mm and 6mm samples under tension-compression loading with 20MPa peak stress level subjected to forced convection with air speeds of 0.5mm/s and 1.5mm/s. Samples under cooling rate of 1.5mm/s lasted for 24hours (170000 cycles) of testing and were removed from the machine at this point. Figure 11-12 shows the same for samples under 30MPa peak stress level.

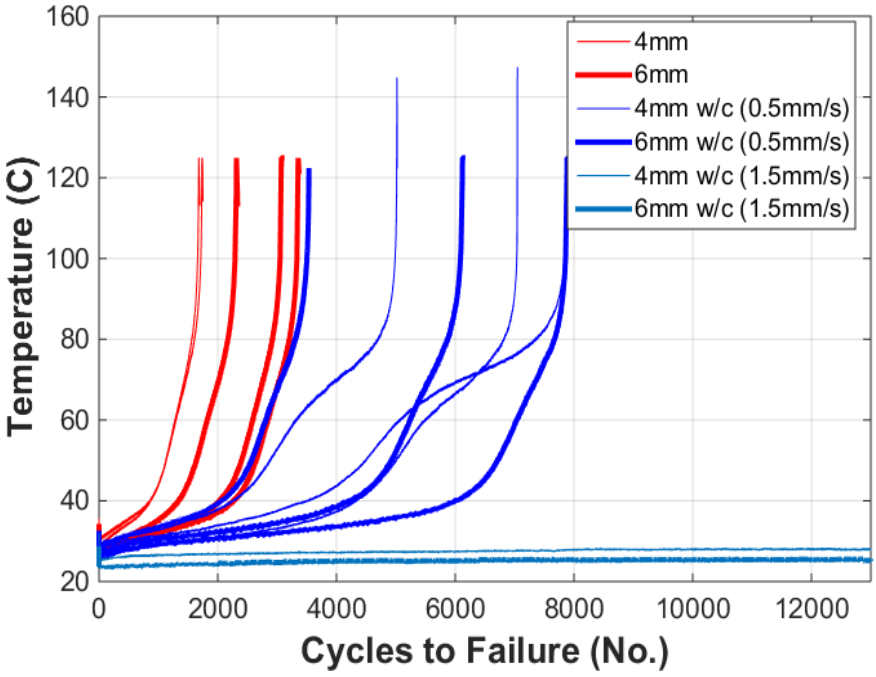

Figure 11-11- Temperature history of cooled and un-cooled samples under cyclic load with 20MPa stress amplitude

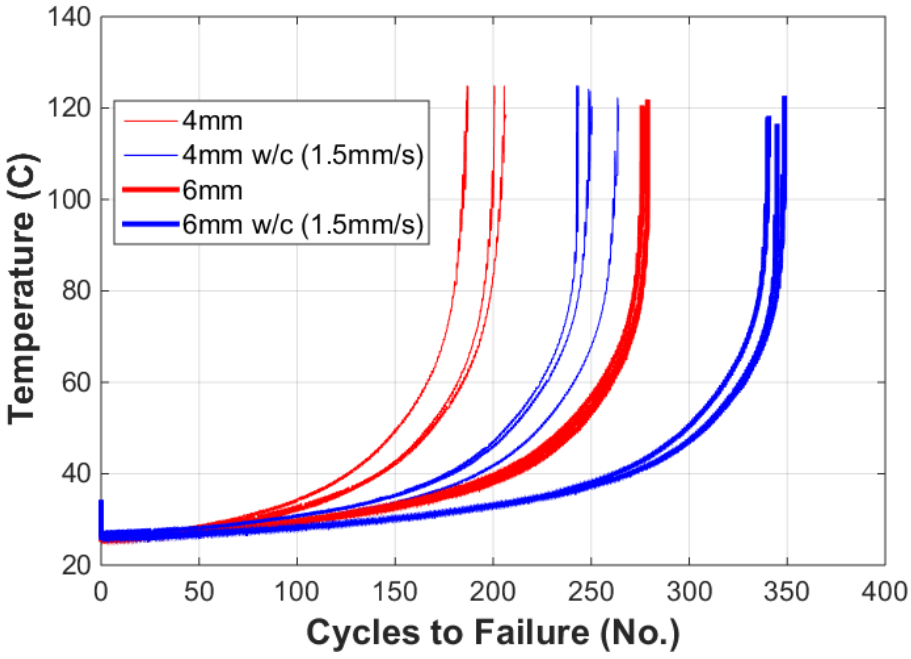

Figure 11-12- Temperature history of cooled and un-cooled samples under cyclic load with 30MPa stress amplitude

Plots in Figure 11-11 indicate that if the sample's temperature is prevented from reaching the critical temperature of around 35°C, by applying a higher rate of cooling, the samples could last for at least 50 times their usual fatigue life. This can be seen in the plots for 1.5mm/s air

speed (light blue plots). However, once the temperature of the samples increased beyond 35°C, although their number of cycles to failure was higher than uncooled samples, the samples experienced thermo-mechanical failure.

Comparing Figures 11-11 and 11-12, it is clear that the cooling rate that significantly increased the fatigue life of samples under the lower stress level, did not have a major influence on fatigue life of samples under the higher stress level. This is due to the higher rate of heat generation in the samples subjected to the higher stress level.

Although samples showed different temperature histories based on their section thickness and applied stress level, it can be observed from Figures 11-11 and 11-12 that, except two of the 4mm samples, all samples have broken within the temperature range of 115-125°C no matter they were uncooled or cooled.

Fatigue life of cooled and uncooled 4mm and 6mm samples are shown in Figures 11-13 and 11-14 for 20MPa and 30MPa stress levels respectively. Cooled samples under 20MPa stress level were subjected to air speed of 0.5mm/s, while the air speed for cooled samples under 30MPa stress level was 1.5mm/s.

Figure 11-13 shows that while the fatigue life of samples generally increased due to cooling, no apparent consistency can be observed in the increase in their number of cycles to failure, i.e. in the 6mm section thickness sample's fatigue life has increased by 4 times while another's has changed by a few cycles. More consistent results can be observed in Figure 11-14 for 30MPa stress level.

Calculating statistical significance of the difference in results from the cooled and uncooled samples for both stress levels using Mann-Whitney U test, the α values obtained were larger than 0.05. This showed that no real statistical significance existed in increasing the number of cycles to failure of samples due to cooling. However, the lack of statistical significance in this case might be due to the small number of statistical samples.

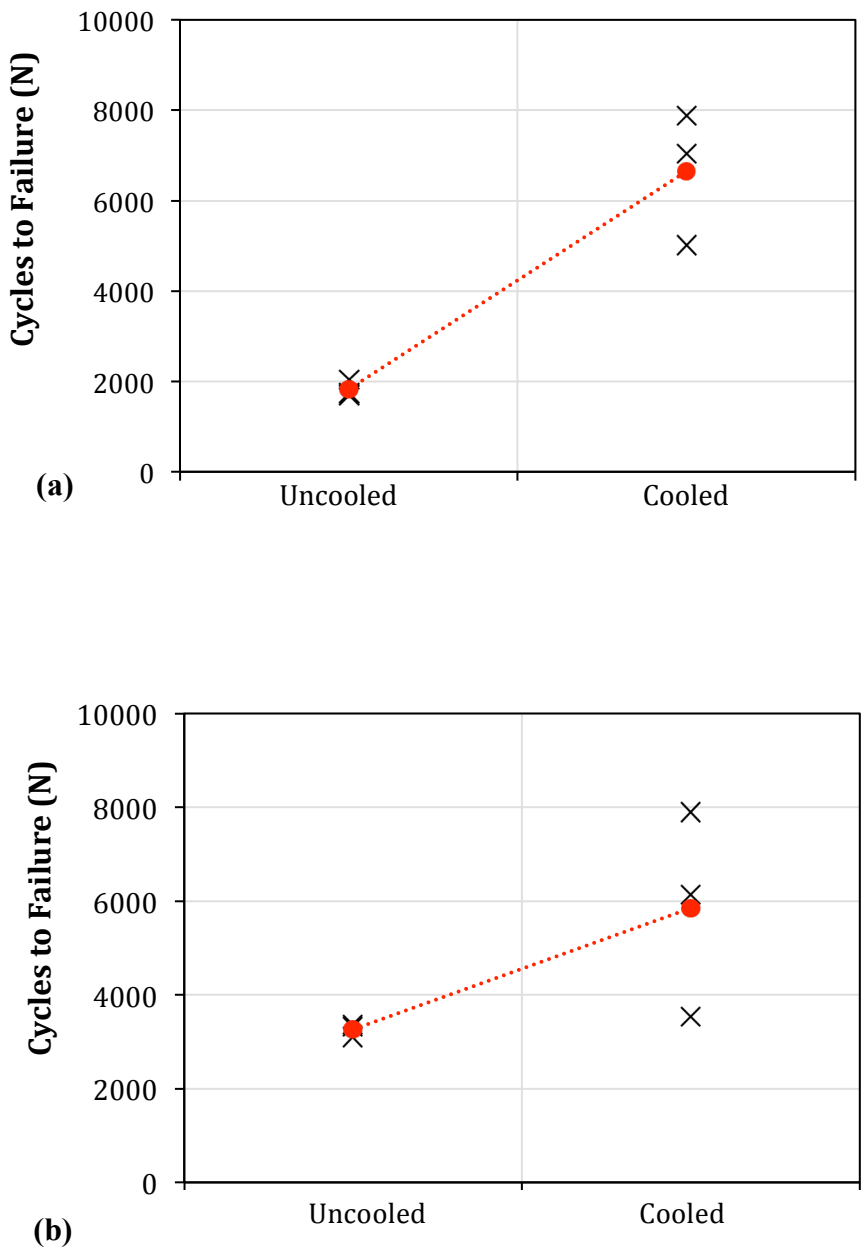

Figure 11-13- Number of cycles for cooled (0.5mm/s air speed) and non-cooled a)4mm and b)6mm samples, stress level of 20 MPa

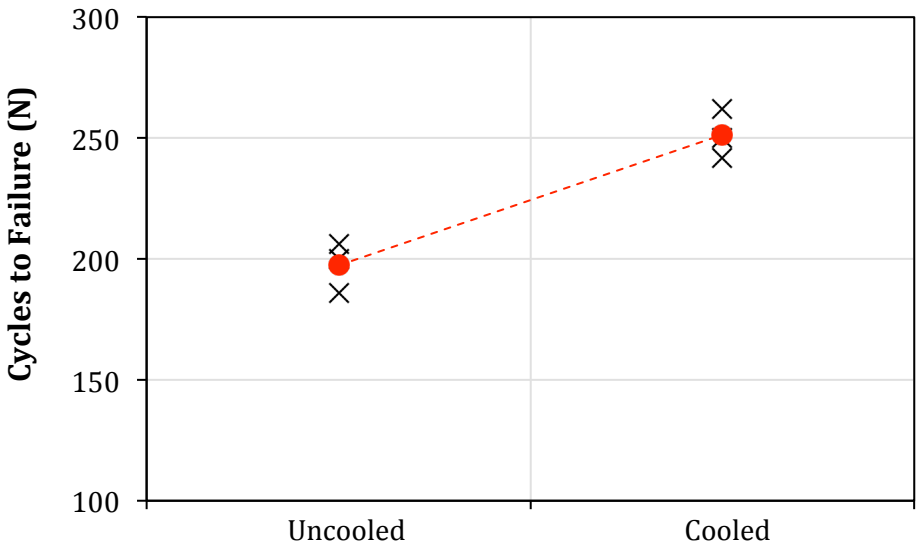

(a)

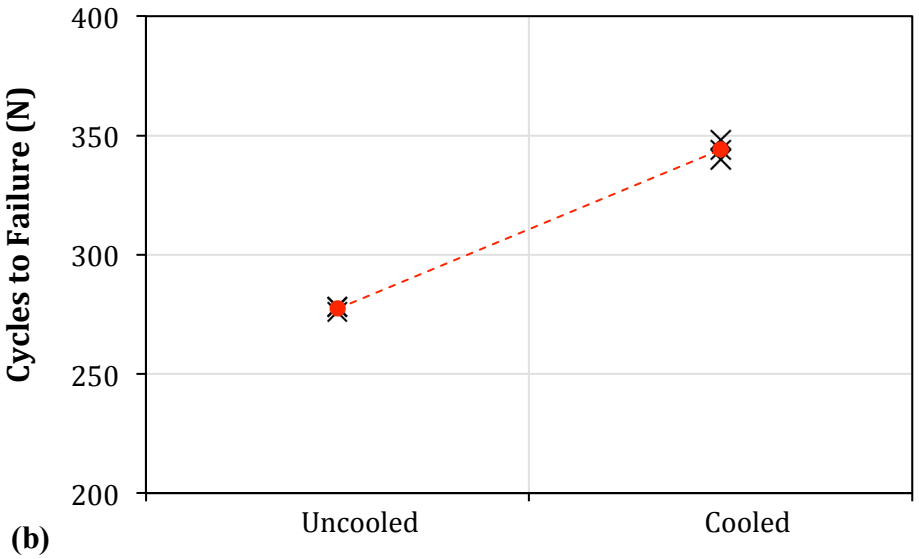

(b)

Figure-11-14- Number of cycles for cooled (1.5mm/s air speed) and non-cooled a)4mm and b)6mm samples, stress level of 30 MPa

11-4- Summary

Thermal behaviour of samples subject to tension-compression load-controlled cyclic loading was studied in this chapter. Samples' surface temperature was recorded using an infrared camera and thermal history of the samples was reported. It was observed that samples' temperature change was influenced by the stress level they were subjected to as well as their section thickness. However, despite their differences, all samples broke in a similar temperature range.

Forced convection was used to decrease the rate of samples' heating under tension-compression loading. It was shown that by preventing the samples from reaching a certain temperature range, samples life could be increase by at least 50 times its normal fatigue life. Even with cooling, the majority of samples still broke within the same temperature range as uncooled samples.

12. Conclusions and Future Work

12-1- Conclusions

Performance of Laser Sintered Nylon 12 parts under dynamic loading was investigated in the present work. Viscoelastic properties of the material were obtained and influence of three important factors in design and in-service applications; section thickness, porosity and temperature (hysteresis heating), on performance of parts was studied and unique findings were presented. This section outlines the primary conclusions gained from this work. All comments are valid within the ranges tested in this research work and may not be applicable outside of these ranges.

12-1-1- Effect of Section Thickness on Mechanical Behaviour

Previous studies have shown that section thickness had no influence on tensile properties of LS Nylon 12 samples, while results from this study indicated that Elongation at Break, Ultimate Tensile Strength and Young's Modulus of samples increased as the thickness of the parts increased. This increase was shown to be statistically significant UTS and Young's Modulus but not significant in EaB.

Fatigue life of LS Nylon 12 samples subject to tension-tension cyclic loading was shown to increase with increase of section thickness. However, no consistent influence of section thickness on fatigue life of samples under tension-compression cyclic loading was observed

for any of the stress levels tested for sample sets manufactured in different builds of the LS machine but with the same powder and build parameters. Hysteresis loops of samples showed that thicker samples dissipate more energy while cycling, although according to thermal history plots they heat up at a lower rate.

12-1-2- Effect of Porosity on Fatigue Behaviour

Morphology of samples was studied using their micro-CT scans and their porosity was measured. Porosity of samples was shown to increase with section thickness and thicker samples were observed to have a larger percentage of pores with larger diameters. However, this parameter did not have any apparent influence on the samples' tension-compression cyclic performance.

12-1-3- Effect of Temperature on Fatigue Behaviour

Samples' thermal behaviour under tension-compression loading was shown to be influenced by the peak stress level of their cyclic loading and their section thickness. Samples at higher stress levels showed higher heating rates than samples at lower stress levels and thicker samples had lower heating rates than thinner samples. Although samples showed different thermal behaviour based on their stress level and section thickness, all samples tested at room temperature broke in a similar temperature range.

Cooling the samples while cycling using forced convection reduced their heating rate and increased their fatigue life. It was also shown that preventing the samples from reaching a certain temperature range significantly increased their life under tension-compression cyclic loading. Even with cooling, the majority of samples still broke within the same temperature range as uncooled samples.

12-1-4- Tensile Cyclic Behaviour

Signs of cyclic creep or strain ratcheting was observed during tension-tension cyclic loading, therefore a pure tensile cyclic loading was not achieved. Both fracture surfaces of tensile and tensile cyclic samples and hysteresis loops of tensile cyclic samples showed signs of brittle fracture. Also, drawn curled fibrils were observed in tensile cyclic samples, which were associated with crazing of the sample before fracture.

Samples of the same section thickness showed different behaviours under the same tensile cyclic loading conditions. No apparent relationship existed between the samples behaviour and their density or surface roughness. This was not the case for samples subjected to stress relaxation.

12-2- Recommendations for Future Work

This chapter covers a selection of further work recommendations. Some build upon aspects of the current research that could benefit from additional investigation, whilst others relate to new areas of study which fell outside the scope of this research.

12-2-1- Effect of Sintering Parameters on Cyclic Performance

As explained in Chapter 3, build parameters specifically the Energy Density (ED) supplied to the powder particles during the sintering process can influence the mechanical properties of the final part. Previous studies have shown the effect of different ED parameters; Laser Power (LP), Scan Spacing (SS) and Beam Speed (BS) on tensile properties of parts. Samples employed in the current study and other studies on fatigue properties of LS samples were produced using standard machine parameters. A study could be conducted on investigating the influence of build parameters on cyclic performance of parts. ED parameters could be varied to establish the significance of each parameter on fatigue life of samples of the same geometry under the same loading conditions.

12-2-2- Effect of Sintering Parameters on Viscoelastic Behaviour

Cyclic performance of parts in reversed loading was shown to be highly influenced by their viscoelastic properties. Valuable findings could be achieved from studying the effect of different build parameters, e.g. ED parameters, on viscoelastic properties of parts. Viscoelasticity of parts is affected by their molecular arrangements and molecular weight, and the sintering process determines the properties of the part at molecular level. Therefore, changing the parameters that define the sintering quality of the material could significantly influence the viscoelastic properties of it.

12-2-3- Extended Life Cycle Testing

Due to limitations, in the current study samples were removed from the machine after 24 hours of testing in tension-compression cyclic loading if they did not break. It could be useful to examine the actual fatigue life of samples when they are prevented from heating by the use of forced convection. Fracture surface of the samples could be studied to determine failure of the parts if they do not experience hysteresis heating.

12-2-4- Finite Element Modelling

A finite element model can be generated using the Prony terms provided in this research to numerically simulate the viscoelastic behaviour of the samples. Fully implementing the viscoelastic properties in to model, in such way that hysteresis heating in cyclic loading could be simulated, could make a great contribution to future research on cyclic properties of parts. It is also sensible to examine the differences between the actual sample with pores, using micro-CT scans, and a bulk sample in FE analysis.

References

[1] P. K. Mallick, *Materials, Design and Manufacture for Leightweight Vehicles*. 2010.

[2] J. Happian-Smith, *An Introduction to Modern Vehicle Design*. Reed Educational and Professional Publishing Ltd, 2001.

[3] A. Mazzoli, "Selective laser sintering in biomedical engineering.," *Med. Biol. Eng. Comput.*, vol. 51, no. 3, pp. 245–56, Mar. 2013.

[4] D. . Pham and R. . Gault, "A comparison of rapid prototyping technologies," *Int. J. Mach. Tools Manuf.*, vol. 38, no. 10–11, pp. 1257–1287, Oct. 1998.

[5] I. Gibson, R. D.W., and S. B., *Additive manufacturing technologies: rapid prototyping to direct digital manufacturing*. Springer, 2009.

[6] N. Hopkinson, R. J. M. Hague, and P. M. Dickens, *Rapid Manufacturing: an Industrial Revolutin for Digital Age*. John Wiley and Sons Ltd, 2005.

[7] "Desktop Engineering website." [Online]. Available: www.deskeng.com/articles/aaayyx.htm.

[8] "3D Systems website." [Online]. Available: www.formero.com.au.

[9] N. Hopkinson and P. Dickens, "Analysis of rapid manufacturing — using layer manufacturing process for production," *Proc. Inst. Mech. Eng. Part C J. Mech. Eng.*, vol. 217, no. 1, pp. 31–39, 2003.

[10] T. T. Wohlers, "Wohlers Report 2011-Additive Manufacturing and 3D printing state of the industry annual worldwide report," 2011.

[11] P. J. Bartolo, *Stereolithography: Materials, Processes and Applications*. Springer, 2011.

[12] E. Tekin, P. J. Smith, and U. S. Schubert, "Inkjet printing as a deposition and patterning tool for polymers and inorganic particles," *Soft Matter*, vol. 4, no. 4, p. 703, 2008.

[13] C. K. Chua, K. F. Leong, and C. S. Lim, *Rapid Prototyping: Principles and Applications*, 3rd ed. World Scientific Publishing Co. Pte. Ltd, 2010.

[14] R. D. Goodridge, C. J. Tuck, and R. J. M. Hague, "Laser sintering of polyamides and other polymers," *Prog. Mater. Sci.*, vol. 57, no. 2, pp. 229–267, 2012.

[15] J.-P. Kruth, P. Mercelis, J. Van Vaerenbergh, L. Froyen, and M. Rombouts, "Binding mechanisms in selective laser sintering and selective laser melting," *Rapid Prototyp. J.*, vol. 11, no. 1, pp. 26–36, 2005.

[16] P. K. Venuninod and W. Ma, *Rapid Prototyping: Laser-Based and other Technologies*. Luwer Academic Publishers Group, 2004.

[17] J.-P. Kruth, M. C. Leu, and T. Nakagawa, "Progress in Additive Manufacturing and Rapid Prototyping," *CIRP Ann. - Manuf. Technol.*, vol. 47, no. 2, pp. 525–540, 2007.

[18] W. E. Katstra, R. D. Palazzolo, C. W. Rowe, B. Giritliglu, P. Teung, and M. J. Cima, "Oral dosage forms fabricated by Three Dimensional Printing.pdf," *J. Control. release*, vol. 66, pp. 1–9, 2000.

[19] A. Bellini and S. Güçeri, "Mechanical characterization of parts fabricated using fused deposition modeling," *Rapid Prototyp. J.*, vol. 9, no. 4, pp. 252–264, 2003.

[20] W. Y. Zhou, S. H. Lee, M. Wang, W. L. Cheung, and W. Y. Ip, "Selective laser sintering of porous tissue engineering scaffolds from poly(L: -lactide)/carbonated hydroxyapatite nanocomposite microspheres.," *J. Mater. Sci. Mater. Med.*, vol. 19, no. 7, pp. 2535–40, Jul. 2008.

[21] J. M. Williams, A. Adewunmi, R. M. Schek, C. L. Flanagan, P. H. Krebsbach, S. E. Feinberg, S. J. Hollister, and S. Das, "Bone tissue engineering using polycaprolactone scaffolds fabricated via selective laser sintering.," *Biomaterials*, vol. 26, no. 23, pp. 4817–27, Aug. 2005.

[22] "Envisiontech." [Online]. Available: http://www.envisiontec.com.

[23] J. Kruth, G. Levy, R. Schindel, T. Craeghs, and E. Yasa, "Consolidation of Polymer Powders by Selective Laser Sintering," *Ann CIRP*, vol. 56, no. 2, 2007.

[24] R. M. German, *Sintering Theory and Practice*. New York: John Wiley and Sons Ltd, 1996.

[25] J.-P. Kruth, G. Levy, F. Klocke, and T. H. C. Childs, "Consolidation phenomena in laser and powder-bed based layered manufacturing," *CIRP Ann. - Manuf. Technol.*, vol. 56, no. 2, pp. 730–759, Jan. 2007.

[26] C. Davidson, "Investigating the Suitability of Laser Sintered Elastomers for Running Footwear Applications," 2012.

[27] J. P. Kruth, X. Wang, T. Laoui, and L. Froyen, "Lasers and materials in selective laser sintering Lasers and materials in selective laser sintering," *Rapid Prototyp. J.*, vol. 11, no. 1, pp. 26–36, 2003.

[28] I. Gibson and D. Shi, "Material properties and fabrication parameters in selective laser sintering process," *Rapid Prototyp. J.*, vol. 3, no. 4, pp. 129–136, 2011.

[29] A. E. Tontowi and T. H. C. Childs, "Density prediction of crystalline polymer sintered parts at various powder bed temperatures Density prediction of crystalline polymer sintered parts at various powder bed temperatures," *Rapid Prototyp. J.*, vol. 7, no. 3, pp. 180–184, 2001.

[30] R. D. Goodridge, C. J. Tuck, and R. J. M. Hague, "Laser sintering of polyamides and other polymers," *Prog. Mater. Sci.*, vol. 57, no. 2, pp. 229–267, Feb. 2012.

[31] B. Vandenbroucke and J.-P. Kruth, “SELECTIVE LASER MELTING OF BIOCOMPATIBLE METALS FOR RAPID,” *Rapid Prototyp. J.*, vol. 13, no. 4, pp. 148–159, 2007.

[32] T. L. Starr, T. J. Gornet, and J. S. Usher, “The effect of process conditions on mechanical properties of laser-sintered nylon,” *Rapid Prototyp. J.*, vol. 17, no. 6, pp. 418–423, 2011.

[33] A. Amado, M. Schmid, G. Levy, and K. Wegener, “ADVANCES IN SLS POWDER CHARACTERIZATION,” in *Proceedings SFF Symposium*, 2011, vol. 12, pp. 438–452.

[34] S. Ziegelmeier, P. Christou, F. Wöllecke, C. Tuck, R. Goodridge, R. Hague, E. Krampe, and E. Wintermantel, “An experimental study into the effects of bulk and flow behaviour of laser sintering polymer powders on resulting part properties,” *Journal of Materials Processing Technology*, vol. 215. pp. 239–250, Jan-2015.

[35] G. M. Vasquez, C. E. Majewski, B. Haworth, and N. Hopkinson, “A targeted material selection process for polymers in laser sintering,” *Addit. Manuf.*, vol. 1–4, pp. 127–138, Oct. 2014.

[36] J.-P. Kruth, G. Levy, F. Klocke, and T. H. C. Childs, “Consolidation phenomena in laser and powder-bed based layered manufacturing,” *CIRP Ann. - Manuf. Technol.*, vol. 56, no. 2, pp. 730–759, Jan. 2007.

[37] H. Zarringhalam, N. Hopkinson, N. F. Kamperman, and J. J. de Vlieger, “Effects of processing on microstructure and properties of SLS Nylon 12,” *Mater. Sci. Eng. A*, vol. 435–436, pp. 172–180, Nov. 2006.

[38] R. Hague *, S. Mansour, and N. Saleh, “Material and design considerations for rapid manufacturing,” *Int. J. Prod. Res.*, vol. 42, no. 22, pp. 4691–4708, Nov. 2004.

[39] S. Eosoly, G. Ryder, T. Tansey, and L. Looney, “Accuracy and Mechanical Properties of Open-Cell Microstructures Fabricated by Selective Laser Sintering,” *Biomaterials*, vol. 26, no. 23, pp. 4817–27, 2005.

[40] “EOS GmbH, Product Information EOSINT P/PA2200-Pulver, Manufacturer Supplied Materials Data Sheet.” [Online]. Available: 2012.

[41] “3D Systems, DuraForm PA and GF, Materials for SLS systems.” [Online]. Available: http://www.3dsystems.com/products/datafiles/lasersintering/datasheets/. [Accessed: 01-Jan-2012].

[42] B. Caulfield, P. E. McHugh, and S. Lohfeld, “Dependence of mechanical properties of polyamide components on build parameters in the SLS process,” *J. Mater. Process. Technol.*, vol. 182, no. 1–3, pp. 477–488, Feb. 2007.

[43] R. D. Goodridge, R. J. M. Hague, and C. J. Tuck, “Effect of long-term ageing on the tensile properties of a polyamide 12 laser sintering material,” *Polym. Test.*, vol. 29, no. 4, pp. 483–493, Jun. 2010.

[44] N. Hopkinson, C. E. Majewski, and H. Zarringhalam, “Quantifying the degree of particle melt in Selective Laser Sintering®,” *CIRP Ann. - Manuf. Technol.*, vol. 58, no. 1, pp. 197–200, Jan. 2009.

[45] H. C. . Ho, I. Gibson, and W. . Cheung, “Effects of energy density on morphology and properties of selective laser sintered polycarbonate,” *J. Mater. Process. Technol.*, vol. 89–90, pp. 204–210, May 1999.

[46] C. Majewski and N. Hopkinson, “Effect of section thickness and build orientation on tensile properties and material characteristics of laser sintered nylon-12 parts,” *Rapid Prototyp. J.*, vol. 17, no. 3, pp. 176–180, 2011.

[47] U. Ajoku, N. Saleh, N. Hopkinson, R. Hague, and P. Erasenthiran, “Investigating mechanical anisotropy and end-of-vector effect in laser-sintered nylon parts,” *Proc. Inst. Mech. Eng. Part B J. Eng. Manuf.*, vol. 220, no. 7, pp. 1077–1086, Oct. 2006.

[48] U. Ajoku, N. Hopkinson, and M. Caine, “Experimental measurement and finite element modelling of the compressive properties of laser sintered Nylon-12,” *Mater. Sci. Eng. A*, vol. 428, no. 1–2, pp. 211–216, Jul. 2006.

[49] M. Blattmeier, G. Witt, J. Wortberg, J. Eggert, and J. Toepker, “Influence of surface characteristics on fatigue behaviour of laser sintered plastics,” *Rapid Prototyp. J.*, vol. 18, no. 2, pp. 161–171, 2012.

[50] B. Van Hooreweder, F. De Coninck, D. Moens, R. Boonen, and P. Sas, “Microstructural characterization of SLS-PA12 specimens under dynamic tension/compression excitation,” *Polym. Test.*, vol. 29, no. 3, pp. 319–326, May 2010.

[51] B. Van Hooreweder, D. Moens, R. Boonen, J.-P. Kruth, and P. Sas, “On the difference in material structure and fatigue properties of nylon specimens produced by injection molding and selective laser sintering,” *Polym. Test.*, vol. 32, no. 5, pp. 972–981, Aug. 2013.

[52] J. Munguía, K. W. Dalgarno, and R. Reid, “Fatigue behavior of additive manufacturing parts . A preliminary analysis,” 2012.

[53] D. J. Hitt, B. Haworth, and N. Hopkinson, “Fracture mechanics approach to compare laser sintered parts and injection mouldings of nylon-12,” *Proc. Inst. Mech. Eng. Part B J. Eng. Manuf.*, vol. 225, no. 9, pp. 1663–1672, Oct. 2011.

[54] C. E. Carraher, *Introduction to Polymer Chemistry*, 2nd ed. CRC Press, Taylor and Francis Group, 2010.

[55] R. J. Young and P. Peter, *Introduction to Polymers*, 3rd ed. CRC Press, Taylor and Francis Group, 2011.

[56] T. R. Crompton, *Polymer Reference Book*. Rapra Technology Limited, 2006.

[57] N. Dusunceli and O. U. Colak, “Modelling effects of degree of crystallinity on mechanical behavior of semicrystalline polymers,” *Int. J. Plast.*, vol. 24, pp. 1224–1242, 2008.

[58] P. E. Bretz, “The Effect of Molecular Weight on Fatigue Crack Propagation in Nylon 66 and Polyacetal,” vol. 27, pp. 1707–1717, 1982.

[59] J. D. Ferry, *Viscoelastic Properties of Polymers*, 3rd ed. John Wiley and Sons Ltd, 1980.

[60] W. Tschoegl, *The phenomenological theory of linear viscoelastic behaviour*. Springer-Verlag, 1989.

[61] J. J. Aklonis and W. J. MacKnight, *Introduction to Polymer Viscoelasticity*, 2nd ed. Wiley-Interscience, 1983.

[62] DTA Dynamic Testing Agency, "Dynamic Testing of Materials," vol. 1, 1996.

[63] I. M. Ward and J. Sweeney, *Mechanical Properties of Solid Polymers*, 2nd ed. John Wiley and Sons Ltd, 1983.

[64] S. N. Zhurkov and V. S. Kuksenko, "The micromechanics of polymer fracture," *Int. J. Fract.*, vol. 11, no. 4, pp. 629–639, 1975.

[65] O. Olabisi and K. Adewale, *Handbook of Thermoplastics*. 1997.

[66] I. M. Ward and J. Sweeney, *An Introduction to the Mechanical Properties of Solid Polymers*, 2nd ed. John Wiley and Sons Ltd, 2004.

[67] R. W. Hertzberg and J. A. Manson, *Fatigue of Engineering Plastics*. Academic Press, 1980.

[68] J. A. Sauer and G. Richardson, "Fatigue of polymers," *Int. J. Fract.*, vol. 16, no. 6, pp. 499–532, 1980.

[69] A. Committee, *Fatigue Mechanisms: A Symposium*. 1979.

[70] A. F. Liu, *Mechanics and Mechanisms of Fracture: An Introduction*. 2005.

[71] S. B. Ratner and V. I. Korobov, "Self-Heating of Plastics During Cyclic Deformation," *Mekhanika Polim.*, vol. 1, no. 3, 1965.

[72] *A Guide for Fatigue Testing and the Stastistical Analysis of Fatigue Data*, Second. ASTM Special Technical Publication No. 91-A, 1963.

[73] G. Tao and Z. Xia, "Biaxial fatigue behavior of an epoxy polymer with mean stress effect," *Int. J. Fatigue*, vol. 31, no. 4, pp. 678–685, Apr. 2009.

[74] G. Tao and Z. Xia, "Mean stress/strain effect on fatigue behavior of an epoxy resin," *Int. J. Fatigue*, vol. 29, no. 12, pp. 2180–2190, Dec. 2007.

[75] S. Rabinowitz and P. Beardmore, "Cyclic deformation and fracture of polymers," *J. Mater. Sci.*, vol. 9, pp. 81–99, 1974.

[76] G. Tao and Z. Xia, "An Experimental Study of Uniaxial Fatigue Behavior of an Epoxy Resin by a New Noncontact Real-Time Strain Measurement and Control System," *Polym. Eng. Sci.*, 2007.

[77] R. W. Hertzberg and J. A. Manson, "Frequency Sensitivity of Fatigue Processes in Polymeric Solids," *Polym. Eng. Sci.*, vol. 15, no. 4, pp. 252–260, 1975.

[78] S. Arad, J. C. Radon, L. E. Culver, and I. College, “Strain Rate Dependence of Failure Processes in Polycarbonate and Nylon,” *J. Appl. Polym. Sci.*, vol. 17, pp. 1467–1478, 1973.

[79] G. C. Martin and W. W. Gerberich, “Temperature effects on fatigue crack growth in polycarbonate,” *J. Mater. Sci.*, vol. 11, pp. 231–238, 1976.

[80] Y. W. Mai and J. G. Williams, “Temperature and Environmental Effects on the Fatigue Fracture in Polystyrene,” *J. Mater. Sci.*, vol. 14, pp. 1933–1940, 1979.

[81] X. Shen, Z. Xia, and F. Ellyin, “Cyclic Deformation Behavior of an Epoxy Polymer. Part I: Experimental Investigation,” *Polym. Eng. Sci.*, vol. 44, no. 12, 2004.

[82] P. E. Bretz, R. W. Herzberg, and J. A. Manson, “Fatigue crack propagation in crystalline polymers: effect of moisture in nylon 66,” *J. Mater. Sci.*, vol. 14, no. 10, pp. 2482–2492, 1979.

[83] *Characterization and Failure Analysis of Plastics*. ASM International, 2003.

[84] J. Sauer and M. Hara, “Effect of molecular variables on crazing and fatigue of polymers,” *Crazing Polym. Vol. 2*, 1990.

[85] J. a. Sauer, E. Foden, and D. R. Morrow, “Influence of molecular weight on fatigue behavior of polyethylene and polystyrene,” *Polym. Eng. Sci.*, vol. 17, no. 4, pp. 246–250, 1977.

[86] J. a. Sauer, E. Foden, and D. R. Morrow, “Influence of molecular weight on fatigue behavior of polyethylene and polystyrene,” *Polym. Eng. Sci.*, vol. 17, no. 4, pp. 246–250, 1977.

[87] H. W. Starkweather, G. E. Moore, E. Hansen, T. M. Roder, and R. E. Brooks, “Effect of Crystallinity on the Properties of Nylons,” *J. Polym. Sci.*, vol. XXI, pp. 189–204, 1956.

[88] L. Pruitt and L. Bailey, “Factors affecting near-threshold fatigue crack propagation behaviour of UHMWPE.pdf,” *Polymer (Guildf).*, vol. 39, no. 8–9, 1998.

[89] S. Suresh, *Fatigue of Materials*, Second. Cambridge University Press, 1998.

[90] A. Bandyopadhyay, F. Espana, V. K. Balla, S. Bose, Y. Ohgami, and N. M. Davies, “Influence of porosity on mechanical properties and in vivo response of Ti6Al4V implants,” *Acta Biomater.*, vol. 6, no. 4, pp. 1640–1648, 2010.

[91] H. . Zhu, L. Lu, and J. Y. . Fuh, “Influence of binder’s liquid volume fraction on direct laser sintering of metallic powder,” *Materials Science and Engineering: A*, vol. 371, no. 1–2. pp. 170–177, Apr-2004.

[92] A. Chemical, “Fatigue Mechanisms of Thermoplastics,” *Polym. Eng. Sci.*, vol. 6, no. 4, pp. 363–368, 1966.

[93] D. Rittel, “Investigation of the heat generated during cyclic loading of two glassy

polymers. Part I: Experimental," *Mech. Mater.*, vol. 32, pp. 131–147, 2000.

[94] D. M. Analysis, "Introduction to Dynamic Mechanical Analysis (DMA) A Beginner ' s Guide."

[95] M. P. Sepe, *Thermal Analysis of Polymers*. 1997.

[96] D. Astm, "Dynamic Mechanical Thermal Analysis (DMTA)," p. 82527.

[97] K. P. Menard, *Dynamic Mechanical Analysis: A Practical Introduction*. 2008.

[98] F. Povolo and E. B. Hermida, "Analysis of the master curve for the viscoelastic behaviour of polymers," *Mech. Mater.*, vol. 12, no. 1, pp. 35–46, Aug. 1991.

[99] S. Kolossov, E. Boillat, R. Glardon, P. Fischer, and M. Locher, "3D FE simulation for temperature evolution in the selective laser sintering process," *Int. J. Mach. Tools Manuf.*, vol. 44, no. 2–3, pp. 117–123, Feb. 2004.

[100] K. Zeng, D. Pal, and B. Stucker, "A review of thermal analysis methods in Laser Sintering and Selective Laser Melting," in *Solid Freeform Fabrication Symposium*, 2012, pp. 796–814.

[101] A. Wegner and G. Witt, "PROCESS MONITORING IN LASER SINTERING USING THERMAL IMAGING," in *Solid Freeform Fabrication: Proceedings, August 2011: University of Texas at Austin*, 2011, pp. 405–414.

[102] R. Greco and L. Nicolais, “Glass transition temperature in nylons,” *Polymer (Guildf).*, vol. 17, no. 12, pp. 1049–1053, Dec. 1976.

[103] A. J. Lesser, “Changes in mechanical behavior during fatigue of semicrystalline thermoplastics,” *J. Appl. Polym. Sci.*, vol. 58, pp. 869–879, 1995.

[104] L. Pruitt and D. Rondinone, “The effect of specimen thickness and stress ratio on the fatigue behavior of polycarbonate,” *Polym. Eng. Sci.*, vol. 36, no. 9, pp. 1300–1305, May 1996.

[105] R. O. Ebewele, *Polymer Science and Technology*. CRC Press LLC, 1996.

[106] R. Rusenburg, L. Schmidt, and H. J. Schmid, “Mechanical and Physical Properties – A Way to assess quality of Laser Sintered Parts,” in *Innovative developments in virtual and physical prototyping: proceedings of the 5th international conference on advanced research in virtual and rapid prototyping, Leiria , 28 September–1 October 2011*, 2011, vol. 2200, pp. 239–251.

[107] D. Rouholamin and N. Hopkinson, “An investigation on the suitability of micro-computed tomography as a non-destructive technique to assess the morphology of laser sintered nylon 12 parts,” *Proc. Inst. Mech. Eng. Part B J. Eng. Manuf.*, Mar. 2014.

Appendices

Appendix A- Prony Series Calculation

A-1- Mechanical Model Analogies for Linear Viscoelastic Behaviour

A mechanical model with sufficient number of elastic elements (springs) and viscous elements (dashpots) can imitate the form of the time dependant or frequency dependant moduli of the material. In this type of model, force applied to the terminals of the model is analogous to σ, the relative displacement of the terminals is analogous to ε, and the rate of displacement is analogous to $\dot{\varepsilon}$. Stiffness of each spring element is analogous to elastic modulus distribution G_i and frictional resistance of each dashpot is analogous to a viscosity contribution η_i.

The simplest combinations are Maxwell model and Kelvin/Voigt models, shown in Figure A1, and more realistic models are made of combinations of these two models.

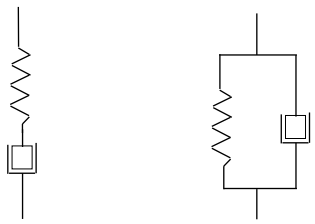

Figure A1- right) Maxwell Model, left) Kelvin/Voigt Model

These models are too simple to give a good quantitative fit to any polymer over an extended period of time. The behaviour of real viscoelastic materials is often modelled by combinations of Kelvin/Voigt and Maxwell models, an example of which is shown in Figure A2 [61].

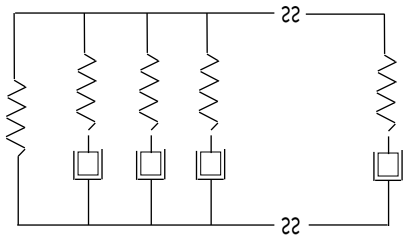

Figure A2- Generalized Maxwell model

The relaxation modulus for this model in time domain has the form

$$G(t) = G_e + \sum_{n=1}^{N} G_n e^{-t/\tau_n} \qquad \text{(Eq 1)}$$

where G_e is the steady-state stiffness, represented by the parallel spring.

And in frequency domain the modulus is given as;

$$G^*(\omega) = G_e + \sum_{n=1}^{N} \frac{G_n j\omega\tau_n}{1 + j\omega\tau_n} \qquad \text{(Eq 2)}$$

The sum of the exponential is also known as Prony Series.

A-2- Prony Series Calculation

In order to simulate viscoelastic behaviour through mathematical models and implement it in Finite Element analyses, viscoelasticity is modelled through the use of Prony series.

Prony series offer a straightforward fitting approach to experimental data obtained from viscoelastic materials. As mentioned in the previous section, viscoelastic properties can be modelled by Equations Eq 1 and Eq 2 in time and frequency domain respectively which are known as Prony series. Method for fitting data using the Prony series is explained in this section.

The real and imaginary parts of Equation Eq 2 can be rewritten as,

$$G_{real}(\omega) = G_e + G_0 \sum_{n=1}^{N} \left(g_n \frac{(\omega\tau_n)^2}{1 + (\omega\tau_n)^2} \right) \quad \text{(Eq 3)}$$

$$G_{img}(\omega) = G_0 \sum_{n=1}^{N} \left(g_n \frac{(\omega\tau_n)^2}{1 + (\omega\tau_n)^2} \right) \quad \text{(Eq 4)}$$

where g_n, τ_n and n are constant parameters of Prony series also known as Prony pairs. Loss factor can also be obtained as the ratio of imaginary to real parts of the modulus.

The relaxation modulus can be written in dimensionless form,

$$g_n(\omega) = \frac{G(\omega)}{G_0} \quad \text{(Eq 5)}$$

where$G_0$is the instantaneous or initial modulus and is given by replacing *t*=0 in Equation Eq 1 as,

$$G_0 = G_e + \sum_{n=1}^{N} G_n \quad \text{(Eq 6)}$$

Using Equations Eq 5 and Eq 6, equilibrium modulus or long term modulus is given as,

$$G_e = G_0(1 - \sum_{n=1}^{N} g_n) \quad \text{(Eq 7)}$$

An optimisation routine was used to fit Prony series parameters to the complex modulus. Range of frequency in the master curve was first divided to even spaces (τ values). Minimum and maximum values of storage and loss moduli and loss factor for each step were attained from the master curve. Appropriate g values were then selected using the Nelder-Mead multi-parameter optimiser (fminsearch). These constants were implemented in Equations7-3 and 7-4 to calculate new values of moduli and loss factor. The error between the complex modulus defined by the Prony series parameters and modulus values from the master curve was calculated and the process was repeated to minimise the error.

Smaller number of Prony terms results in a fitting that is less accurate. Figure A3 shows five Prony terms fitted to the viscoelastic properties curves (storage modulus, loss modulus and loss factor) derived from experimental results. The poor fit can be observed for all three viscoelastic properties. By increasing the number of Prony terms to twenty, a better fitting can be obtained as shown in Figure A4.

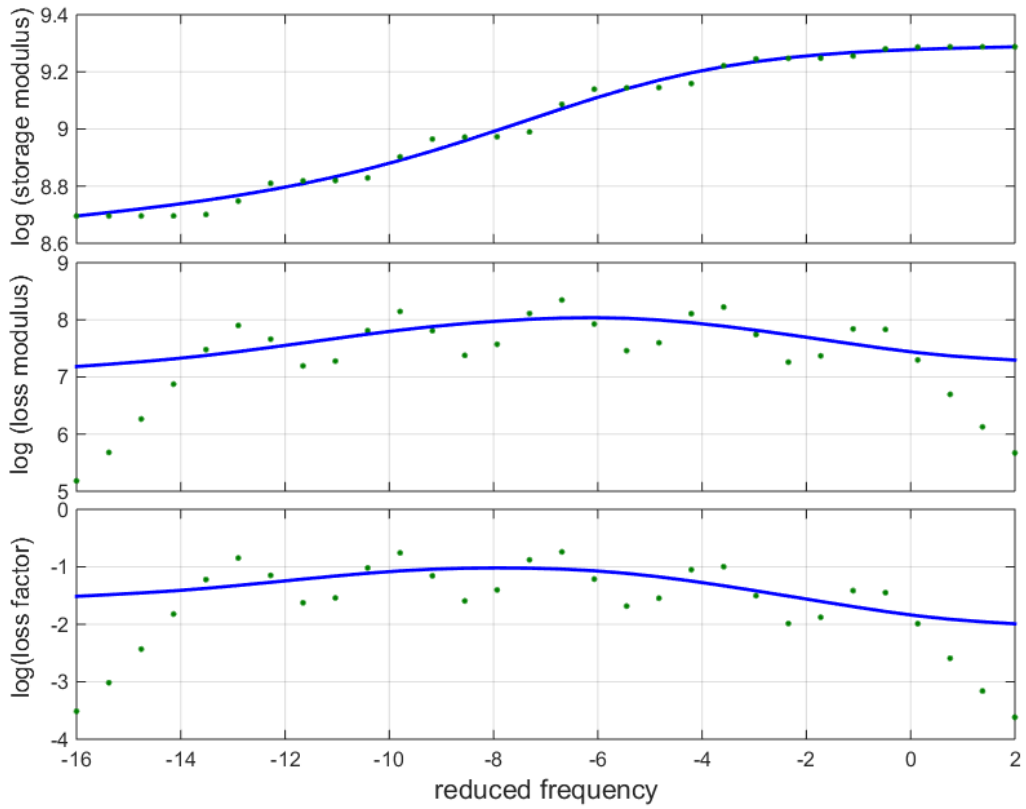

Figure A3- Five Prony terms fitted to viscoelastic properties. Viscoelastic properties derived from experiment (solid curves) and from Prony series ("•")

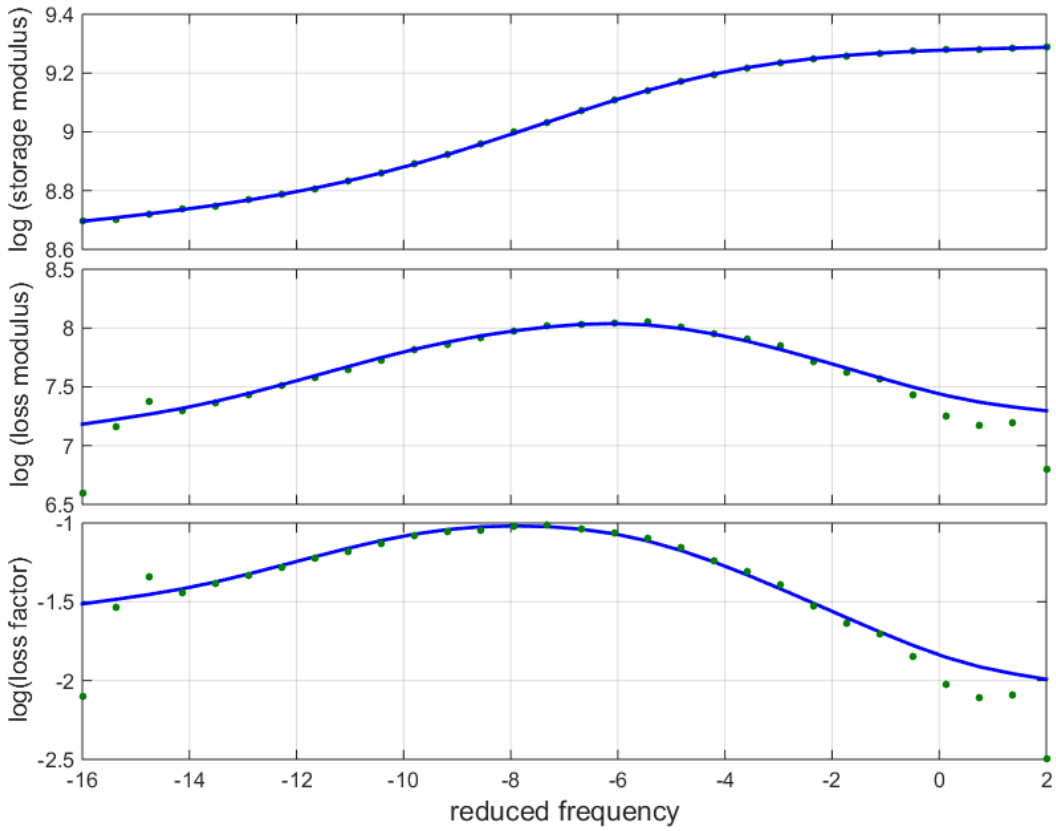

Figure A4- Twenty Prony terms fitted to viscoelastic properties showing a better fit. Viscoelastic properties derived from experiment (solid curves) and from Prony series ("•")

Prony parameters for twenty terms obtained from Figure A4 are shown in Table A1. These terms can be used in Finite Element modelling process to incorporate the viscoelastic behaviour of the material. Prony parameters for twenty terms are shown in the Table A1.

Table A1- Twenty Prony terms (n=20) considered to fit to material properties at 27°C

n	g	tau
1	$2.145889842478965\times10^{-2}$	$1.389495494373136\times10^{14}$
2	$8.749367245189710\times10^{-3}$	$1.930697728883254\times10^{13}$
3	$1.782403330629578\times10^{-2}$	$2.682695795279728\times10^{12}$
4	$1.909904300989806\times10^{-2}$	$3.727593720314938\times10^{11}$
5	$2.481969831053288\times10^{-2}$	$5.179474679231223\times10^{10}$
6	$3.257381588850206\times10^{-2}$	$7.196856730011528\times10^{9}$
7	$4.038117256527018\times10^{-2}$	$1.000000000000000\times10^{9}$
8	$4.956938824001111\times10^{-2}$	$1.389495494373136\times10^{8}$
9	$6.089639404001057\times10^{-2}$	$1.930697728883246\times10^{7}$
10	$6.612908236148729\times10^{-2}$	$2.682695795279727\times10^{6}$
11	$7.520981162949614\times10^{-2}$	$3.727593720314938\times10^{5}$
12	$7.215872405201273\times10^{-2}$	$5.179474679231202\times10^{4}$
13	$6.581995705296451\times10^{-2}$	$7.196856730011528\times10^{3}$
14	$5.545231581991017\times10^{-2}$	$1.000000000000000\times10^{2}$
15	$4.482079849045983\times10^{-2}$	$1.389495494373136\times10^{2}$
16	$2.792029738975821\times10^{-2}$	$1.930697728883253\times10^{1}$
17	$2.548859904117340\times10^{-2}$	2.682695795279727
18	$1.535667674957897\times10^{-2}$	$3.727593720314938\times10^{-1}$
19	$6.994105086997937\times10^{-3}$	$5.179474679231223\times10^{-2}$
20	$1.336171924802065\times10^{-2}$	$7.196856730011528\times10^{-3}$

Appendix B – SPSS Statistical Analysis Results

B-1- Tensile Test Results

Ultimate Tensile Strength

Hypothesis Test Summary

	Null Hypothesis	Test	Sig.	Decision
1	The distribution of UTS is the same across categories of Cross_Sectional_Area.	Independent-Samples Kruskal-Wallis Test	.007	Reject the null hypothesis.

Asymptotic significances are displayed. The significance level is .05.

EaB

Hypothesis Test Summary

	Null Hypothesis	Test	Sig.	Decision
1	The distribution of EaB is the same across categories of Cross_Sectional_Area.	Independent-Samples Kruskal-Wallis Test	.387	Retain the null hypothesis.

Asymptotic significances are displayed. The significance level is .05.

Young's Modulus

Hypothesis Test Summary

	Null Hypothesis	Test	Sig.	Decision
1	The distribution of Young_Modulus is the same across categories of Cross_Sectional_Area.	Independent-Samples Kruskal-Wallis Test	.043	Reject the null hypothesis.

Asymptotic significances are displayed. The significance level is .05.

B-2- Tension-Tension Cyclic Test Results

Section Thickness

Hypothesis Test Summary

	Null Hypothesis	Test	Sig.	Decision
1	The distribution of cycles is the same across categories of Thickness.	Independent-Samples Kruskal-Wallis Test	.152	Retain the null hypothesis.

Asymptotic significances are displayed. The significance level is .05.

B-3- Tension-Compression Cyclic Tests Results

Second Batch- Maximum Stress 20MPa

Ranks

	Section Thickness	N	Mean Rank	Sum of Ranks
Cycles to Failure	4mm	8	12.63	101.00
	6mm	10	7.00	70.00
	Total	18		

Test Statistics[a]

	Cycles to Failure
Mann-Whitney U	15.000
Wilcoxon W	70.000
Z	-2.222
Asymp. Sig. (2-tailed)	.026
Exact Sig. [2*(1-tailed Sig.)]	.027[b]

a. Grouping Variable: Section Thickness

b. Not corrected for ties.

Second Batch- Maximum Stress 30MPa

Ranks

	Section_Thickness	N	Mean Rank	Sum of Ranks

Number_of_Cycles	4mm	5	4.60	23.00
	6mm	5	6.40	32.00
	Total	10		

Test Statistics[a]

	Number_of_Cycles
Mann-Whitney U	8.000
Wilcoxon W	23.000
Z	-.943
Asymp. Sig. (2-tailed)	.346
Exact Sig. [2*(1-tailed Sig.)]	.421[b]

a. Grouping Variable: Section_Thickness

b. Not corrected for ties.

Third Batch- Maximum Stress 20MPa

Ranks

	Section Thickness	N	Mean Rank	Sum of Ranks
Cycles to Failure	4mm	7	4.86	34.00
	6mm	6	9.50	57.00
	Total	13		

Test Statistics[a]

	Cycles to Failure
Mann-Whitney U	6.000
Wilcoxon W	34.000
Z	-2.143
Asymp. Sig. (2-tailed)	.032
Exact Sig. [2*(1-tailed Sig.)]	.035[b]

a. Grouping Variable: Section Thickness

b. Not corrected for ties.

Third Batch- Maximum Stress 30MPa

Ranks

	Section_Thickness	N	Mean Rank	Sum of Ranks
Number_of_Cycles	4mm	5	3.40	17.00

	6mm	5	7.60	38.00
	Total	10		

Test Statistics[a]

	Number_of_Cycles
Mann-Whitney U	2.000
Wilcoxon W	17.000
Z	-2.193
Asymp. Sig. (2-tailed)	.028
Exact Sig. [2*(1-tailed Sig.)]	.032[b]

a. Grouping Variable: Section_Thickness

b. Not corrected for ties.

Appendix C – Full S-N curve table

Sample	Load (N)	Max Stress (MPa)	Average number of cycles to failure
#17	1200	30	236
#23			259
#50			223
#14	1050	26	440
#26			524
#80			428
#20	900	23	1026
#38			878
#47			954
#35	800	20	2152
#41			2353
#71			2251
#77	650	16	$>10^6$
#5			$>10^6$

Appendix D – Publications

Results from Chapter 7 of this thesis have been published in Journal of Materials Research;

Hoda Amel, Hadi Moztarzadeh, Jem Rongong, Neil Hopkinson, Investigating the behaviour of Laser Sintered Nylon 12 parts subject to dynamic loading, *Journal of Materials Research*, *Vol 29 / Issue 17 / 2014, pp 1852-1858*

Two more publications are expected.